Showcasing research from Professor Makoto Ogawa's laboratory, School of Energy Science and Engineering, VISTEC, Thailand

Designed functions of oxide/hydroxide nanosheets *via* elemental replacement/doping

The replacement of main components with small amounts of heteroelements in layered materials affects the properties and imparts novel functions, as in the variation of cakes coming from the main components and the alternating layered organization with a variety of ingredients.

As featured in:

See Makoto Ogawa *et al.*,
Chem. Soc. Rev., 2024, **53**, 10523.

ROYAL SOCIETY
OF **CHEMISTRY**

rsc.li/chem-soc-rev

Designed functions of oxide/hydroxide nanosheets *via* elemental replacement/doping

Kanji Saito, [iD] [ab] Masashi Morita, [iD] [c] Tomohiko Okada, [iD] [d] Rattanawadee (Ploy) Wijitwongwan [e] and Makoto Ogawa [iD] *[e]

Partial replacement of one structural element in a solid with another of a similar size was conducted to impart functionality to the solids and modify their properties. This phenomenon is found in nature in coloured gemstones and clay minerals and is used in materials chemistry and physics, endowing materials with useful properties that can be controlled by incorporated heteroelements and their amounts. Depending on the area of research (or expected functions), the replacement is referred to as "isomorphous substitution", "doping", *etc.* Herein, elemental replacement in two-dimensional (2D) oxides and hydroxides (nanosheets or layered materials) is summarised with emphasis on the uniqueness of their preparation, characterisation and application compared with those of the corresponding bulk materials. Among the 2D materials (graphene, metallenes, transition metal chalcogenides, metal phosphate/phosphonates, MXenes, *etc.*), 2D oxides and hydroxides are characterised by their presence in nature, facile synthesis and storage under ambient conditions, and possible structural variation from atomic-level nanosheets to thicker nanosheets composed of multilayered structures. The heteroelements to be doped were selected depending on the target application objectively; however, there are structural and synthetic limitations in the doping of heteroelements. In the case of layered double hydroxides (single layer) and layered alkali silicates (from single layer to multiple layers), including layered clay minerals (2∶1 layer), the replacement (commonly called isomorphous substitution) is discussed to understand/design characteristics such as catalytic, adsorptive (including ion exchange), and swelling properties. Due to the variation in their main components, the design of layered transition metal oxide/hydroxide materials *via* isomorphous substitution is more versatile; in this case, tuning their band structure, doping both holes and electrons, and creating impurity levels are examined by the elemental replacement of the main components. As typical examples, material design for the photocatalytic function of an ion-exchangeable layered titanate (lepidocrocite-type titanate) and a perovskite niobate ($KCa_2Nb_3O_{10}$) is discussed, where elemental replacement is effective in designing their multiple functions.

1. Introduction

The replacement of one structural element with another one of a similar size is often referred to as "isomorphous substitution", which is commonly confused with the term "defect",

another form of replacement (concerning vacancies). In nature, there are well-known classes of materials in which isomorphous substitution and/or defects play key roles in their characteristics/functions. The replacement of an element in the structure of semiconductor materials is one of the most common examples, and the term "doping" is used for the intentional introduction of impurities into an intrinsic semiconductor to modulate its electrical, optical and structural properties. Alternatively, since the discovery of cupric oxide-based superconductors in the 1980s by J. G. Bednorz and K. A. Muller,[1] changes in the superconducting and magnetic properties of high-temperature oxide-based superconductors as a function of oxygen stoichiometry and cation substitution have been systematically and extensively investigated to find superconducting properties that can be continuously optimised at a specific doping level. Thus, the replacement of a framework

[a] *Department of Materials Science, Graduate School of Engineering Science, Akita University, 1-1 Tegatagakuen-machi, Akita-shi, Akita 010-8502, Japan*

[b] *Kagami Memorial Research Institute for Materials Science and Technology, Waseda University, 2-8-26 Nishiwaseda, Shinjuku-ku, Tokyo 169-0054, Japan*

[c] *Department of Applied Chemistry, Tokyo University of Agriculture and Technology, Tokyo 184-8588, Japan*

[d] *Department of Materials Chemistry, and Research Initiative for Supra-Materials, Shinshu University, 4-17-1 Wakasato, Nagano, Nagano-shi 380-8553, Japan*

[e] *School of Energy Science and Engineering, Vidyasirimedhi Institute of Science and Technology (VISTEC), 555 Moo 1, Payupnai, Wangchan, Rayong 21210, Thailand. E-mail: makoto.ogawa@vistec.ac.th*

This journal is © The Royal Society of Chemistry 2024

Chem. Soc. Rev., 2024, **53**, 10523–10574 | **10523**

element is a versatile way to modify the properties of solids (not only crystalline but also amorphous solids) from insulators to superconductors and impart functions (optical properties as notable examples). In this case, various terms such as doping/dopants, replacement/guests, isomorphous substitution and lattice substitution are used depending on the research field and materials. Doping is commonly used in semiconductor science, where very small quantities of heteroelements can significantly modify the electrical properties of materials. The term "substitution" is commonly used when replacing one element with another in larger quantities ranging from several percentage to several tens of percentage in some cases.

Elemental doping/isomorphous substitution is found in nature. For example, the origin of colours in coloured gemstones[2] and charges in clay minerals[3] is well-known. The replacement in oxide-based crystals such as quartz (crystalline silica), corundum (α-alumina), beryl and chrysoberyl with trace amounts of heteroelements such as iron, titanium, chromium, vanadium and magnesium causes changes in the corresponding colours. The colour of amethyst (Fig. 1), purple-coloured quartz, is explained by the unusual irradiation-induced valence of iron (or other transition metal ions) as impurities in the quartz crystal lattice. Sapphires are described by their colour (blue, green, and yellow, which is dependent on

Kanji SAITO received his BS in 2012 and MS in 2014 from Waseda University, supervised by Professor Makoto Ogawa. He received his PhD from Waseda University in 2017 under the direction of Professor Yoshiyuki Sugahara. He was Research Associate at Waseda University from 2015 to 2017. Thereafter, he joined Akita University in 2017 as Specially Appointed Assistant Professor and moved to a permanent position in 2021. He was promoted to Lecturer, his current position, in 2024. His research interest focuses on layered inorganic solids including layered clay minerals and layered transition metal oxides.

Kanji Saito

Masashi Morita received his BS (2011) and MS (2013) from Waseda University under the supervision of Professor Makoto Ogawa. From 2013 to 2021, he worked as a researcher at Panasonic Corporation and was promoted to senior researcher (2017–present) and has been working as a project leader (2018–present). In 2021, he received his PhD from Nagoya University under the supervision of Professor Ryotaro Matsuda. After receiving his PhD, he moved to the Division of Applied Chemistry, Institute of Engineering at Tokyo University of Agriculture and Technology as an assistant professor. He was promoted to lecturer in October 2024. His current research interests are the design and synthesis of inorganic–organic hybrid materials focusing on 2D materials and metal complexes for adsorbents and catalysts.

Masashi Morita

Tomohiko Okada received his PhD from Waseda University in 2004 under the direction of Professor Makoto Ogawa. In 2006, he moved to Shinshu University, Nagano Prefecture Japan as an assistant professor. He is presently an associate professor in the Department of Materials Chemistry, Shinshu University. His research interests are materials chemistry of clay-based adsorbents and catalysts.

Tomohiko Okada

Rattanawadee (Ploy) Wijitwongwan received her BEng degree in Petrochemicals and Polymeric Materials Engineering from Silpakorn University with First Class Honors. She completed her PhD in 2023 at Vidyasirimedhi Institute of Science and Technology (VISTEC), Thailand. Currently, she is a postdoctoral researcher under the supervision of Prof. Makoto Ogawa at the School of Energy Science and Engineering (ESE) at VISTEC. Her research interests focus on the synthesis of layered double hydroxides, especially for composition control, for environmental and energy-related applications.

Rattanawadee (Ploy) Wijitwongwan

10524 | *Chem. Soc. Rev.*, 2024, **53**, 10523–10574

This journal is © The Royal Society of Chemistry 2024

Fig. 1 Colour variation in quartz caused by isomorphous substitution; amethyst is quartz containing a trace amount of iron. Permission for photography was given by Mineral Industry Museum of Akita University. The archive number is 292 and 14277 for quartz and amethyst, respectively.

the doped element and its states), where the intense blue of blue sapphire is caused by the replacement of aluminium in corundum with titanium and iron. The synthesis of coloured gemstone crystals (ruby and sapphire as notable examples) in the laboratory has also been examined to obtain materials mimicking the mechanical, chemical, optical, and physical characteristics of natural gemstones for industrial applications, including the jewellery industry. Synthetic *gem* crystals have been manufactured since the 19th century, and among them, synthetic ruby is one of the first successful examples used in abrasives, communications, electronics and optics. Lasing materials were designed from yttrium aluminium garnet ($Y_3Al_5O_{12}$) by the replacement of yttrium with titanium and rare earth ions to obtain varying wavelength emissions (known as YAG laser).[4] Intense emission was seen when the Nd content was 3 atomic%. When the Nd content was 6 atomic%, the emission intensity was reduced as a result of the Nd–Nd interactions. Various optical properties were reported for rare earth element-doped oxides.[5] In addition to the crystalline host lattice, various transition metal ions and rare earth metal ions have been incorporated in inorganic glasses for optical applications as phosphors and laser since the first demonstration of the laser action of Nd^{3+} ions (concentration of Nd_2O_3 in the

range of 0.13 to 2.0 wt%) in barium crown glass.[6] These examples clearly indicate the importance of the heteroelements and their amounts.

Thus, the doping (isomorphous substitution) of heteroelements has been applied in many solid-state materials. However, there is no general consensus on the relationship between doping and properties and there are several emerging new classes of materials, and thus doping in numerous materials has become the focus of research. To tune the target properties, parameters such as elemental variation and quantity and distribution of the dopant have been examined. Also, to obtain reliable and reproducible results, the synthetic methods and conditions have been optimised. There are solubility limits depending on the system, the required concentration level is different for each application, and in some applications, an extension of the dopant concentration is expected. Furthermore, the state and location of the doped heteroelements have been investigated using advanced analytical tools with the appropriate atomic resolution.

The materials and material designs described above are based on bulk materials and the solubility limit is applicable to bulk solids. When isomorphous substitution occurs at the surface (not in the bulk), the surface properties are substantially modified, and new surface properties emerge. This occurs in various materials and is efficient, especially for materials with a nanoscopic size and/or nanoporous structures. The isomorphous substitution in layered clay minerals is a representative example, where the isomorphous substitution of the main component with a heteroelement with lower valence represents the primary source of negative charges in silicate-based clay minerals. Alternatively, isomorphous substitution in brucite-type layered hydroxide with an ion of higher valence (namely M^{2+} is replaced with M^{3+}) leads to a positive charge, providing a class of anion-exchangeable materials, *i.e.*, layered double hydroxides (LDHs, also as anionic clay or hydrotalcite-type compounds).

Another well-known example of isomorphous substitution in nanomaterials is that of the main components such as silicon in zeolites with other tetrahedrally coordinated heteroatoms such as Al^{3+} and Ga^{3+} at a few wt%, which has been used to obtain catalysts.[7,8] The activities are known to be determined by the coordination states of the heteroelements. Besides trivalent metal cations, Ti^{4+} has been incorporated into the frameworks of silicates as an isolated tetrahedrally coordinated species. A charge transfer-type excited state is generated under light irradiation. The photocatalytic reduction of carbon dioxide by UV light has been examined using Ti-containing zeolites, mesoporous silicas and metal–organic frameworks.[9–11] Initially, this concept was known as "single-site catalyst", while more recently, it is referred to as "single-atom catalyst".[12]

The incorporation of a second metal ion into the nodes of the frameworks of porous coordination polymers (PCPs), which are also called metal–organic frameworks (MOFs), has been reported.[13–17] MOFs are a class of porous materials with a very large surface area and high porosity, leading to significant interest for their application in gas storage, separation,[18,19]

Makoto Ogawa was educated in the Department of Applied Chemistry, Waseda University, supervised by Professor Chuzo Kato. After postdoctoral research at RIKEN, he joined Waseda University and worked on inorganic materials chemistry as a full professor in 2004. In 2015, he moved to Thailand as an opening professor at the School of Energy Science and Engineering, Vidyasirimedhi Institute of Science and Technology (VISTEC), which opened in 2015 in Rayong, Thailand and continues his research activity in materials chemistry.

Makoto Ogawa

This journal is © The Royal Society of Chemistry 2024

Chem. Soc. Rev., 2024, **53**, 10523–10574 | **10525**

detection,[20] catalysis,[21] medicine,[22] *etc.* MOFs are constructed from inorganic nodes and organic linkers. The partial replacement of the inorganic nodes with other metal ions (the products are called bimetallic or mixed metal MOFs) has been used to control their properties, including adsorptive, catalytic, and optical properties.[22–27] These bimetallic (or mixed metal) MOFs have been prepared by metal doping during crystallisation or post-synthetic ion exchange.[28]

Heteroelement doping/substitution in nanomaterials with lower dimensions (2D, 1D and 0D) has been examined. The replacement of the main components in oxide and hydroxide nanosheets with heteroelements are the topics of this review article because of their presence in nature, facile synthesis and storage, possible structural variation from nanosheet to multi-layered structures, and morphological variation from nanodot to large single crystals. Considering their advantageous characteristics, 2D oxides/hydroxides are useful for vast applications ranging from civil engineering to molecular and biomedical applications. Non-oxide 2D materials including graphene and transition metal dichalcogenides have been studied extensively and heteroatom doping has become an effective method to tune their opto-electronic and chemical characteristics for the increasing demands in fields such as optoelectronics and sensing.[29–32]

After the discovery of a layered zeolite (MCM-22, later designated as MWW) framework in the 1990s,[33,34] layered or 2D zeolites, which are stacked nanometer-thick layers or mono-layer assemblies, became an important direction in the development of zeolites for better performances and new applications. One of the advantages of zeolite nanosheets is generating more open pore connections for the diffusion of reactants and products.[35,36] Similarly nanosheet (or 2D) MOFs are becoming popular materials.[37,38] Nanosheets of bimetallic MOFs have also been published.[39]

2D materials (layered materials/flat materials) of varying compositions and structures are known, as described above (Fig. 2).[40–44] Some layered materials have been dispersed in solvents to realise a single-sheet dispersion (exfoliation) and obtain nanosheets.[45,46] Exfoliation has been achieved in some polymers to obtain polymer nanocomposites. Porous nanoarchitectures have been designed by the cross-linking of nanosheets with organic moieties and inorganic (metals, oxides, and chalcogenides) nanoparticles (pillars) by intercalation into the layered materials and by exfoliation and restacking.[47] The surface of each nanosheet is exposed by these approaches to utilise it for adsorption/immobilisation and reactions more efficiently. Thus, compared with isomorphous substitution in bulk materials, that in layered materials has a greater impact on the sophisticated materials design.

In the present review, we summarise the elemental replacement of the framework elements (isomorphous substitution) in oxide-based and hydroxide-based layered materials (using layered double hydroxides, layered alkali silicates, 2 : 1 type phyllosilicates, and layered transition metal oxides) and derived nanosheets. Based on the variation in the layer thickness and composition, four groups of layered materials, as
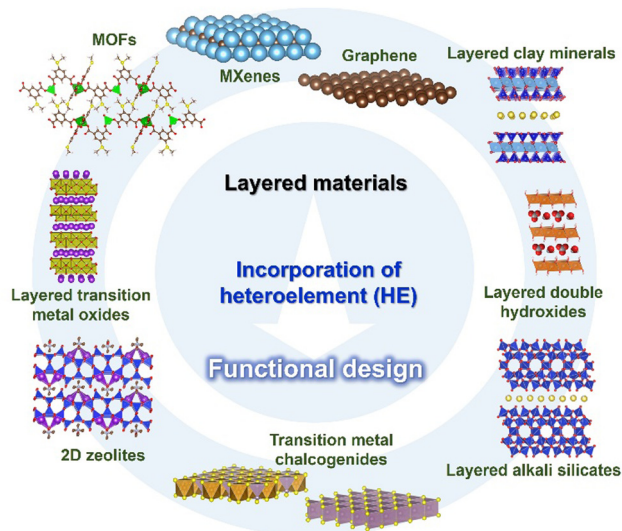

Fig. 2 Incorporation of heteroelements into 2D materials.

summarised in Fig. 3, will be introduced as representative examples of layered materials functionalised by isomorphous substitution. Layered double hydroxides are regarded as the representative example of single layer materials with versatile compositional variation. Layered alkali silicates are chosen because a variation in their layer thickness keeps the main component as silica/silicate. Also, 2 : 1-type phyllosilicates (smectite group of clay minerals) are important examples of unit layers composed of multiple sheets (composed of two silicate sheets sandwiching one metal hydroxide sheet), where the metal ion in the hydroxide sheet has a compositional variation (Mg, Al, Fe, *etc.*). Layered transition metal oxides (LTMO) are larger categories including several structural types, offering a wide compositional and structural variation. To simplify the discussion, lepidocrocite-type layered titanates will be discussed as the representative example of single-layer LTMO, and a perovskite niobate ($KCa_2Nb_3O_{10}$, a Dion–Jacobsen-type perovskite) as the example of LTMO with possible expandable thickness of the unit layer. The experimental methods for the replacement (or the preparation of the
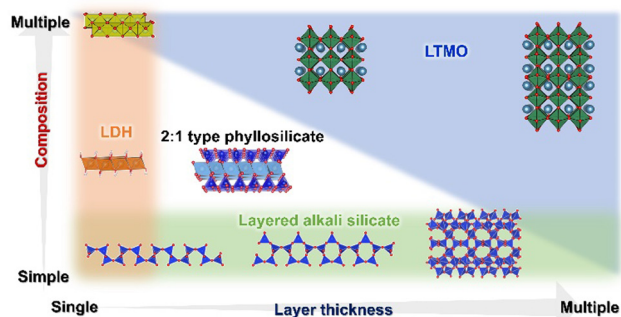

Fig. 3 Layered double hydroxides, layered alkali silicates, 2 : 1 type phyllosilicates, and layered transition metal oxides represent layered materials with varying layer thickness and/or composition.

10526 | *Chem. Soc. Rev.*, 2024, **53**, 10523–10574

This journal is © The Royal Society of Chemistry 2024

heteroelement-incorporated layered materials and the nanosheets), the characterisation and the possible (and the examined) functions of the products will be introduced to highlight the important roles of the elemental replacement in the design of 2D materials.

2. Metal hydroxides and layered double hydroxides

Layered double hydroxides (LDHs) are representative examples of layered materials, where isomorphous substitution plays a key role in their structures, characteristics, and functions. As the most well-known example, the isomorphous substitution of Mg^{2+} in brucite (magnesium hydroxide) with Al^{3+} results in layered materials with anion exchange capability. The material containing carbonate as the charge compensating anion in the interlayer space is named hydrotalcite, which was found as a mineral in Sweden in the 19th century and named due its capacity to be crushed into a white powder similar to talc, a 2:1-type layered clay mineral (see Section 4 of this review). The structural concept is applicable to other metal hydroxides and the substitution of the main component with heteroelements produces a series of layered materials named layered double hydroxides (LDHs),[48–53] as shown in Fig. 4. LDHs with various compositions such as $Mg_6Fe_2(OH)_{16}CO_3 \cdot 4.5H_2O$ (pyroaurite), $Mg_6Cr_2(OH)_{16}CO_3 \cdot 4H_2O$ (stichtite), $Ni_6Al_2(OH)_{16}CO_3OH \cdot 4H_2O$ (takovite), and $Mg_4Fe(OH)_{10}Cl \cdot 3H_2O$ (iowaite) have been found as minerals.[54–59] Occasionally, "anionic clay", "hydrotalcite", and "hydrotalcite-like compounds" are used as alternative terminologies for LDHs in the literature. The synthesis of LDHs (at that time, referred to as hydrotalcite-like compounds) was reported by Feitknecht in the 1940s.[60,61]

Some LDHs are commercially available as an antacid under the product name Talcid® (Bayer Healthcare AG) or a stabiliser in polyvinylchloride (PVC) resins by scavenging chloride.[62,63] The properties of LDHs are different depending on their M^{2+}, M^{3+} and interlayer anions. Therefore, the compositional variation in LDHs leads to their application in many different fields such as adsorbent/anion exchangers,[64] catalysts and catalyst supports,[65,66] electrodes/capacitors,[67] anti-corrosion coatings,[68] drug/gene carriers,[69,70] and other medical/pharmaceutical applications. In addition, LDHs are used as precursors of oxides upon calcination, and the obtained mixed oxides are used as pigments, functional ceramics, catalysts and ion exchangers (reconstruction method).[71–73] The ability to tune their properties through compositional adjustments and possible morphosynthesis has attracted considerable attention in each application.

2.1. Structure of LDHs and their compositional variation

The structure of LDHs is determined by the selection of M^{2+} and M^{3+}, $M^{3+}/(M^{2+} + M^{3+})$ ratio and interlayer anions.

2.1.1. Selection of M^{2+} and M^{3+} and $M^{3+}/(M^{2+} + M^{3+})$ ratio in the layer. In the case of functional design, the main component (M^{2+}) is selected to satisfy the required function, in addition to the associated requirements of elemental toxicity, solubility and stability of the starting materials and their hydroxide, cost/availability, etc. Then, the second component (M^{3+}) is selected based on the target function. Regarding structural aspects, M^{3+} has an ionic size similar to M^{2+}, which is a requirement for the isomorphous substitution in the brucite-like sheet. The amount of isomorphous substitution is affected by the difference in the ionic radius between M^{2+} and M^{3+}, leading to the phase separation of LDHs and impurity phases. Thus, to avoid phase separation, the difference in the ionic radius between M^{2+} and M^{3+} should be minimised to maintain the structure of a brucite-like sheet.[48–52,74] In addition to the crystal chemistry aspects, the availability and the solution behaviour of metal salts (and the solubility of hydroxides) are considered when the preparation is done in solution.

The $M^{3+}/(M^{2+} + M^{3+})$ ratio in the brucite-like sheet corresponds to the layer charge density, correlating the properties of LDHs. The $M^{3+}/(M^{2+} + M^{3+})$ ratio is denoted by x in the chemical formula of LDHs, $[M^{2+}_{1-x}M^{3+}_x(OH)_2]^{x+}[A^{n-}]_{x/n} \cdot mH_2O$ and x is commonly found in the range of 0.20–0.33.[49–51] When attempting to vary x beyond the common range, impurity phases such as metal hydroxides, metal oxides, and basic salts of the divalent or trivalent metal ion are encountered in most cases, as shown in Fig. 5. The limitation of x is thought to be caused by two factors, i.e., electrostatic repulsion between the neighbouring trivalent cations in the brucite-like sheet and the repulsion between the charge-balancing anions. These
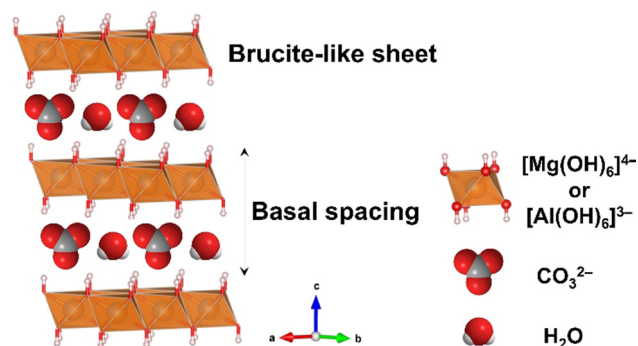

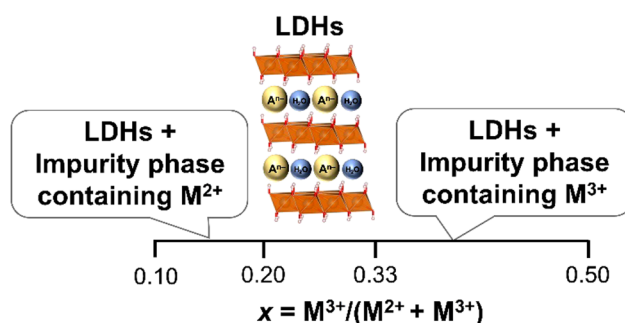**Fig. 4** Structure of layered double hydroxides. The crystal structure was drawn using the VESTA program.[44]

Fig. 5 Common phenomena in the formation of LDHs when different values of x were employed.

This journal is © The Royal Society of Chemistry 2024

Chem. Soc. Rev., 2024, **53**, 10523–10574 | **10527**

repulsive forces prevent higher layer charge densities corresponding to $x > 0.33$. The difficulty in obtaining a smaller x ($x < 0.20$) was explained by the large distance between the adjacent interlayer anions, leading to the collapse of the layered structure.

In addition to the substitution in the brucite-like sheet, the defects in the sheets are thought to play a role in several functions, especially in photocatalysis,[75] where LDHs have been used.[76] M^{3+} is thought to be isolated by M^{2+} in the brucite-like sheet, and thus the removal of M^{3+} was examined to generate vacancies in the brucite-like sheet.[77,78] Because of the difficulties in identifying and quantifying the vacancies in the brucite-like sheet, the roles of the vacancies in the functions of LDHs have not been well elucidated.[79]

2.1.2. Selection of the interlayer anion. A variety of anionic species has been incorporated during the formation of LDHs or by anion exchange of LDHs.[48–53] Depending on the interlayer anion, neutral molecules (including water) are intercalated together with the charge-compensating anions. Common examples of the anions in LDHs include halides (F^-, Cl^-, Br^-, and I^-), oxo-anions (NO_3^-, ClO_4^-, SO_4^{2-}, and CO_3^{2-}), oxometallate anions (MnO_4^-, CrO_4^{2-}, $Cr_2O_7^{2-}$, AsO_4^{3-}, $Mo_7O_{24}^{6-}$, *etc.*) and organic anions (dodecyl sulfate, dodecyl benzene sulfonate, adipate, oxalate, *etc.*). The basal spacing of LDH varies in relation to the size, charge, and orientation of the interlayer anions and their solvation.
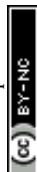
2.2. Synthetic methods for LDHs

A variety of synthetic methods (and conditions in each method) has been employed to prepare LDHs with the desired composition (metal combinations, interlayer anions, and composition) and particle morphology to satisfy the application requirements.

2.2.1. Co-precipitation from solution; the most common method. Co-precipitation from solution has been widely employed for the preparation of LDHs. Co-precipitation involves mixing an aqueous solution of divalent and trivalent metal salts and a basic solution for the nucleation of hydroxide, followed by crystal growth during ageing. For the metal cation to precipitate as hydroxide, an increase in pH until the solubility limit of the metal hydroxides is required. The mechanism is based on the condensation of hexa-aqua complexes of metal ions in the solution to build hydroxide layers of two metal cations with different valences. This process generates positively charged layers, and simultaneously attract anionic species.[49,80,81] The experimental parameters for the co-precipitation of LDHs are pH of the reaction solution, concentration of metal salts, reaction temperature/time, solvent, mixing method for the nucleation and temperature/pressure/time for the ageing. These parameters are used to control the rate of nucleation and growth, allowing the customisation of the composition and morphology of LDHs. Several mixing sequences and mixing/heating methods have been used. In addition to mixing with basic solution, hydroxides are supplied by the hydrolysis of urea and hexamethylenetetramine upon heating for the formation of LDHs.

(a) Co-precipitation from an aqueous solution of metal salts by the addition of a basic solution is the most common method for the synthesis of LDHs.[48,80,82–84] This method has many advantages, such as ease of scaling-up. The sequence of mixing varies as follows: (a-i) An aqueous solution of NaOH, KOH or NH$_4$OH is slowly added to an aqueous solution (normally acidic) of M^{2+} and M^{3+} salts, resulting in a high pH of the mixture, referred to as the titration method.[85–87] Given that metal hydroxides precipitate at different pH, the composition of the precipitate is not the same as the M^{2+} and M^{3+} ratio in the initial solution when the final pH is not high enough for the complete precipitation of M^{2+} and M^{3+}.[88,89] Co-precipitation at the pH for high supersaturation leads to the formation of less crystalline LDHs and the aggregation of nanometer-size particles. This is a result of the formation of a larger number of nuclei by the rapid nucleation in the initial stage.[49,90–93] Thus, a crucial limitation of this sequence (adding base to the acidic solution of metal salts; titration) is the continuous change in the solution pH during the addition. The formation of individual metal hydroxide phases and LDHs also occurs. (a-ii) A basic solution and an acidic solution of metal salts are simultaneously added to a third solution, which contains the anion to be intercalated into the interlayer space of the resulting LDHs (constant pH method). By adjusting the rate of the addition, the pH of the mixture is controlled at a constant value suitable for the formation of the target LDHs. This method provides the condition of lower supersaturation, favouring particle growth over nucleation, resulting in LDHs with relatively higher crystallinity and larger particle sizes. A limitation of the constant pH method is the large volume of the solvent required to control the pH. With the large volume of solvent used in the process, the separation of the precipitate is difficult.[49] Alternatively, this method has a frequent acquisition of the desired composition as an advantage. Generally, LDHs formed by the co-precipitation are finite particles with a broad particle size distribution, and aggregation of the finite particles is observed. Several conditions and methods such as different types of mixing conditions and post-synthetic ageing have been introduced to achieve homogeneity and higher crystallinity and to reduce particle aggregation.

(b) Co-precipitation from a homogeneous solution of metal salts during the hydrolysis of urea, hexamethylenetetramine, ammonium carbonate, *etc.* Co-precipitation of LDHs is possible by the decomposition of urea at elevated temperatures. This process involves the hydrolysis of urea, releasing carbonate and ammonium, which results in an increase in pH. The gradual release of ammonium leads to the growth of LDH crystals with high crystallinity. The LDHs prepared by the urea method have a narrower particle size distribution compared to the LDHs prepared by the titration method using a basic solution and constant pH method.[94–101] Because of the generation of the carbonate anion from urea, the LDHs prepared by this method are commonly carbonate type. The use of hexamethylenetetramine (HMT) as the precipitating reagent of LDH enables the possibility to obtain LDHs with an interlayer anion other than carbonate given that the formaldehyde released from the hydrolysis of HMT is less plausible to be intercalated.[101–103]

10528 | *Chem. Soc. Rev.*, 2024, **53**, 10523–10574

This journal is © The Royal Society of Chemistry 2024

2.2.2. Preparation using a slurry of metal oxides/hydroxides as a scalable approach. Instead of using soluble metal salts, a method using metal oxides/hydroxides as starting materials has been developed for the preparation of LDHs.[104] For example, MgAl-deoxycholate-LDH was prepared via the hydrothermal treatment of an aqueous slurry of magnesium hydroxide (brucite) and aluminium hydroxide (gibbsite).[105] The selectivity of the bulky and monodentate deoxycholate anion as the interlayer anion of LDH was very low. It was not possible to obtain MgAl-deoxycholate-LDH by the co-precipitation method. Unlike co-precipitation, the initial mixture is slurry instead of a solution, and thus LDHs are formed by dissolution/recrystallisation under heating (commonly under hydrothermal conditions).

2.2.3. Preparation using solids by the solid-state reaction (mechanochemical method). Solid-state reaction can also be used to prepare LDHs.[106] To form LDHs from metal hydroxide and metal salts, mechanical forces such as compression, shear and friction are used to induce the reaction by simply grinding the starting materials with a mortar and pestle, or by using mills (ball mills and planetary mills). An LiAl-LDH was formed by grinding a mixture of $LiOH \cdot H_2O$ and $Al(OH)_3$ for 2–3 days, and then purging the mixture with water saturated with N_2 gas at room temperature.[107] The formation of the LDH was achieved by the incorporation of LiOH and H_2O into $Al(OH)_3$ particles during mechanical mixing. The LDH was not obtained when the mixture was not purged with water, showing the importance of water in promoting interparticle diffusion. MgAl-LDH with x of 0.33 was prepared by manually grinding hydrated metal salts including $Mg(NO_3)_2$ and $Al(NO_3)_3$ at room temperature,[108] where an NaOH pellet was added as the hydroxide source. Nitrate-intercalated LDH was obtained instead of carbonate LDH as the rapid reaction of the precursors prevented CO_3^{2-} contamination. The products were agglomerated platy LDH particles. Thus, the mechanochemical reaction of hydrated metal salts with atmospheric water (without the addition of water) is a way to synthesise LDH. To incorporate Sn^{4+} into the hydroxide layers, which is challenging using the conventional co-precipitation method, the preparation of CaSn-LDH was reported by applying two-step grinding including dry grinding, followed by wet grinding with the addition of water.[109] Dry grinding of $CaCl_2$ and $SnCl_2$ for 3 h was done for comparison. It should be noted that CaSn-LDH was not obtained by using the co-precipitation method. Similarly, one-step dry grinding did not produce LDH, given that the generation of a sufficient amount of hydroxide groups for the LDH structure from the introduced water was infeasible. The one-pot synthesis of organic molecules containing LDH was done by mechanical grinding with the addition of a small amount of solvent, the so-called liquid-assisted grinding process.[110]

The formation of organic anion-intercalated LDHs by mechanochemical reactions has also been reported.[111,112] MgAl-LDH intercalated with p-toluene sulfonate (p-TS-LDH), malonate (M-LDH), and oxalate anions (O-LDH) was synthesised by milling $Mg(OH)_2$ and $Al(OH)_3$ in a planetary ball mill for 1 h and subsequent milling with organic anions for another

1 h. The d values were 1.77, 0.88, and 0.86 nm for p-TS-LDH, M-LDH, and O-LDH, respectively. The aggregated particles with a size of over 700 nm were observed from the TEM image, together with small disk-shaped particles with a lateral size of ca. 150 nm. p-TS-LDH was used as the starting material for the anion exchange reaction with dodecyl sulphate anion. The X-ray diffraction (XRD) patterns showed an increase in the basal spacing from 1.77 nm to 3.09 nm, and the FT-IR results also confirmed the successful ion exchange.[112]

The mechanochemical synthesis of LDHs has the following advantages: (i) solid–liquid separation is not necessary, (ii) carbonate contamination is less plausible, and (iii) the starting materials are not expensive compared with that used for the conventional synthesis starting from an aqueous solution of metal salts. However, the variation in the metal combination, composition, and morphology of LDHs achieved by the mechanochemical method is still limited.

2.3. Characterisation of LDHs

2.3.1. Structure and composition of LDHs. Because of the difficulty of obtaining single crystals, powder diffraction is most commonly utilised to identify the structure,[113] the phase purity, and impurity phases of LDHs. The basal spacing of LDHs is expected to be larger when their layer charge density is lower, corresponding to a smaller x due to the weaker attractive force between the LDH layers and interlayer anions. The lattice parameter a, calculated as $a = 2d_{110}$, corresponds to the metal–metal distance in the hexagonal framework of LDH layers. Accordingly, different metal cations lead to a variation in the lattice parameter a due to the difference in ionic radius. The variation in the a parameter with x is often used to assess the successful substitution in LDH. In the case of poorly crystalline LDHs, various complementary techniques such as Fourier transform infrared (FT-IR) and Raman (FT-Raman) spectroscopy are employed.[113] The shift in the vibration frequency of the bonds between the metal and oxygen in LDHs due to the incorporation of M^{3+} in the framework was investigated using FT-Raman spectroscopy. For example, the shift in the Ni–O vibration was ascribed to the incorporation of Fe in $Ni(OH)_2$[114] and the incorporation of Fe and Co in NiFe- and NiFeCo-LDHs.[115] The presence of isolated metal hydroxides $(M^{2+}(OH)_2)$ as an impurity phase was discussed based on the characteristic O–H stretching vibration. The OH groups without hydrogen bonding (from isolated metal hydroxides) appeared at a different wavenumber region from the OH groups with hydrogen bonded to the adsorbed water and the interlayer anion from LDHs. Mg/Al ordering was examined by multinuclear nuclear magnetic resonance (NMR) spectroscopy.[116,117]

The composition of the products is determined by X-ray fluorescence (XRF) for solid samples and inductively coupled plasma emission spectrometry (ICP) after dissolving the products in an acidic solution. An energy dispersive X-ray fluorescence spectrometer (EDS) equipped with SEM or TEM is used to determine the distribution of metal cations and anions in the samples. Also, X-ray photoelectron spectroscopy (XPS) is

This journal is © The Royal Society of Chemistry 2024

Chem. Soc. Rev., 2024, **53**, 10523–10574 | **10529**

employed to analyse the elemental composition and oxidation states of the components.

2.3.2. Shape and size of LDH particle. Scanning electron microscopy (SEM) and transmission electron microscopy (TEM) are employed to observe the particle morphology of LDHs (shape and size of particles and surface texture). LDHs are sensitive to the electron beam and can be burned under the conditions for TEM observation. Thus, to prevent burning and avoid charging problems, the samples are coated with a platinum layer by sputtering. Surface probe microscopy (SPM) is also used, particularly atomic force microscopy (AFM), to explore the topology and surface texture of LDH particles, which may correlate with the location of the guest. 3D images can be generated based on the size and shape of the particles and their surface roughness. Dynamic light scattering (DLS) is used to determine the dynamic size and size distribution of LDH nanoparticles in suspension and can provide information about their aggregation behaviour.

2.3.3. Formation process of LDHs. By monitoring the change in pH, the formation of LDHs *via* the co-precipitation can be tracked. The milky appearance observed during the co-precipitation signals the initiation of nucleation and formation of LDHs. As the reaction progresses, the appearance, opacity, and texture of the mixture change, indicating the growth and aggregation of the LDH particles. *In situ* XRD gives real-time information on the formation of nuclei and crystals, phase transitions, crystal structure, and intercalation during the synthesis process with kinetic information. *In situ* small-angle X-ray scattering (SAXS) provides information on the structure and size of particles during their formation.

2.3.4. Thermal transformation of LDHs. Upon heating LDHs, the water molecules in the interlayer space are released, while the interlayer anions are decomposed or evaporated, together with the dehydroxylation of the brucite-like sheet, resulting in weight loss. Thus, to study these thermal reactions quantitatively and understand the decomposition process, thermogravimetric analysis coupled with differential thermal analysis (TG-DTA) is employed to measure the weight change in the sample as a function of temperature and detect exothermic or endothermic reactions. During heating, the structural change in LDHs is observed by *in situ* XRD, which can track the phase transformation, crystallinity changes and the formation of new phases that occur during the heating.

2.4. Synthetic efforts to vary composition of LDHs

For the functional design of LDHs, the main component (M^{2+}) and the second component (M^{3+}) are selected to satisfy the required function. In addition to the selection of the M^{2+}/M^{3+} combination, the M^{3+} content (or ($M^{3+}/(M^{2+} + M^{3+})$ or x) is also an important parameter to determine the properties of the resulting LDHs. However, there are several requirements in the selection of M^{2+} and M^{3+} from the preparation viewpoints including the solubility and stability of the available starting materials and solubility and stability of their hydroxides. Taking advantage of the facile synthesis of LDHs from solution and in the solid-state, as mentioned above, various synthetic

methods and conditions have been examined to prepare LDHs with desired compositions.[48–53,74,80,81,106] Hereafter, the reported examples of LDHs with varying ($M^{3+}/(M^{2+} + M^{3+})$) are summarised. To investigate the effects of x on the properties of LDHs, the preparation of LDHs with varying x is examined. LDHs with x of 0.20–0.33 have commonly been reported as pure LDH phase.[49,51] Even when x in the products was less than 0.20, the products were found to be a mixture of LDHs and impurity phases ($M^{2+}(OH)_2$) in many cases including MgAl-,[118,119] MgGa-,[120,121] NiAl-,[122,123] CoFe-,[124,125] CaAl-,[126] and CaFe-LDHs.[127] The limitation of x was claimed to be caused by the large distance between the adjacent interlayer anion in the interlayer space and the difference in the ionic radii of the divalent and trivalent metal cations in the brucite-like sheet.[48–52] However, the reasons for this limitation are not clearly understood. Therefore, the preparation of LDHs with varying x is still worth investigating.

In the case of co-precipitation using the titration method, the effect of the final pH of the suspension on x in the product was examined.[128] To control x in MgAl-LDHs intercalated with carbonate, the acidic solution containing $Mg(NO_3)_2$ and $Al(NO_3)_3$ with varying $M^{3+}/(M^{2+} + M^{3+})$ ratios (x') from 0.05 to 0.50 were used as starting solutions. An aqueous solution of NaOH containing $NaHCO_3$ was slowly added to the starting solution until the pH reached 9.5–11. Then, the resulting suspension was aged and dried for the crystallisation of LDHs. It was shown that x in the products was larger than x' (in the starting solution) when the final pH of the suspension was 9.5, indicating that a portion of magnesium in the starting solution did not precipitate at this pH. It was reported that the mechanism for the formation of MgAl-LDH by the titration method involves aluminium hydroxide precipitation in the pH range of 3.4–7.1, followed by magnesium precipitation (and to be incorporated in the pre-formed aluminium hydroxide) at pH above 8.5.[89,91] To enhance the precipitation of magnesium to achieve x in the products closer to x', titration was carried out to reach a pH in the range of 10–11. Although the pH was found to affect x in the products, the products were mixtures of LDHs and impurity phases when x in the product was 0.05 and 0.07.[128] It should be noted here that x in the product determined by ICP is not x of the LDH phase when the product is a mixture and it is difficult to determine the composition of the LDH phase in the mixture.

Miyata reported the preparation of MgAl-LDHs using a starting solution of metal chlorides at x' of 0.10–0.60 by co-precipitation at a constant pH.[118] The reaction was conducted at 40 °C with a constant pH of 10. The x in products was determined by chelatometric titration after dissolution with dilute HCl in the range of 0.25–0.33. Phase separation to LDHs and impurity phases such as MgAl-LDH and boehmite was often observed when x = 0.38–0.60 in the product, MgAl-LDH and hydromagnesite when x = 0.16–0.20, and MgAl-LDH, hydromagnesite and magnesium hydroxide when x = 0.10.[118] The constant pH method has been widely used to prepare LDHs such as MgFe-, NiAl-, NiFe-, ZnAl-, CuAl-, CoFe-, and CaAl-LDHs with varying x. However, single-phase LDHs were available for x

10530 | *Chem. Soc. Rev.*, 2024, **53**, 10523–10574

This journal is © The Royal Society of Chemistry 2024

Table 1 The difference in ionic radius (nm) between M^{2+} and M^{3+} (in percentage) for possible LDHs. The percentage difference in ionic radius between M^{2+} and M^{3+} was calculated using the equation of $100 \times (R_M{}^{2+} - R_M{}^{3+})/R_M{}^{2+}$. Numbers with − indicate M^{3+} is larger than M^{2+}. The ionic radius is from Shannon's report[129]

		M^{2+}							
		0.069	0.072	0.073	0.074	0.075	0.078	0.083	0.1
M^{3+}		Ni	Mg	Cu	Zn	Co	Fe	Mn	Ca
0.054	Al	22	26	27	28	28	31	36	47
0.055	Co	21	24	25	26	27	30	34	46
0.062	Cr	11	15	16	17	17	21	26	39
0.062	Ga	10	14	15	16	17	21	25	38
0.065	Fe	6	10	12	13	13	17	22	36
0.08	In	−16	−11	−10	−8	−7	−3	4	20

in 0.20–0.33, and phase separation into LDH and impurity phase was observed when $x < 0.20$ or $x > 0.30$ in many cases.

Taking advantage of the size matching between Mg^{2+} (0.072 nm) and Ga^{3+} (0.062 nm),[129] the possibility of the extension of x was investigated in MgGa-LDHs (Table 1).[120,121] MgGa-LDHs with x of 0.12–0.33 in the product were obtained by co-precipitation at a constant pH in the range of 11–12, using acidic solutions of $Mg(NO_3)_2$ and $Ga(NO_3)_3$ and basic solutions of NaOH and Na_2CO_3. The product with x of 0.07 was found to consist of a mixture of LDH and magnesium hydroxide. It was observed that MgGa-LDH was prepared without phase separation at a smaller x compared to MgAl-LDH, as reported by Miyata.[118] More recently, the preparation of MgGa-LDHs with iodide (MgGa-I-LDHs) with x of 0.06–0.24 was examined by co-precipitation from aqueous solutions of sodium iodide, magnesium nitrate and gallium nitrate, using the constant pH method, where the bulky I^- ion was thought to play a role in suppressing their collapse when x was 0.06.[130] The relationship between the lattice parameter a and x in the reported MgGa-LDHs is summarised in Fig. 6. There was a linear relationship between a and x, confirming the successful quantitative incorporation of Ga.[130–133]

Dioctyl sulfosuccinate was used for the preparation of NiFe-LDHs with x of 0.05–0.25.[134] NiFe-LDHs with a wide range of x were expected because of the similar ionic size of Ni^{2+} (0.069 nm) and Fe^{3+} (0.064 nm), while phase separation has been reported. By using dioctyl sulfosuccinate as the interlayer anion, NiFe-LDHs with $x < 0.20$ were obtained by co-precipitation at a constant pH. The interlayer dioctyl sulfosuccinate was replaced with the carbonate anion by a common ion exchange method using an aqueous solution of sodium carbonate to obtain NiFe-LDH carbonates. The basal spacings of the NiFe-LDH carbonates varied depending on x, as shown in Fig. 7.[134–143] NiFe-LDHs with x of 0.05–0.25 were obtained by co-precipitation from an aqueous solution of nickel nitrate and iron nitrate containing glycerol.[144]

Co-precipitation during the hydrolysis of urea and HMT has also been employed to prepare LDHs with varying x. Most of the reported studies focused on the common range of x (0.20–0.33). Carbonate-type NiAl-LDHs with x of 0.22–0.33 and NiFe-LDHs with x of 0.21–0.34 were prepared by the hydrolysis of urea or
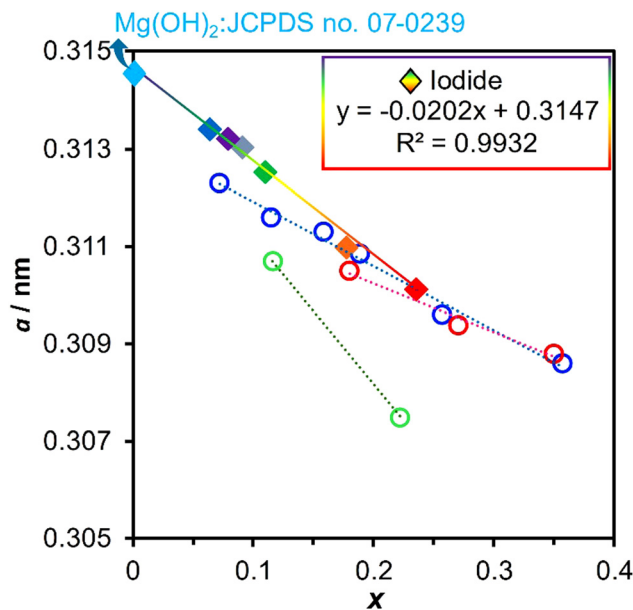

Fig. 6 Relationships between the lattice parameter a and composition x in the reported MgGa-LDHs. Diamonds are for iodide-type MgGa-LDHs[130] and circles are for the carbonate-type MgGa-LDHs.[131–134]

HMT. The synthesis for NiAl-LDHs was conducted at 180 °C for 72 h in air, while for NiFe-LDH, it was conducted at 100 °C for 48 h.[142,145] NiFe-LDH and CoAl-LDH with varying x were prepared using an aqueous solution of metal salts with $x' < 0.20$ by the hydrolysis of urea, while the composition of the products was not reported.[142,146]

The preparation from a slurry of metal oxides/hydroxides has been examined. The preparation of ZnAl-LDHs intercalated with the benzene sulfonate anion (BS) was investigated under hydrothermal conditions using ZnO and $Al(OH)_3$ as the starting materials. The formation of single-phase LDH was observed at x' of 0.4, while the starting materials were detected by XRD as impurity phases when x' was 0.20, 0.25, and 0.33. The remaining amount of the starting materials decreased when the amount of BS increased, resulting in single-phase ZnAl-LDH with $x = 0.33$. Alternatively, the ZnO remained when starting slurries with the Zn : Al : BS ratios of 4 : 1 : 1 and 4 : 1 : 2 ($x' = 0.20$) were employed.[147] In the case of MgAl-LDH with deoxycholate, the basal spacing varied depending on the x in the products.[105]

The preparation of LDHs with varying x by mechanochemical reaction has been reported.[106] $Mg(OH)_2$ and $Al(OH)_3$ were mixed with $x' = 0.14$–0.25 in a planetary ball mill for 15 min, resulting in the formation of MgAl-LDH with x of 0.25.[126] A part of $Mg(OH)_2$ was unreacted when x' was 0.14 and 0.20. Cl^-, $NO_3{}^-$, and $SO_4{}^{2-}$-intercalated MgAl-LDHs were prepared by using planetary ball mills to mix $Mg(OH)_2$ and aluminium salts ($AlCl_3$, $Al(NO_3)_3$ and $Al_2(SO_4)_3$) for 3–15 min, followed by washing the product with deionised water.[148] However, although the formation of an LDH with the targeted interlayer anion was confirmed, the $Al^{3+}/(Mg^{2+} + Al^{3+})$ ratio of the product was found to be smaller than the initial ratio of precursors. Accordingly, the importance of the precursor composition in the formation
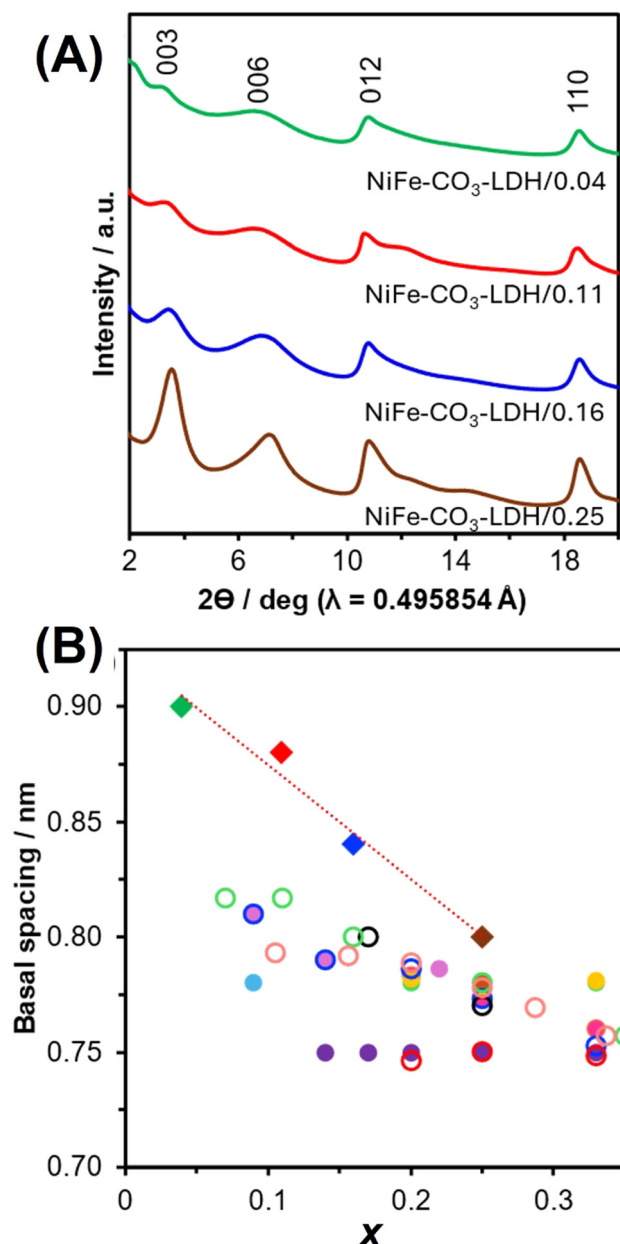
This journal is © The Royal Society of Chemistry 2024

Chem. Soc. Rev., 2024, **53**, 10523–10574 | **10531**

Fig. 7 (A) XRD patterns of NiFe−CO$_3$-LDH/x, where x is 0.04, 0.11, 0.16, and 0.25. (B) Relationship between the basal spacing and x. Diamonds are values for NiFe−CO$_3$-LDH/x,[134] closed circles are values reported for NiFe−CO$_3$-LDHs,[135–140] and open circles are values reported for MgAl−CO$_3$-LDHs,[118,141] MgGa−CO$_3$-LDHs,[133] MgFe−CO$_3$-LDHs,[142] and NiAl-CO$_3$-LDHs.[143]

of LDHs by mechanochemical milling was studied. Mg(OH)$_2$ and Al(OH)$_3$ (at Al^{3+}/(Mg^{2+} + Al^{3+}) ratios of the precursor = 0.14–0.25) were mixed in a planetary ball mill for 15 min at room temperature. The results yield MgAl-LDH when the initial Al^{3+}/(Mg^{2+} + Al) ratio was 0.25, whereas Mg(OH)$_2$ was unreacted when the initial Al^{3+}/(Mg^{2+} + Al^{3+}) ratio was 0.14 and 0.20.

Redox reaction has been employed to vary x in CoFe-, CoNi-, and CoCo-LDHs by using metal hydroxides as the starting materials.[124,149–151] Hydroxides of divalent transition metal cations (TM^{2+}(OH)$_2$) were prepared by precipitation using the hydrolysis of HMT under nitrogen gas bubbling. Some portions of divalent transition metal cations in the brucite were oxidised to trivalent form by oxidation using iodine (I$_2$) or bromine (Br$_2$). Meanwhile, the oxidising agent was reduced to iodide (I$^-$) or bromide (Br$^-$), and then intercalated into the interlayer space after the reaction. LDHs consisting of Co^{2+} and Fe^{2+} with varying Fe^{2+}/(Co^{2+} + Fe^{2+}) ratios of 0.17–0.33 were oxidised using iodine for 168 h under nitrogen gas protection, resulting in the formation of Co^{2+}Fe^{3+}-LDHs intercalated with iodide for the sample with an Fe^{3+}/(Co^{2+} + Fe^{3+}) ratio of 0.33. However, the phase separation to Co^{2+}Fe^{3+}-LDH and Co^{2+} hydroxide was observed when the Fe^{3+}/(Co^{2+} + Fe^{3+}) ratios of the starting mixture were in the range of 0.17–0.20.[124,151] Green rust is another example of an LDH obtained by the redox process with the general formula of $[\text{Fe}^{2+}_{1-x}\text{Fe}^{3+}_x(\text{OH})_2]^{x+}\cdot(x/n)[\text{A}^{n-}]^{x-}\cdot m[\text{H}_2\text{O}]$ (A^{n-}: interlayer anions, H$_2$O: interlayer water molecules).[152] Because of the poor stability, the application of green rust was limited.[153] However, green rust with remarkable stability was obtained from Fe^{3+} chloride and glycerol by the partial reduction and precipitation during the hydrothermal reaction.[154] The remarkable stability was explained by the less defective particle surface and dense interlayer structure, which suppress the diffusion of oxygen to oxidize Fe^{2+} in the hydroxide sheet.

The preparation of LDHs with $x < 0.20$ or $x > 0.30$ has been attempted thus far, as summarised in Table 2.

2.5. Characteristics and application of LDHs

2.5.1. Basal spacing and the expansion (swelling). It has been reported that the basal spacings of CaAl-,[169] MgAl-,[159,170] MgFe-,[165] and NiAl-LDHs[145] were larger when x was smaller. Furthermore, delamination and film fabrication of LDH can be substantially influenced by x. LDH of common x possesses a high charge density ($\sim$4(+) nm^{-2}) compared with the smectite group of clay minerals, which has a layer charge density of $\sim$0.5(−) nm^{-2}. Consequently, the delamination of LDH in water is difficult, while the smectite group of clay minerals swells in water, which will be introduced in Section 4 of the present review.

2.5.2. Anion exchange for the collection of anions. The anion exchange capacity and kinetics of the ion exchange are governed by x in LDH. A larger x resulted in higher adsorption properties towards anionic dye molecules.[171] MgFe- and MgAl-LDHs prepared from the starting solution with x' of 0.20 exhibited higher adsorption rates of perchlorate,[156] nitrate, and nitrite[172] than that with x' of 0.33. A smaller x resulted in a larger interlayer space and lower affinity, which had a reverse effect on the adsorption.[173]

2.5.3. Surface properties for application as catalysts. The basic properties of MgAl-LDH are also known to be affected by x.[174,175] The basic sites in the alkali earth oxide component can originate from O^{2-} (strong basicity), O species near hydroxyl groups (medium strength) and OH groups (weak). The addition of Al^{3+} alters the acid: base site distribution through the introduction of Al^{3+}–O^{2-} sites, which are of moderate Lewis

10532 | Chem. Soc. Rev., 2024, 53, 10523–10574

This journal is © The Royal Society of Chemistry 2024

Table 2 Summary of the previous reports on the preparation of LDHs with varying x values

M^{2+} M^{3+}		Interlayer anion	x'	x	By-product	Preparation			Atmosphere	Objective	Ref.
						Method	Temp. (°C)	Aging time			
Mg	Al	Cl^- and CO_3^{2-}	0.29	0.29	n.d.	2.2.1 (a-ii) (pH = 10)	60	24 h	Air	Nitrate ion exchanger	155
		CO_3^{2-}	0.20–0.33	n.r.	n.d.	2.2.1 (a-ii) (at 25 °C)	75		Air	Precursor of metal oxide for perchlorate adsorption	156
		Cl^- and CO_3^{2-}	0.20–0.33	0.20–0.33	n.d.	2.2.1 (a-ii) (pH = 10)	70	24 h	N_2 for Cl-type	Adsorption of norfloxacin	157
		CO_3^{2-}	0.02–0.50	0.33–0.50	n.d.	2.2.1 (a-i) (pH = 9.5, 10, 10.5, 11)			Air	Fundamental study	88
		CO_3^{2-}	0.20–0.33	n.r.	n.d.	2.2.1 (a-i) (pH = 10.5)	30	1 h	Air	Precursor of metal oxide for antimonate removal	158
		CO_3^{2-}	0.20–0.33	n.r.	n.d.	2.2.1 (a-ii) (at 40 °C, pH = 10–11)	65	18 h	Air	Adsorption of nitrate and nitrite ions	159
		NO_3^-	0.20–0.33	n.r.	n.d.	2.2.1 (a-ii) (at 65 °C for 30 min)	120	24 h	Air	Adsorption of chloride ions	160
		NO_3^-	0.20, 0.33	0.18, 0.33	n.d.	2.2.1 (a-ii) (at 30 °C, pH = 10.5)	55	18 h	N_2	Adsorption of arsenate and iron ions	161
		Terephthalate and benzoate	0.18–0.43	0.18–0.50	n.d.	2.2.1 (a-ii) (pH = 10)			Air	Fundamental study	162
Mg	Al	Cl^-	0.10–0.61	0.10–0.60	Boehmite (x = 0.38–0.60), n.d. (x = 0.25–0.33), Hydromagnesite (x = 0.16–0.20), Hydromagnesite + $Mg(OH)_2$ (x = 0.10)	2.2.1 (a-ii) (at 40 °C, pH = 10)				Fundamental study	118
		CO_3^{2-}	0.17–0.33	0.17–0.33	n.d.	2.2.1 (a-ii)			Air	Catalyst for aromatic nitrile hydrolysis	131
		OH^- and Cl^-	0.14–0.33	n.r.	$Mg(OH)_2$ (x' = 0.14, 0.20, 0.25 and 0.33)	2.2.2	110	5–10 days	Air	Fundamental study	163
		CO_3^{2-}	0.14 and 0.20	n.r.	$Mg(OH)_2$ + MgO (x' = 0.14 and 0.20)	2.2.2	110	5–10 days	Air	Fundamental study	119
		CO_3^{2-}	0.14–0.25	0.14–0.25	n.d. (x = 0.25), $Mg(OH)_2$ (x = 0.14–0.20)	2.2.3		Milling for 15 min			
Mg	Ga	CO_3^{2-}	0.07–0.33	0.07–0.33	n.d. (x = 0.12–0.33), $Mg(OH)_2$ (x = 0.07)	2.2.1 (a-ii) (at 40 °C, pH = 11–12)			N_2	Fundamental study	120 and 121
		NO_3^- and CO_3^{2-}	0.18	0.18	n.d.	2.2.1 (a-ii) (pH = 9.5)	25	18 h	Air	Fundamental study	164
		CO_3^{2-}	0.14–0.25	0.12–0.25	n.d.	2.2.1 (a-ii) (pH = 9–10)			N_2	Catalyst for aromatic nitrile hydrolysis	131
Mg	Fe	Cl^- and CO_3^{2-}	0.16	0.16	n.d.	2.2.1 (a-ii) (pH = 10)	25	24 h	Air	Nitrate ion exchanger	155
		CO_3^{2-}	0.20–0.33	n.r.	n.d.	2.2.1 (a-ii) (at 25 °C)	75		Air	Precursor of metal oxide for perchlorate adsorption	156
		CO_3^{2-}	0.20–0.33	n.r.	n.d.	2.2.1 (a-ii) (pH = 10)	80	24 h in oven	Air	Adsorption of copper, cobalt, and cadmium ions	165
		NO_3^-	0.17–0.33	n.r.	n.d.	2.2.1 (a-i) (at 25 °C for 30 min)	110	10 h	Air	Adsorption of fluoride and arsenate ions	143
		Cl^-	0.20–0.33	n.r.	n.d. (x' = 0.33; reaction at 25–100 °C), n.d. (x' = 0.25; reaction at 25–125 °C)	2.2.1 (a-ii) (pH = 10)	25–150	48 h	N_2	Fundamental study	166

This journal is © The Royal Society of Chemistry 2024

Chem. Soc. Rev., 2024, **53**, 10523–10574 | 10533

Table 2 (continued)

M²⁺	M³⁺	Interlayer anion	x'	x	By-product	Preparation Method	Temp. (°C)	Aging time	Atmosphere	Objective	Ref.
Ni	Al	CO_3^{2-}	0.17–0.33	0.17–0.33	n.d. (x' = 0.20; reaction at 25–150 °C)	2.2.1 (a-i) (pH = 10.5)	40	1 h	Air	Catalyst for oxidation of ethylbenzene	65
		CO_3^{2-}	0.20–0.33	0.22–0.33	n.d. (x = 0.33)	2.2.1 (b)	180	72 h	Air	Pseudocapacitor	145
		NO_3^-	0.10–0.33	0.10–0.33	$Ni(OH)_2$ (x = 0.10, 0.17)	2.2.1 (a-ii) (pH = 10)	75–80	16 h	N_2	Characterisation of electrochemical behavior	122
		CO_3^{2-}	0.09–0.33	0.09–0.33	n.d. (x = 0.17–0.33) $Ni(OH)_2$ (x = 0.09, 0.11)	2.2.1 (a-i) (at 25 °C, pH = 11–12)			Air	Precursor of metal oxide using as catalyst for reforming of methane	123
		Cl^-	0.09–0.33	0.09–0.33	n.d.	2.2.1 (a-i)	100	20 h	Air	Fundamental study	135
Ni	Fe	Cl^- and CO_3^{2-}	0.21	0.21	n.d.	2.2.1 (a-ii) (pH = 10)	120	24 h	Air	Nitrate ion exchanger	155
		Cl^-	0.20–0.33	n.r.	n.d.	2.2.1 (b)		6 h under reflux condition	Air	Electrocatalyst for water splitting	66
		CO_3^{2-}	0.09–0.17	n.r.	n.d.	2.2.1 (b)	150	48 h	Air	Electrocatalyst for oxygen evolution	115
		CO_3^{2-}	0.20–0.33	0.21–0.34	n.d.	2.2.1 (b) (at 25 °C for 24 h)	100	48 h	Air	Electrochemical glucose sensing	137
Zn	Al	CO_3^{2-}	0.20–0.33	n.r.	n.d.	2.2.1 (a-ii) (at 25 °C)	75		Air	Precursor of metal oxide for perchlorate adsorption	156
		NO_3^-	0.20–0.33	n.r.	n.d.	2.2.1 (a-ii) (at 65 °C for 30 min)	120	24 h	Air	Adsorption of chloride ion	131
		Benzene sulfonate	0.20–0.40	n.r.	n.d. (x' = 0.40) ZnO (x' = 0.20, 0.25 and 0.33)	2.2.2	150	24 h	Air	Fundamental study	147
Cu	Al	CO_3^{2-}	0.20–0.67	n.r.	Malachite	2.2.1 (a-ii) (at 40 °C)	40	15 min	Air	Fundamental study	167
Co	Al	CO_3^{2-}	0.14–0.80	n.r.	n.d. (x' = 0.33)	2.2.1 (b) (in methanol)	150	12 h	Air	Precursor of metal oxide using as catalyst for 4-nitrophenol reduction	168
Co	Fe	I^-	0.17–0.33	0.33	n.d. (x' = 0.33) $Co(OH)_2$ (x' = 0.20–0.25)	2.2.2.	25	168 h	N_2	Fundamental study	124 and 125
Ca	Al	Cl^- and CO_3^{2-}	0.26	0.26	n.d.	2.2.1 (a-ii) (pH = 10)	25	24 h	Air	Nitrate ion exchanger	155
		Cl^-	0.14–0.33	0.20–0.33	n.d. (x' = 0.20–0.33) $Ca(OH)_2$ + $Ca(CO)_3$ (x' = 0.14, 0.17)	2.2.1 (a-i)	25	1 h	Air	Removal of copper, nickel, zinc, chromium, and phosphate ions	126
		NO_3^-	0.20–0.33	n.r.	n.d.	2.2.1 (a-ii) (at 65 °C for 30 min)	120	24 h	Air	Adsorption of chloride ion	160
Ca	Fe	Cl^-	0.14–0.33	0.33	n.d. (x' = 0.33) $Ca(OH)_2$ (x' = 0.14–0.25)	2.2.1 (a-i) (pH = 13)	25		N_2	Fundamental study	127

Note: x' is the $M^{3+}/(M^{2+} + M^{3+})$ ratio of the initial solution of metal salts, and x is the $M^{3+}/(M^{2+} + M^{3+})$ ratio of the product. "n.r." indicates "not reported", and "n.d." indicates "not detected".

10534 | Chem. Soc. Rev., 2024, 53, 10523–10574

This journal is © The Royal Society of Chemistry 2024

acidity and only medium basicity.[176] A series of MgAl-LDH with tuneable basicity was prepared in the range $x = 0.25$–0.55 (all resulting materials were found to exhibit characteristic XRD patterns of the hydrotalcite phase). When the Mg content was higher, a steady increase in lattice parameter was observed with a concomitant increase in the basal spacing.[177] NiAl-LDH prepared from the starting solution with x' of 0.20 exhibited greater catalytic activity for the oxidation of ethylbenzene compared with NiAl-LDH with x' of 0.33.[65] According to several reports in the literature, transition metal-containing LDHs show different catalytic activity as a function of x.[178–182] For instance, CuAl-CO$_3$-LDH with the Cu/Al ratio of 2/1, 3/1 and 4/1 ($x = 0.33$, 0.25 and 0.2, respectively) resulted in different phenol conversion of 47.5%, 53.5% and 56.0%, respectively.[181] The effect of x on the catalytic reactions was also reported when LDH was used as a catalyst support.[182]

2.5.4. Controlled release of functional species from LDHs. Controlled release is an important application of LDHs.[183] The dependence of adsorption capability on x is also correlated with the release of the anions from LDHs. It was reported that x affects the kinetics and the amount of inorganic oxo-anions released such as borate and nitrate.[184] The release of vanillic acid from ZnAl-LDH was faster and had a higher release pattern for the LDH with a high Al^{3+} content, suggesting the higher affinity between vanillic acid and LDH.[185]

The surface charge of drug delivery materials is a factor affecting their cellular uptake given that they should interact with negatively charged cellular membranes.[186] Controlling the x of LDH resulted in varying charges of the LDH surface to modify their cellular interactions.[187–189]

2.5.5. Diagnostic and medical application of LDHs by the incorporation of functional elements. An interesting approach to incorporate heteroelements into LDHs was developed by Oh et al.[190–192] LDHs labelled with contrasting moieties such as gadolinium (Gd) complex and metallic nanoparticles for magnetic resonance imaging (MRI) and X-ray computed tomography (CT) have been reported.[190–192] For these diagnostic and medical applications, the key components (Co-57 and Ga^{3+} in the reported examples) are required to be immobilised in the brucite-like sheet using other components (non-toxic and suitable surface charge and particle size) for their delivery to the target. LDHs prepared by hydrothermal reaction are suitable for biological application due to their phase purity and well-defined and appropriate particle size. The preparation of well-defined LDHs through hydrothermal reaction requires a longer time, and thus is not a compatible method to prepare LDHs incorporating radionuclides with a short half-life (e.g., $t_{1/2}$ of ^{68}Ga and ^{44}Sc are 68 min and 3.97 h, respectively). Accordingly, MgAl-LDH with a particle diameter of 150 nm was synthesised and radionuclide Co-57, a single photon emission computed tomography (SPECT)-sensitive RI, was incorporated in the LDH framework post-synthetically by treating the pre-synthesised LDHs with 880 mCi of ^{57}CoCl$_2$ solution per 5 mg of LDH under hydrothermal conditions at 150 °C for 2 h.[191] This post-synthetic incorporation method under hydrothermal conditions was applied to Ga^{3+}. Given that ^{68}Ga is a well-known

PET imaging agent, Ga-containing LDHs can be an alternative contrasting agent. Both cases showed the successful introduction of the target cations (Co-57 and Ga^{3+}), while preserving the crystallinity and particle size of LDH. Achieving this with Ga^{3+} within a short time is especially challenging given that the LDH is spontaneously dissolved upon encountering aqueous Ga^{3+} salt solution due to the strong acidity of aqueous Ga^{3+} salt solution, resulting in dissolution–reprecipitation rather than the incorporation of Ga^{3+}. Thus, to solve this problem, Ga(OH)$_4$ species was generated by the reaction of aqueous Ga^{3+} solution with NaOH, and subsequently reacted with LDH.[192]

2.6. Summary and perspectives

As mentioned for the incorporation of a useful isotope, Co-57, into the LDH framework for diagnostic applications,[17] multiple (more than three) components of layered hydroxides have been prepared for application as catalysts including (photo)electro-catalysts and adsorbents. A third component has been incorporated by the post-synthetic treatment of pre-synthesised LDHs and co-precipitation. Single atomic Ru, Rh and Au were reported to be anchored on sheets of ZnCr-, NiFe-, CoFe- and FeCoNi-LDHs,[193–197] while some ions were reported to be located in the brucite-like sheets such as Fe^{2+} in NiFe-LDH[198,199] and Fe^{3+} in MgAl-LDH.[200] The incorporation of Bi in ZnAl-LDH and V in NiFe-LDH was reported, where the important roles played vacancies were pointed out.[201,202]

The incorporation of La was reported to affect the adsorption of metal oxo-anions such as arsenate and tungstate onto CuMgFe- and MgFe-LDHs.[203,204] The incorporation of La^{3+} in brucite-like sheets by isomorphous substitution was not favoured. The size of the octahedra in the LDH sheets is determined by the size of the divalent cations, such as Mg^{2+} (ionic radius of 0.072 nm). The Fe^{3+} ions have an even smaller ionic radius (0.065 nm) and their preferentially adopted coordination number is 6. Thus, because of the larger ionic radius of La^{3+} (0.136 nm) with higher coordination numbers ranging from 7 to 10, the isomorphous substitution of Fe^{3+} with La^{3+} in MgFe-LDH is not favoured. The formation of carbonate and oxy-hydroxide phases of La^{3+} on the surface of the LDH sheets was seen in the attempt to incorporate La^{3+} in MgFe-LDH. Recently, it was reported that the incorporation of La^{3+} in the brucite-like sheet was possible by optimising the synthetic parameters using an ammonia alkaline solution for the preparation.[205] Thermally activated purple-to-blue luminescence was reported for CoMgAl-LDHs, which were prepared by co-precipitation.[206] Thus, the incorporation of a third (or the fourth) component into LDHs and preparation of layered triple (quadruple) hydroxides are a direction for materials design. In this direction, synthetic efforts are still necessary to achieve the quantitative introduction of multiple components into the final products. Appropriate characterisation to discuss the location of the incorporated elements is another challenge, which needs to be addressed.

To satisfy the requirements for the above-mentioned versatile applications (anion exchangers, catalysts, polymer additives, and drug/gene carriers), as well as to find novel

This journal is © The Royal Society of Chemistry 2024

Chem. Soc. Rev., 2024, **53**, 10523–10574 | **10535**

applications, the hybridisation of LDHs with various functional particles has been reported to design materials with modified, improved, and multiple functions.[207] In the extended application by hybridisation, the precise design of the composition of LDHs has important roles, and consequently their detailed characterisation will be more challenging.

3. Layered alkali silicates

A variety of crystalline and amorphous silicas exist, which are composed of an $[SiO_4]^{4-}$ tetrahedron with varying connections (Fig. 8), where the elemental substitution of Si with heteroelements is possible. As a known example in nature, the substitution of Si in quartz with iron is the origin of the purple-colour of amethyst (Fig. 1). Silicate glasses doped with rare earth (for example Sm^{2+} and Eu^{3+}) and transition metal ions (for example Mn^{3+} and Cu^{2+}) exhibit useful optical (including luminescent) properties, showing possible application in phosphors (including lasers), optical recording, sensors, etc.[208,209]

The connection of $[SiO_4]^{4-}$ tetrahedron leads to silica/silicate of varying three-dimensional structures. Silica/silicate-based nanoporous materials (silica gels, mesoporous silicas and zeolites) with varying pore sizes have been investigated for adsorption/separation and catalysis. To impart catalytic functions and modify the surface properties for adsorption, the introduction of heteroelements such as Al^{3+}, B^{3+}, Ga^{3+}, Fe^{3+}, Ti^{4+}, V^{4+}, Sn^{4+}, and Zr^{4+} into the frameworks of silicas has been conducted.[210] For example, Ti-containing mesoporous silicas and zeolites have been prepared by the isomorphous substitution of Si^{4+} with Ti^{4+} during the preparation of silicas/silicates and used as (photo)catalysts. The incorporated Ti exists as isolated tetrahedrally coordinated species in the silica/silicate frameworks at a low Ti content (the upper limit of its framework incorporation was Ti/Si > 30/1).[11] Metal oxide may segregate out of their frameworks when the loading of the heteroelement increases.

Phyllosilicates are abundant in nature, which are commonly found as aluminium silicates and magnesium silicates, where gibbsite and brucite-like hydroxide sheets play a key role in directing layered structures (these materials will be introduced in Section 4 of this review). Alternatively, some layered silicic acids and their alkaline salts are composed of $[SiO_4]^{4-}$ tetrahedrons.[43,211,212] These layered silicic acids/silicates with varying structures (varying connection of $[SiO_4]^{4-}$ tetrahedron resulting in varying layer thicknesses) are available and the notable examples are introduced in Table 3.[213–217] Some of them are found in nature, for example, kenyaite ($Na_2Si_{20}O_{41}\cdot nH_2O$) and magadiite ($Na_2Si_{14}O_{29}\cdot nH_2O$) were found at Lake Magadi, Kenya in 1967.[218] The layered alkali silicates introduced in Table 3 have been synthesised by hydrothermal reactions in the laboratory for different applications.[219–222]

The isomorphous substitution of Si^{4+} with heteroelements may lead to novel functional layered silicates. Here, the synthetic methods for the incorporation of heteroelements, examples of the heteroelements and their amount, characterisation, and the expected (achieved) functions reported thus far are introduced. The isomorphous substitution of Si^{4+} in layered alkali silicates with heteroelements (Al^{3+}, Ti^{4+}, etc.) has been reported,[212] as summarised in Table 4.[223–248] One of the motivations for substitution is the application of heteroelement-containing layered alkali silicates as the precursors of zeolites and mesoporous silicas as catalysts and adsorbents with designed material performances connected with the incorporated heteroelements.[232–238] Due to the similarity in the local structure of the $[SiO_4]^{4-}$ network, some layered alkali silicates have been converted to zeolites topochemically.[249–251] It is worth noting that some zeolites (framework types: NSI, CDO, RWR, RRO, etc.) are available only by topotactic conversion of layered silicates such as Nu-6(1), PLS-1, octosilicate, and RUB-39.[252–255]

In addition to substitution in the silicate layer, defects as microchannels in the silicate layer are considered to be the key
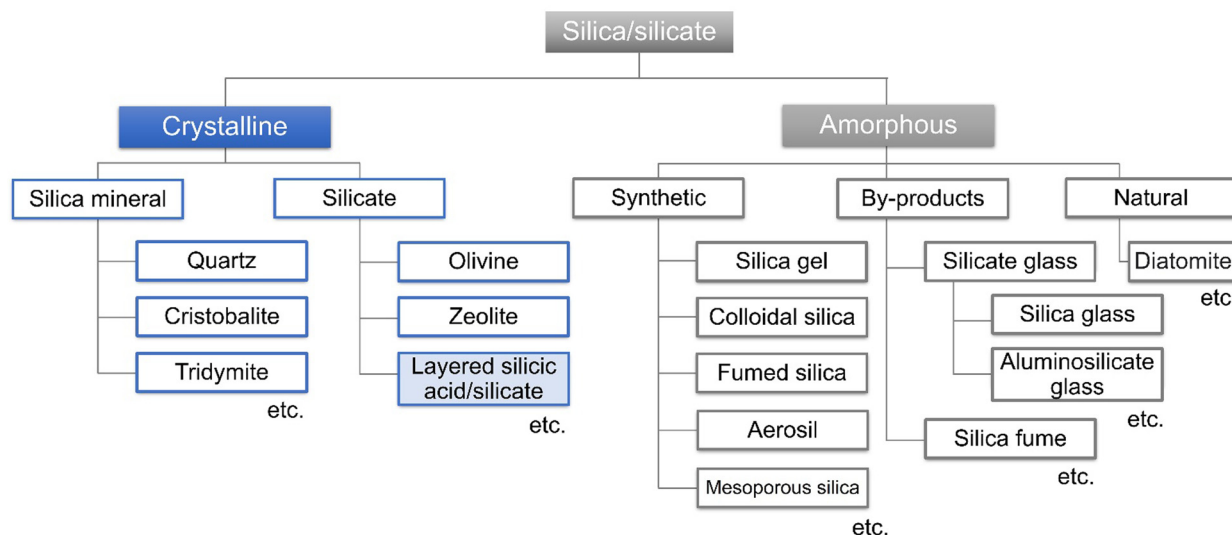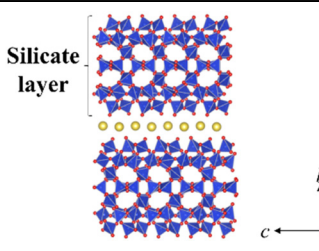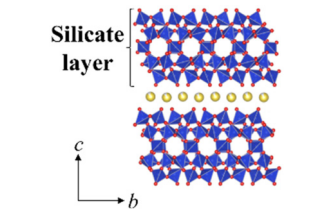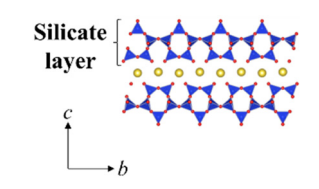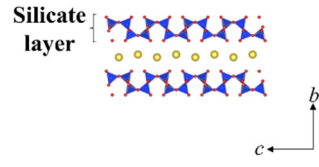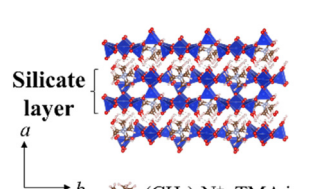

Fig. 8 Classification of crystalline and amorphous silica/silicates.

10536 | Chem. Soc. Rev., 2024, 53, 10523–10574

This journal is © The Royal Society of Chemistry 2024

Table 3 Examples of layered silicates (the crystal structure was drawn using the VESTA program[44])

Layered silicate[a]	Structure[a] ▲ SiO$_4$ tetrahedra ○ Na$^+$	Thickness of layer/nm	Ideal cation exchange capacity (meq g^{-1})	Ref.
Kenyaite Na$_{16}$[Si$_{160}$O$_{320}$(OH)$_{16}$]·64H$_2$O		1.6	1.4	213
Magadiite Na$_2$[Si$_{14}$O$_{28}$(OH)$_2$]·8H$_2$O		1.1	2.0	214
Octosilicate Na$_8$[Si$_{32}$O$_{64}$(OH)$_8$]·32H$_2$O		0.74	2.8	215
Kanemite NaH[Si$_2$O$_5$]·3H$_2$O		0.49	4.7	216
HUS-1 Si$_{10}$O$_{24}$H$_6$·2[(CH$_3$)$_4$N]		0.90	2.4	217

(CH$_3$)$_4$N$^+$: TMA ions

[a] Water molecules are omitted for clarity.

for some functions. Magadiite showed the selective adsorption of benzoic acid from acetonitrile solution, where its microchannel was thought to play a role in its selectvity.[256] Layered silicic acid/alkali silicates are characterised by regularly arranged reactive silanol groups on the layer surface, which can be used for cation exchange and grafting to obtain intercalation compounds of controlled nanostructures.[257–261] The chemical/thermal stabilities and reactivity of layered silicates/ silicic acids vary depending on the structures (derived from the composition), and thus the development of novel layered alkali silicates has been reported.[262] For example, layered silicates named Hiroshima University Silicate (HUS) series were synthesised by hydrothermal reactions as adsorbents and catalyst precursors.[217,263,264]

3.1. The amount of the heteroelement to be doped in the silicate layer and the structural transformation

The acidity generated by the isomorphous substitution of Si^{4+} with heteroelements of lower valency and similar sizes, such as Al^{3+}, Ga^{3+}, and B^{3+} has been investigated.[223,224,226–229,231–234,236,239–244,247,248] Layered silicic acid/alkali silicates have weak Brønsted acid sites owing to their silanol groups on the layer surface.[249] Al is the element conveniently used to substitute Si in the silicate framework, as seen in many crystalline silicates (zeolites) and amorphous silicas (including mesoporous silicas). To impart acidity, Al-containing magadiites have been prepared by the hydrothermal reaction starting from Si and Al sources (sodium metasilicate and aluminium tri(isopropoxide); initial

This journal is © The Royal Society of Chemistry 2024

Chem. Soc. Rev., 2024, **53**, 10523–10574 | **10537**

Table 4 Summary of the isomorphous substitution of Si^{4+} of various layered alkali silicates with heteroelements (HE)

Layered silicate	Composition	HE	Effective ionic radii^a/nm	HE source	HE/Si atomic ratio (initial)	HE/Si atomic ratio (products)	Preparation^b	Characterisation	Objective	Ref.
Magadiite	$Na_2Si_{14}O_{29}$	Al^{3+}	0.039	Al_2O_3	—	1/17.1–1/53.4	HTR (130 °C) and 120 h	^{27}Al MAS NMR	Characterisation of acid sites	223
Magadiite	$Na_2Si_{14}O_{29}$	Ga^{3+}	0.047	$Ga_2(SO_4)_3\cdot 13H_2O$	—	1/21.3–1/23.6	HTR (130 °C) and 120 h	FT-IR spectra of adsorbed pyridine	Characterisation of acid sites	223
Magadiite	$Na_2Si_{14}O_{29}$	Al^{3+}	0.039	$Al[OCH(CH_3)_2]_3$	1/15–1/60	1/15–1/69	HTR (150 °C) and 12 or 24 h	^{27}Al and ^{29}Si MAS NMR, and FT-IR spectra of adsorbed CO	Characterisation of acid sites	224
Magadiite	$Na_2Si_{14}O_{29}$	Sn^{4+}	0.055	$SnCl_4\cdot 5H_2O$	1/67–1/143	1/51–1/108	HTR (150 °C) and 48 h	^{29}Si MAS NMR and H_2-TPR	Characterisation of acid sites	225
Magadiite	$Na_2Si_{14}O_{29}$	Al^{3+}	0.039	AlOOH $Al_2(SO_4)_3$ $Al[OCH(CH_3)_2]_3$	1/15–1/40 1/15–1/40 1/15–1/40	1/13.9–1/42.5 1/22.4–1/64.2 1/11.8–1/32.8	HTR (150 °C) and 72 h	^{27}Al and ^{29}Si MAS NMR	Characterisation of acid sites	226
Magadiite	$Na_2Si_{14}O_{29}$	Al^{3+} Co^{3+}	0.039 —	$Al[OCH(CH_3)_2]_3$ $Co(NO_3)_2\cdot 6H_2O$	1/64	—	HTR (150 °C) and 72 h	^{29}Si MAS NMR and NH_3-TPD	Characterisation of acid sites Catalytic butyraldehyde conversion	227
Kenyaite	$Na_2Si_{20}O_{41}$	Er^{3+} Al^{3+} Co^{3+}	— 0.039 —	$Er(NO_3)_3\cdot 5H_2O$ $Al[OCH(CH_3)_2]_3$ $Co(NO_3)_2\cdot 6H_2O$	1/64	—	HTR (180 °C) and 96 h	^{29}Si MAS NMR and NH_3-TPD	Characterisation of acid sites Catalytic butyraldehyde conversion	227
Magadiite	$Na_2Si_{14}O_{29}$	Er^{3+} Al^{3+}	— 0.039	$Er(NO_3)_3\cdot 5H_2O$ $Al[OCH(CH_3)_2]_3$	1/15	1/9.25	HTR (150 °C) and 66 h	^{27}Al MAS NMR and NH_3-TPD	Characterisation of acid sites Catalytic ethanol conversion	228
Magadiite	$Na_2Si_{14}O_{29}$	V^{5+}	0.0355	$VOSO_4\cdot 4.2H_2O$	1/33	1/80.91	HTR (150 °C) and 66 h	UV-Vis absorption spectroscopy	Characterisation of acid sites Catalytic ethanol conversion	228
Magadiite	$Na_2Si_{14}O_{29}$	Al^{3+}	0.039	$Al[OCH(CH_3)_2]_3$	1/15	1/28.3–1/29.4	HTR (150 °C) and 66 h	^{27}Al and ^{29}Si MAS NMR and NH_3-TPD	Characterisation of acid sites Catalytic ethanol conversion	229
Magadiite	$Na_2Si_{14}O_{29}$	Al^{3+} and V^{5+}	0.039 and 0.0355	$Al[OCH(CH_3)_2]_3$ $VOSO_4\cdot 4.2H_2O$	1/15 1/33	1/42.0–1/54.7 1/71.1–1/86.4	HTR (150 °C) and 66 h	^{27}Al and ^{29}Si MAS NMR and NH_3-TPD	Characterisation of acid sites Catalytic ethanol conversion	229
Magadiite	$Na_2Si_{14}O_{29}$	Sn^{4+}	0.055	Na_2SnO_3, $SnCl_4\cdot 5H_2O$	1/67–1/333	—	HTR (150 °C) and 72 h	FT-IR and Raman and UV-Vis absorption spectroscopy	Characterisation of acid sites	230
Octosilicate	$Na_2Si_8O_{17}$	Al^{3+}	0.039	$Al[OCH(CH_3)_2]_3$	1/15–1/60	1/22–1/47	HTR (100 °C) and 336 h	^{27}Al and ^{29}Si MAS NMR	Characterisation of acid sites Catalytic ethanol conversion	231
Kanemite	$NaHSi_2O_5$	Al^{3+}	0.039	$Al(NO_3)_3\cdot 9H_2O$, $NaAlO_2$	1/2.5–1/100	1/7.2–1/188	SSR (700 °C) and 6 h	^{27}Al and ^{29}Si MAS NMR	Precursor for mesoporous silica	232
Kanemite	$NaHSi_2O_5$	Al^{3+}	0.039	$NaAlO_2$	1/20–1/100	1/20–1/100	SSR (700 °C)	^{27}Al MAS NMR	Precursor for mesoporous silica	233
Kanemite	$NaHSi_2O_5$	Ga^{3+}	0.047	GaOOH	1/100–1/200	—	SSR (700 °C)	^{71}Ga MAS NMR	Precursor for mesoporous silica	233

10538 | Chem. Soc. Rev., 2024, **53**, 10523–10574

This journal is © The Royal Society of Chemistry 2024

Table 4 (continued)

Layered silicate	Composition	HE	Effective ionic radii^a/nm	HE source	HE/Si atomic ratio (initial)	HE/Si atomic ratio (products)	Preparation^b	Characterisation	Objective	Ref.
Kanemite	$NaHSi_2O_5$	Al^{3+}	0.039	$NaAlO_2$	1/20–1/100	—	SSR (800 °C)	^{27}Al MAS NMR	Precursor for mesoporous silica	234
Kanemite	$NaHSi_2O_5$	Ti^{4+}	0.042	$Ti[O(CH_2)_3CH_3]_4$	1/100–1/500	1/96–1/435	SSR (675 °C) and 3 h	UV-Vis absorption spectroscopy	Precursor for mesoporous silica	235
Magadiite	$Na_2Si_{14}O_{29}$	Al^{3+}	0.039	Al_2O_3	1/18.5	—	HTR (130 °C) and 120 h	^{27}Al MAS NMR	Precursor for zeolite	236
Magadiite	$Na_2Si_{14}O_{29}$	Co^{2+}	0.058	$Co(CH_3COO)_2 \cdot 4H_2O$	1/50	—	HTR (150 °C) and 72 h	—	Precursor for zeolite Magnetism	237
Magadiite	$Na_2Si_{14}O_{29}$	Co^{2+}	0.058	$Co(CH_3COO)_2 \cdot 4H_2O$	1/50	—	HTR (150 °C) and 72 h	UV-Vis absorption and XPS spectroscopy	Precursor for zeolite Photocatalysts for water splitting	238
Octosilicate	$Na_2Si_8O_{17}$	Al^{3+}	0.039	$Al[OCH(CH_3)_2]_3$	1/15–1/60	1/22–1/42	HTR (100 °C) and 336 h	^{27}Al and ^{29}Si MAS NMR	Precursor for pillared materials	239
Kanemite	$NaHSi_2O_5$	Ga^{3+}	0.047	$Ga_2(SO_4)_3 \cdot 13H_2O$	1/18.5–1/37	1/19.4–1/31.5	SSR (700 °C) and 6 or 156 h	^{71}Ga and ^{29}Si MAS NMR	Fundamental study	240
Kenyaite	$Na_2Si_{20}O_{41}$	B^{3+}	0.011	B_2O_3	1/0.83	—	HTR (150 °C) and 168 h	^{11}B MAS NMR	Fundamental study	241
Magadiite	$Na_2Si_{14}O_{29}$	Al^{3+}	0.039	Al_2O_3	1/22.5–1/180	—	HTR (100–200 °C) and 30–259 h	^{27}Al MAS NMR	Fundamental study	242
Kenyaite	$Na_2Si_{20}O_{41}$	B^{3+}	0.011	B_2O_3	1/0.83–1/1.5	—	HTR (175 °C) and 48–168 h	^{11}B MAS NMR	Fundamental study	242
Magadiite Kenyaite	$Na_2Si_{14}O_{29}$ $Na_2Si_{20}O_{41}$	B^{3+}	0.011	B_2O_3	1/2.5	—	HTR (125/150 °C) and 552/72 h	^{11}B, ^{23}Na and ^{29}Si MAS NMR	Fundamental study	243
Magadiite	$Na_2Si_{14}O_{29}$	Al^{3+}	0.039	$Al[OCH(CH_3)_2]_3$	1/15	1/14.5	HTR (150 °C) and 12 h	^{27}Al and ^{29}Si MAS NMR	Fundamental study	244
Magadiite	$Na_2Si_{14}O_{29}$	Ti^{4+}	0.042	$TiCl_4$	1/50–1/200	—	HTR (150 °C) and 48 h	UV-Vis absorption and XAFS spectroscopy	Fundamental study	245
Octosilicate	$Na_2Si_8O_{17}$	Ti^{4+}	0.042	$TiCl_4$	1/50–1/200	1/54–1/204	HTR (100 °C) and 240 h	UV-Vis absorption and XAFS spectroscopy	Fundamental study	245
Octosilicate	$Na_2Si_8O_{17}$	Sn^{4+}	0.055	$SnCl_4 \cdot 5H_2O$	1/800–1/2000	1/893–1/3703	HTR (100 °C) and 504–672 h	FT-IR spectroscopy and H_2-TPR	Fundamental study	246
Magadiite	$Na_2Si_{14}O_{29}$	Al^{3+}	0.039	$Al[OCH(CH_3)_2]_3$	1/120–1/480	1/112–1/420	HTR (150 °C) and 72 h	^{27}Al MAS NMR	Adsorbent for Pb^{2+} and methylene blue	247
Octosilicate	$Na_2Si_8O_{17}$	Al^{3+}	0.039	Al_2O_3	1/40	1/22	HTR (105 °C) and 216 h	^{27}Al and ^{29}Si MAS NMR	Ion exchange with Cu^{2+}	248

^{a} The ionic radii of tetrahedrally coordinated heteroelements by the isomorphous substitution of Si^{4+} (0.026 nm) in layered alkali silicates, according to Shannon et al.[129] ^{b} The type of synthetic method and reaction time are indicated, where hydrothermal reaction and solid-state reaction are abbreviated as HTR and SSR, respectively. Value in () indicates reaction temperature.

This journal is © The Royal Society of Chemistry 2024

Chem. Soc. Rev., 2024, 53, 10523–10574 | 10539
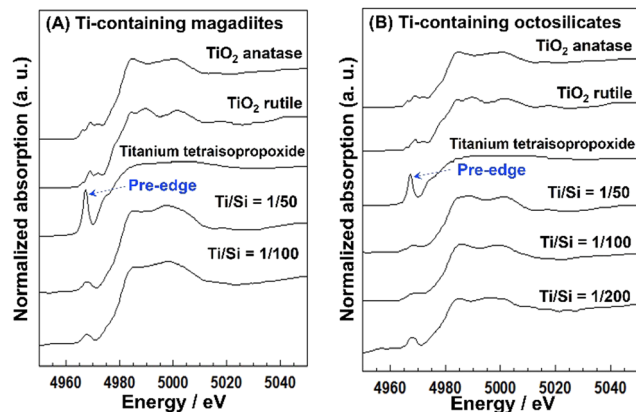
Fig. 9 (A) XANES spectra of the Ti-containing magadiites and reference. (B) XANES spectra of the Ti-containing octosilicates and ref. 245.

Fig. 10 XRD pattern and SEM image of the Ti-containing magadiites and octosilicates (Ti/Si = 1/10 and 1/20).[245]

Al/Si = 1/15–1/60), respectively.[224] The FT-IR spectra of Al-containing magadiite after the adsorption of CO at 100 K indicated the presence of Brønsted acidity, which was comparable with that of acidic zeolites (H-mordenite zeolite). As the Al content increased (Al/Si = 1/15–1/30), the population of acidic sites also increased. However, some of the Al was in octahedral coordination (probably extra framework aluminium oxide or (oxy)hydroxide), suggesting that the upper limit of the isomorphous substitution of Si with Al was lower than Al/Si = 1/30.

Ti-containing kanemite was synthesised from silicon tetraethoxide and titanium(IV) tetrabutoxide *via* the sol–gel process and subsequent crystallisation by calcination. It was possible to transform it into Ti-containing mesoporous silicas (designated as KSW-2).[235] The UV-Vis absorption spectra of the Ti-containing kanemite showed absorption bands at 210–220 nm when the Si/Ti ratio was larger than 300, indicating that the tetrahedrally coordinated titanium oxide species existed in the framework of kanemite. As the Ti content increased (Ti/Si = 1/100–1/200), the absorption band became broader because of the co-existence of octahedrally coordinated titanium oxide species. The upper limit of the incorporation of tetrahedrally coordinated Ti in the framework was as low as Ti/Si = 1/250. Recently, Ti-containing octosilicates and magadiites were synthesised *via* hydrothermal reactions using $TiCl_4$ as the Ti source in the starting mixture (silica gel and NaOH) for the preparation of magadiite and octosilicate.[245] The UV-Vis absorption and X-ray absorption near edge structure (XANES) spectra suggested that tetrahedrally coordinated titanium oxide species existed in the silicate frameworks. The XANES spectra of the Ti-containing silicates are shown in Fig. 9. In the Ti K-edge XANES spectra of the Ti-containing magadiites (Ti/Si = 1/100 and 1/50), a weak pre-edge peak was observed (Fig. 9A), indicating that the titanium oxide species existed mainly in tetrahedral coordination in the framework of magadiite. Alternatively, that of the Ti-containing octosilicate (Ti/Si = 1/200) showed a weak but single pre-edge peak (Fig. 9B), indicating that some of the titanium oxide species were in tetrahedral coordination in the framework of octosilicate. As the content of Ti increased (Ti/Si = 1/100 and 1/50), the XANES
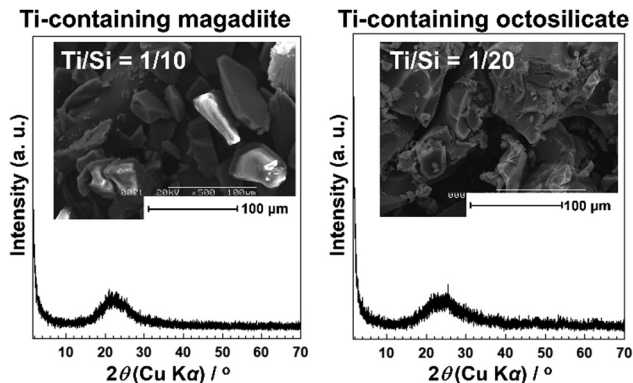
spectra of the Ti-containing octosilicates (Fig. 9B) were observed to be similar to that of rutile and anatase, indicating the presence of an isolated tetrahedrally coordinated titanium oxide species in the framework of octosilicate together with extra framework octahedrally coordinated titanium oxide species. These results suggested that the upper limit of the framework incorporation of Ti was Ti/Si = 1/50 and 1/100 for magadiite and octosilicate, respectively. In addition, as the Si/Ti ratio increased (Ti/Si = 1/10 and 1/20 for magadiite and octosilicate; Fig. 10), the XRD patterns of the products showed no crystalline phase and morphologies different from the Ti-containing silicates and aggregated TiO_2 particles were seen. The capacity of the incorporation of Ti into the silicate framework was higher for the silicates with thicker silicate layers (magadiite > octosilicate > kanemite, Table 3).[235,245] The amount of tetrahedrally coordinated titanium oxide species can be increased for kenyaite. To further understand the relationship between the incorporated amount of heteroelements in the silicate frameworks and emerging functions such as (photo)catalysis and adsorption, synthetic methods and the conditions need to be developed to prepare materials with a higher heteroelement content.

Layered silicic acid/alkali silicates have been used as precursors of zeolites and mesoporous silicas.[249,250] In particular, some zeolites are only obtained by topotactic conversion through the interlayer condensation of layered silicic acid/alkali silicates (Fig. 11).[251] The conversion of the Ti-containing layered silicic acid/alkali silicates into zeolites is worth investigating.

3.2. Variation in the heteroelements to be incorporated in the layered alkali silicates

The incorporation of other heteroelements besides Al^{3+} such as Co^{2+}/Co^{3+}, Er^{3+}, Ti^{4+}, Sn^{4+} and V^{5+} into the silicate framework has also been investigated given that these heteroelements are expected to play roles as isolated active sites for magnetic and catalytic properties.[225,227–230,235,237,238,245,246] The ionic radius of tetrahedrally coordinated heteroelements by the isomorphous substitution of Si^{4+} (0.026 nm) in layered alkali silicates and the experimental conditions of the examples are

10540 | *Chem. Soc. Rev.*, 2024, **53**, 10523–10574

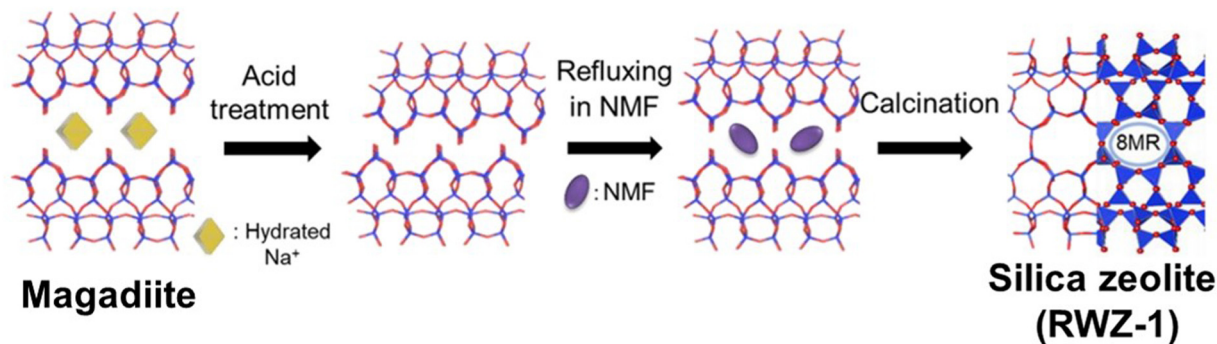This journal is © The Royal Society of Chemistry 2024

Fig. 11 Schematic of the topotactic conversion of magadiite into a silica zeolite (RWZ-1) during refluxing in *N*-methylformamide (NMF) and subsequent calcination. Reprinted from ref. 251 with permission from John Wiley & Sons.
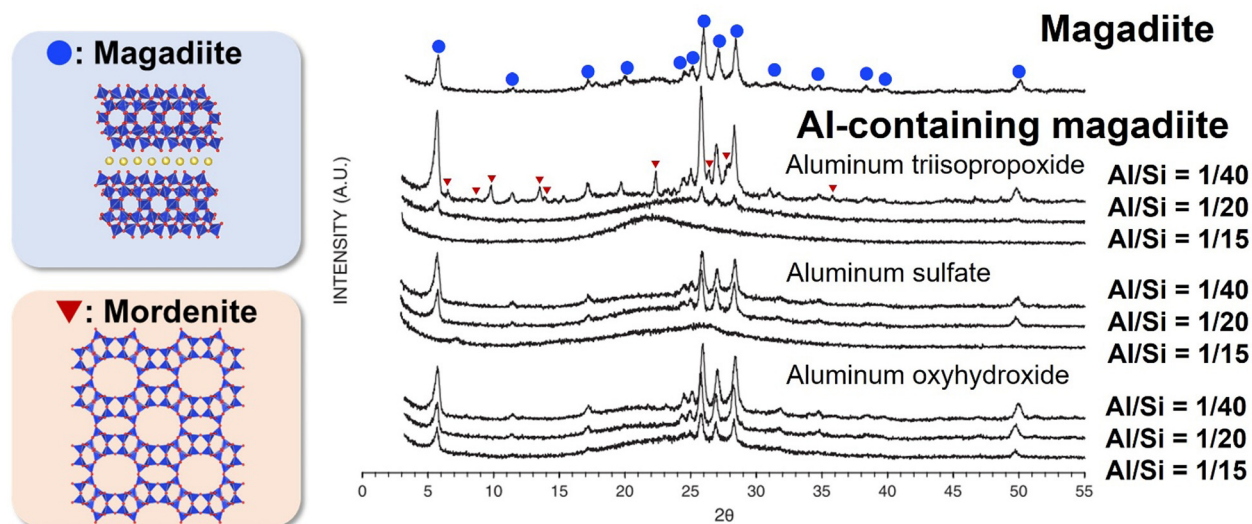

Fig. 12 XRD patterns of magadiite and Al-containing magadiites using aluminum triisopropoxide, aluminum sulfate and aluminum oxyhydroxide (Al/Si = 1/40, 1/20 and 1/15) as the aluminium source.[226]

summarised in Table 4.[129] The effective ionic radius is one of the important factors determining the isomorphous substitution. The isomorphous substitution with the elements such as Ni^{2+} (0.055 nm), Fe^{2+}/Fe^{3+} (0.063/0.049 nm), Cu^{2+} (0.057 nm) and Eu^{3+} (0.0947 nm) seems to be possible because of the size matching.

3.3. Synthesis of heteroelement-containing layered alkali silicates

Most of the heteroelement-containing layered alkali silicates have been prepared *via* the hydrothermal reaction of the starting material of layered alkali silicates in the presence of molecular species (alkoxides and metal salts) as the source of heteroelements. The amount of heteroelement incorporated in the framework of layered alkali silicates is as low as a few wt% (oxide base). The type of heteroelement source plays an important role in the incorporation. Al-containing magadiite was prepared with different types of Al sources (aluminium oxyhydroxide, aluminium triisopropoxide and aluminium sulfate), and

its acidic sites evaluated in the catalytic cracking of cumene.[226] The XRD patterns of Al-containing magadiite with different types of Al sources are shown in Fig. 12. Although aluminium oxyhydroxide led to the formation of crystallised Al-containing magadiite (Al/Si = 1/15–1/40), the formation of mordenite impurities was observed using aluminium triisopropoxide at Al/Si = 1/40. With a higher Al/Si = 1/15, the XRD patterns of the products using aluminium triisopropoxide and aluminium sulfate showed no crystalline phase, suggesting that the anions affected the crystallisation. Thus, the amount of heteroelement in the heteroelement-containing layered alkali silicates is limited (detail in Section 4).

3.4. Characterisation of the states of the incorporated heteroelements

The states of the heteroelements in silica/silicate frameworks can be evaluated various spectroscopic techniques, including NMR, UV-Vis absorption, photoluminescence and X-ray absorption (XANES and EXAFS) spectroscopy.

This journal is © The Royal Society of Chemistry 2024

Chem. Soc. Rev., 2024, **53**, 10523–10574 | **10541**
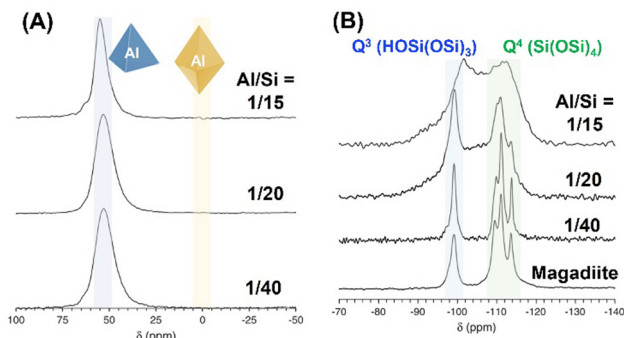
Fig. 13 (A) ^{27}Al and (B) ^{29}Si MAS NMR spectra of Al-containing magadiite using aluminum oxyhydroxide.[226]

To gain further insight into the chemical state of the heteroelements in the silica/silicate framework, solid-state magic angle spinning (MAS) NMR spectroscopy is a key technique. As a typical example, the ^{27}Al and ^{29}Si MAS NMR spectra of Al-containing magadiite using aluminium oxyhydroxide are shown in Fig. 13.[226] The coordination state of the Al sites in either tetrahedral or octahedral coordination is characterised by ^{27}Al MAS NMR measurement, showing signals at *ca.* 55 ppm or 0 ppm, respectively. These samples (Al/Si = 1/15–1/40) showed only a signal at around 55 ppm (Fig. 13A), corresponding to the tetrahedral coordination, indicating the isomorphous substitution of Si with Al. In the ^{29}Si MAS NMR spectrum of magadiite (pure silicate; Fig. 13B), four peaks were observed at *ca.* −100 ppm, which were attributed to Q^3 (HOSi(OSi)$_3$), and *ca.* −110, −112 and −114 ppm, corresponding to Q^4 (Si(OSi)$_4$). The ^{29}Si MAS NMR spectrum of Al-containing magadiite (Al/Si = 1/40) was similar to that of magadiite, whereas the spectrum became broader with an increase in the Al content (Al/Si = 1/20), with the appearance of a broad peak at −107 ppm which was attributed to amorphous silica. The incorporation of Al in the silicate framework affects the chemical environment of Si, *i.e.*, not only first coordination but also second or third coordination environment, resulting in low-field shifts (about 5 ppm: Q^4(1Al) *i.e.*, Si(OSi)$_3$(OAl)) and the broadening of the signal in the ^{29}Si MAS NMR spectrum.[265,266] As the content of Al increased (Al/Si = 1/15), two broad peaks were observed at −112 and −102 ppm, corresponding to Q^4(0Al) and Q^4(1Al)/Q^3(0Al), respectively, which suggested that most of this product existed as an amorphous phase.

The incorporation of Ti into various silicas/silicates has been examined for the design of (photo)catalysts. Titanium silicalite-1 (TS-1), which is a representative titanosilicate zeolite with isomorphous substitution of Si^{4+} with Ti^{4+} in the MFI zeolite framework, exhibited selective oxidation of various hydrocarbons with H$_2$O$_2$.[267,268] Regarding the states of the incorporated titanium oxide species in zeolites and mesoporous silica/silicate frameworks, UV-Vis absorption, photoluminescence and XAFS spectroscopy (Section 3.1) are powerful measurement tools to determine if the titanium oxide species exist as isolated tetrahedrally coordinated species in the silica/silicate framework.[235,245,269–273] Tetrahedrally coordinated

titanium oxide species in silicas/silicates showed absorption bands with the maximum at 220–280 nm due to the charge transfer excited state ([Ti^{4+}–O^{2-}] → [Ti^{3+}–O$^-$]*). In addition, these samples exhibited photoluminescence at around 450–550 nm upon excitation at 220–280 nm, which is ascribed to the charge transfer process.

3.5. Summary and perspectives

The incorporated heteroelements in layered silicates/silicic acids are exposed to the surface of silicate nanosheets, affecting their surface characteristics and associated functions, while their function has not been fully explored to date. Layered alkali silicates accommodate various guest species in their interlayer space for functional materials. Organic modification with cationic surfactants and silane coupling reagents has been done to design materials for applications in environment, energy and life science-related fields through molecular recognition.[43,249,260–264,274–284] Recently, the site-specific organic modification of octosilicate led to the fabrication of a floating adsorbent for the collection of metal ions from water.[283] Selective adsorption on layered alkali silicates (with defects in the silicate layer) and their silylated products has been reported.[256,285–287] These material designs will be examined using heteroelement-doped layered silicates.

Regarding synthetic aspects, the incorporation of heteroelements into the silicate frameworks is done during the preparation of layered silicates *via* the hydrothermal reaction, where phase separation of the heteroelements and the formation of different phases (such as zeolites) may occur depending on the composition. However, alternative synthesis methods are worth examining to extend the compositional variation. Heteroelement-containing silicate zeolites, such as zeolites with Ti^{4+}, Al^{3+} and Fe^{3+}, have been synthesised *via* mechanochemically assisted hydrothermal reactions using metal oxy(hydroxide) (*e.g.*, TiO$_2$ (anatase), γ-AlO(OH), α-Fe$_2$O$_3$, and α-FeOOH) and silica (fumed silica).[288–291] The synthesis of magadiite, octosilicate, and kanemite *via* the solid-state reaction at 50–900 °C has been reported.[292] In addition to the application of these reported procedures, the development of novel synthetic methods (including post-synthetic immobilisation[293,294]) is worth examining to extend the compositional variation.

4. 2 : 1 type phyllosilicates

Layered clay minerals, namely 2 : 1-type phyllosilicates (Fig. 14), are materials where isomorphous substitution plays a key role in their characters/functions. The useful adsorptive, ion exchange, swelling and catalytic functions of the clay minerals are known.[295,296] Silicate minerals of various structures and compositions are widely distributed in nature and clay minerals are known to be formed by the hydrothermal alteration or weathering of these silicate minerals. Metal (Mg^{2+} and Al^{3+}) hydroxide sheets are thought to play a role in directing the layered structure, given that layered silicic acids/silicates (given
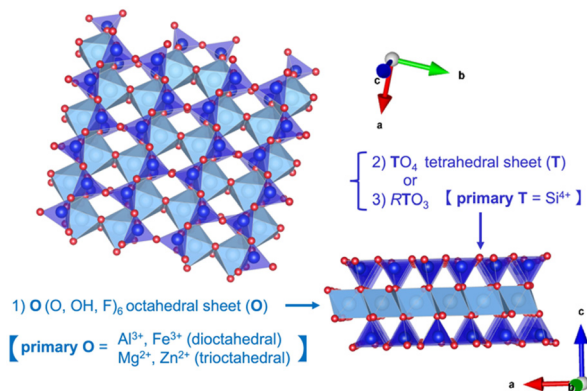
10542 | *Chem. Soc. Rev.*, 2024, **53**, 10523–10574

This journal is © The Royal Society of Chemistry 2024

Fig. 14 Structure of a 2:1-type phyllosilicate, two TO_4 (the primary element of **T** = Si^{4+}) tetrahedral sheets (T) on each side of an **O** (O, OH, F) octahedral sheet (O) occupied by octahedrally coordinated cations (*e.g.*, Mg^{2+}, Zn^{2+}/Al^{3+}, Fe^{3+}, *etc.*), forming a T–O–T layer (prepared using VESTA software).[44]

in Section 3) are less common from the aspects of mineral quantity in Earth's crust.

4.1. Structural versatility: combination of an LDH structure with SiO_4 tetrahedra and interlayer cations

The compositional variation of 2:1-type phyllosilicates by isomorphous substitution has led to versatile applications (Fig. 14). The layered clay minerals, which belong to the hydroxylated phyllosilicates, include T–O (1:1) and T–O–T (2:1) phyllosilicates.[3] Table 5 shows the classification of phyllosilicate clay minerals. They can be classified based on their sheet stacking (1:1 or 2:1), layer charge ($x + y$: or charge per unit cell of $Si_8O_{20}(OH)_4$), and type of interlayer into eight major groups. Further subdivision into sub-groups and species is made based on the type of octahedral sheet (dioctahedral and trioctahedral, which will be explained later), chemical composition and the geometry of the superposition of individual layers

and interlayers. The names used for groups, sub-groups, and mineral species are those approved by the AIPEA Nomenclature Committee or the IMA Commission on New Minerals and Mineral Names.

Isomorphous substitution of the main components in the silicate layer as Si^{4+} and/or $M^{2+/3+}$ with cations of similar size and lower valency gives a net negative charge. The quantity of the isomorphous substitution is expressed as x and y in the unit cell of $(Si, Al)_8O_{20}(OH)_4$ (*e.g.*, $[Si_{8-x}M^{tetra}{}_x]^{IV}$ $[Al_{4-y}M^{octa}{}_y]^{VI}O_{20}(OH)_4$, where M^{tetra} and M^{octa} are heteroelements in the SiO_4 tetrahedral sheet (T) and octahedral sheet (O), respectively. The compositional variation of 2:1-type phyllosilicates arises from three structural aspects, as follows: (1) Two types of octahedral sheets (O; dioctahedral and trioctahedral types composed of M^{3+} and M^{2+} hydroxides, respectively) are represented, as shown in Fig. 14, with a wide variety of octahedrally coordinated cations to replace M^{3+} and M^{2+}, which influence their functions similar to LDHs (the structures and functions were described in Section 2). (2) Substitution of Si^{4+} with M^{3+} in the tetrahedral sheet (T) affords acidic character, as observed in zeolites, mesoporous silicas and other silicas in addition to the generation of negative charge. (3) Covalent attachment of organic groups (R) with the silicon atom in the SiO_4 tetrahedra in T provides organically modified silicates with a type of self-assembled monolayer, which can form multilayers composed of alternatively stacked silicate layers and organic layers. When the silicate possesses a permanent net negative charge as a result of the isomorphous substitution, cations are interposed in the interlamellar region between the silicate layers. The amount and the location of the isomorphous substitution influence the surface characteristics, which are correlated with the colloidal, catalytic and adsorptive properties of the phyllosilicates. The charge per unit cell ($x + y$) is an important value in determining the characteristics of phyllosilicates. Among the phyllosilicates, smectites have been used most extensively in industrial applications as well as scientific

Table 5 Classification of phyllosilicate related to clay minerals adapted from Brindley and Brown[3]

Layer type	Group ($x + y$ = charge per unit cell[a])	Sub-group	Species[b]
1:1	Serpentine–kaolin ($x + y \sim 0$)	Serpentine	Chrysotile, antigorite, lizardite, amesite
		Kaoline	Kaolinite, dickite, nacrite
2:1	Talc–pyrophyllite ($x + y \sim 0$)	Talc	Talc, willemseite
		Pyrophyllite	Pyrophyllite
	Smectite ($x + y \sim 0.4$–1.2)	Saponite	Saponite, hectorite, sauconite
		Montmorillonite	Montmorillonite, beidellite, nontronite
	Vermiculite ($x + y \sim 1.2$–1.8)	Trioctahedral vermiculite	Trioctahedral vermiculite
		Dioctahedral vermiculite	Dioctahedral vermiculite
	Mica ($x + y \sim 2.0$)	Trioctahedral mica	Phlogopite, biotite, lepidolite
		Dioctahedral mica	Muscovite, paragonite
	Brittle mica ($x + y \sim 4.0$)	Trioctahedral brittle mica	Clintonite, anandite
		Dioctahedral brittle mica	Margarite
	Chlorite ($x + y$ variable)	Trioctahedral chlorite	Clinochlore, chamosite, nimite
		Dioctahedral chlorite	Donbassite
		Di, trioctahedral chlorite	Cookeite, sudoite
2:1 inverted ribbons	Sepiolite–palygorskite ($x + y$ variable)	Sepiolite	Sepiolite, loughlinite
		Palygorskite	Palygorskite

[a] $x + y$ refers to an $Si_8O_{20}(OH)_4$ unit cell for smectite, vermiculite, mica, and brittle mica. [b] Only few examples are given.

This journal is © The Royal Society of Chemistry 2024

Chem. Soc. Rev., 2024, **53**, 10523–10574 | **10543**

Table 6 Classification of dioctahedral $A^{n+}_{x/n}[T_8]^{IV}[O_4]^{VI}O_{20}(OH)_4$ and trioctahedral smectites $A^{n+}_{x/n}[T_8]^{IV}[O_6]^{VI}O_{20}(OH)_4$

Sub-group	Species	T		O		Chemical formula[a]
		Main	M^{tetra}	Main	M^{octa}	
Dioctahedral smectites	Montmorillonite	Si^{4+}	—	Al^{3+}	Mg^{2+}	$A^{n+}_{y/n}[Si_8]^{IV}[Al_{4-y}Mg_y]^{VI}O_{20}(OH)_4$
	Beidellite	Si^{4+}	Al^{3+}	Al^{3+}	—	$A^{n+}_{x/n}[Si_{8-x}Al_x]^{IV}[Al_4]^{VI}O_{20}(OH)_4$
	Nontronite	Si^{4+}	Al^{3+}	Fe^{3+}	—	$A^{n+}_{x/n}[Si_{8-x}Al_x]^{IV}[Fe_4]^{VI}O_{20}(OH)_4$
Trioctahedral smectites	(Fluoro)hectorite	Si^{4+}	—	Mg^{2+}	Li^+	$A^{n+}_{y/n}[Si_8]^{IV}[Mg_{6-y}Li_y]^{VI}O_{20}(OH, F)_4$
	Saponite	Si^{4+}	Al^{3+}	Mg^{2+}	—	$A^{n+}_{x/n}[Si_{8-x}Al_x]^{IV}[Mg_6]^{VI}O_{20}(OH)_4$
	Sauconite	Si^{4+}	Al^{3+}	Zn^{2+}	—	$A^{n+}_{x/n}[Si_{8-x}Al_x]^{IV}[Zn_6]^{VI}O_{20}(OH)_4$

[a] A^{n+}: exchangeable cation.

research. Smectite is the name of a group of swellable 2:1-type phyllosilicates $(0.4 \leq x + y \leq 1.2)$.[3,297] Depending on the composition and the location of the isomorphous substitution, smectite is classified as summarised in Table 6. The interlayer cations (*e.g.*, Na^+ and Ca^{2+}) are usually hydrated and are exchangeable.

Swelling occurs when the hydration energy overcomes the attractive forces between the silicate layers and is sufficient to cause osmotic swelling in excess water.[298] The spontaneous swelling of smectites in water leads to the formation of a stable thixotropic gel or suspension.[45,46,298,299] Smectites occasionally form liquid crystalline phase phyllosilicates under specific conditions with careful preparation.[300–302] Structural colour emerged when nanosheets were stacked with submicrometer periodicity in an aqueous suspension (Fig. 15).[302] Gravity and an electric field led to different alignments of the nanosheets in poly(*N*-isopropylacrylamide) composite gel films. The combined two-layer gels exhibited three-dimensional deformations
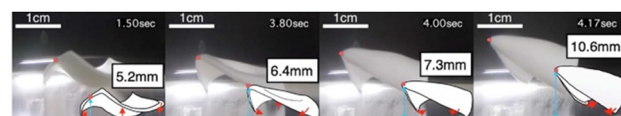
Fig. 16 Jumping motion of poly(*N*-isopropylacrylamide) composite gel films in water in response to thermal stimulus. Photographs and corresponding illustrations show the time course of the gel films after immersion in hot water. The heights from the ground surface to the red point on the gel are also shown. The red arrows indicate the direction of movement of each part. Reprinted with permission from ref. 303. Copyright 2022, the American Chemical Society.

(*e.g.*, jumping motion), which were triggered by temperature changes with controlled curvature (Fig. 16).[303]

When the solvents in the suspension are evaporated on a flat plate, plate particles pile up with their *ab* plane parallel to the substrate to form an oriented film.[304,305] A similar procedure in the presence of a water-soluble polymer afforded multi-functionalised inorganic–organic hybrid films with transparent gas barrier,[306] thermal stability, water resistance, water-induced self-healing behaviour, and adhesion.[307] The Langmuir–Blodgett[308] and layer-by-layer deposition techniques (alternating adsorption of a cation and an anionic silicate layer) from exfoliated platelets were used to obtain inorganic–organic multilayer thin films.[309–311]

In addition to the swelling property and the associated film-forming ability from a colloidal suspension, isomorphous substitution is the origin of cation exchange ability and acidic character. The cation exchange capability was used to modify the properties of smectites for application as fillers in clay-polymer hybrids,[312–317] rheology-controlling reagents,[318,319] reaction media to control photochemical reactions,[320–323] optics,[324] selective adsorption,[325–327] chiral discrimination,[328,329] and catalysis.[330]

4.2. Bentonite and purified bentonite

Bentonite (coarse samples, a natural resource containing smectites as the main component) contains accessory minerals such as crystalline SiO_2 (*e.g.*, quartz, cristobalite), amorphous SiO_2, feldspar, and goethite $FeO(OH)$, as presented in Table 7.[331,332] Depending on the application, purified bentonites, which are commercially available, are used.
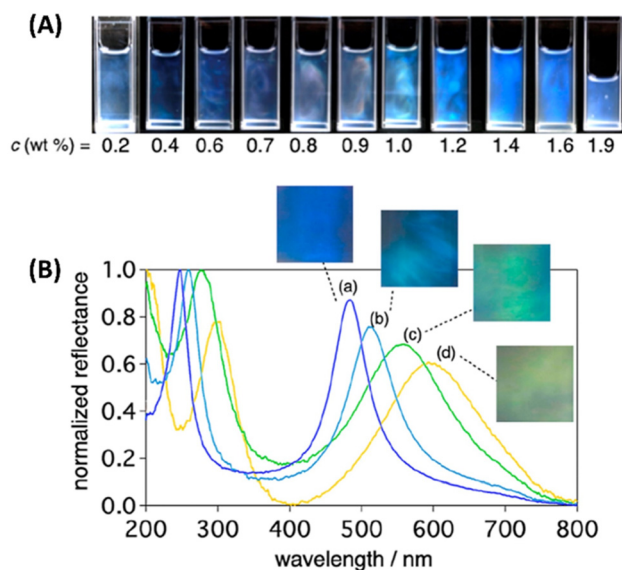

Fig. 15 (A) Photographs of nanosheet colloids (average nanosheet diameter of 1.8 μm) with various nanosheet concentrations *c*. (B) Photographs and UV-Vis spectra of the nanosheet colloid with the average nanosheet diameter of (a) 0.14, (b) 0.16 (c) 0.98, and (d) 1.8 μm. The spectra were recorded at an observing angle of 10°.[302]

10544 | *Chem. Soc. Rev.*, 2024, **53**, 10523–10574

This journal is © The Royal Society of Chemistry 2024

Table 7 Composition of some reference clay minerals in the structural formula of $[T_8]^{IV}[O_4/O_6]^{VI}O_{20}(OH)_4$

		T		O		
		Si	Al^{tetra}	Al^{octa}	Fe	Mg
SAz-1$^{a\,331}$		8.00	0.00	2.67	0.15	1.20
ST$^{b\,331}$		7.22	0.78	1.96	1.60	0.58
SWa-1$^{c\,331}$		7.33	0.67	0.91	2.86	0.28
JP$^{d\,331}$		7.71	0.29	3.00	0.38	0.63
JCSS3101 $^{e\,332}$	NIMS^g	7.66	3.37 (Al$^{tetra+octa}$)		0.21	0.64
	NMNS^h	7.56	3.47 (Al$^{tetra+octa}$)		0.25	0.69
JCSS3501 $^{f\,332}$	NIMS	7.19	0.81 (Al$^{tetra+octa}$)		0.00	5.99
	NMNS	7.02	0.71 (Al$^{tetra+octa}$)		0.00	6.26

^{a} SAz-1: (Cheto, AZ), a magnesium rich montmorillonite. ^{b} ST (Stebno): an iron-rich beidellite from the Czech Republic, which contains about 21% of total iron bound in goethite. ^{c} SWa-1: a ferruginous smectite from The Clay Mineral Repository of the Clay Minerals Society. ^{d} JP: hydrothermal, aluminium-rich montmorillonite from the Kremnica mountains in central Slovakia. ^{e} JCSS3101: montmorillonite, a reference clay sample of the Clay Science Society of Japan. ^{f} JCSS3501: a synthetic saponite, a reference clay sample of the Clay Science Society of Japan. ^{g} NIMS: analysed by the National Institute for Materials Science, Japan. ^{h} NMNS: analysed by the National Museum of Nature and Science, Japan.

Purification is possible by the following dispersion-sedimentation method. Coarse samples were suspended in deionised water, treated several times with 1.0 M aqueous $CaCl_2$, washed until free of chloride, and centrifuged. After the nominally <2 μm sample was collected, drying at 60 °C and subsequent grounding to <0.2 mm were performed.[331] As a dissolution method, the alkaline fusion technique was employed, melting the sample with BO_3 and Li_2CO_3, followed by dissolution in acidic HCl solution.[332] The purification was confirmed by XRF and ICP.

Bentonite, purified bentonites (non-swelling impurities were removed from bentonite by dispersion-sedimentation method), and synthetic smectites are commercially available and some of them are authorised by academic societies (The Clay Minerals Society[333] and The Clay Science Society of Japan[334]). However, their quantitative characterisation is difficult because of the fine grain-size of clay minerals and the association with accessory minerals. The compositional variation is seen even for samples from the same deposits.[335] The Clay Science Society of Japan authorizes reference clay samples with their chemical formula/compositions.[332] Some additional data are available, as shown in Table 7. JCSS3101 includes only a small amount of quartz as a result of careful purification. The associated minerals make it difficult to determine the accurate compositions of the smectite phase by bulk analysis. The location of isomorphous substitution is another difficulty given that the quantity is normally low and clay minerals are commonly poorly crystalline.

4.3. Site of isomorphous substitution in 2 : 1-type phyllosilicates, heteroelements and their amount

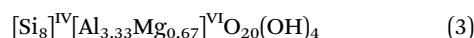Available range of Al/Si ratio in T–O–T (2 : 1)-type phyllosilicate is discussed employing the "pyrophyllite" structure as the original structure, as represented by the following formula (eqn (1)).

$$[Si_8]^{IV}[Al_4]^{VI}O_{20}(OH)_4 \qquad (1)$$
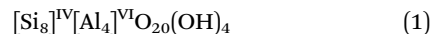
According to the Loewenstein rule,[336] which applies the avoidance of the Al–O–Al bond in T, the maximum Si^{4+} can be substituted with Al^{3+} at the Al/Si atomic ratio of 1/3 in the tetrahedral sheet (Al/Si = 1/1 in total, eqn (2), the charge compensated cations are omitted hereafter), forming paragonite-type mica ($x + y = 2$, Table 5).

$$[Si_6Al_2]^{IV}[Al_4]^{VI}O_{20}(OH)_4 \qquad (2)$$
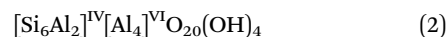
Ross and Hendricks[337] published a series of 100 analyses of smectites, from which they worked out their structural formula. As a result, two equations (eqn (3) and (4)) were given as typical substitutions in O and T, respectively, which are intermediate values in the common range of $x + y$ (0.4–1.2) in smectites.

$$[Si_8]^{IV}[Al_{3.33}Mg_{0.67}]^{VI}O_{20}(OH)_4 \qquad (3)$$

$$[Si_{7.33}Al_{0.67}]^{IV}[Mg_6]^{VI}O_{20}(OH)_4 \qquad (4)$$
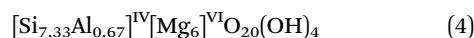
Compared with other 2 : 1-type phyllosilicates, smectites have high interlayer accessibility for various inorganic and organic species. The cation exchange capacity (CEC) of smectites, which is directly correlated with the amount of isomorphous substitution, is usually expressed in the unit of milliequivalent (meq) of exchangeable cations per 100 g of smectite (clay). The CECs of smectites are empirical values ranging from 60 to 120 meq/100 g of clay. Several techniques have been used for determining the CEC using ammonium acetate,[338] triethanolamine buffered barium chloride,[339–341] calcium chloride,[342] methylene blue,[343,344] silver thiourea,[345] and copper(II) ethylenediamine.[346] It should be noted that some organic and organometallic cations may be adsorbed over the CEC by van der Waals interactions (intersalation).[347,348] The CECs of smectites are governed by permanent charge and independent of the ionic strength electrolyte concentration and pH.

Smectites and vermiculites are distinguished at the layer charge of $x + y = 1.2$ per unit cell.[3] The identification is commonly made by swelling in water and in glycerol; when saturated with Mg^{2+} ions, the basal spacing of vermiculite expands to approximately 1.5 nm in water and glycerol, whereas smectites expand to 1.7–1.8 nm in glycerol. The synthesis of smectites with an extremely large layer charge (e.g., $x + y = 2.66$) resulted in the formation of a non-expandable phase even in the presence of Na^+ ions.[349] The question arises if any division can be made between smectites ($x + y = 0.4–1.2$) with high layer charge and vermiculite ($x + y = 1.2–1.8$) with a low layer charge? Méring and Perdo[350] suggested that the order or disorder of the isomorphous substitutions may be another feature of these minerals.

Here, the amount of isomorphous substitution ($x + y$ value or CEC) will be discussed for both sites (T and O) in 2 : 1-type phyllosilicate $[T_8]^{IV}[O_4]^{VI}O_{20}(OH)_4$ and $[T_8]^{IV}[O_6]^{VI}O_{20}(OH)_4$, where the isomorphous substitution occurs as

This journal is © The Royal Society of Chemistry 2024

Chem. Soc. Rev., 2024, **53**, 10523–10574 | **10545**

Table 8 Isomorphous substitution of selected 2:1-type phyllosilicates and synthesis conditions

Formula of anionic form	M^{tetra}	M^{octa}	Concentration x', y' (nominal) / x, y (found)	Method^a	Temp. (°C)	Specific characterisation	Objective	Ref.
$[Si_{8-x}M^{tetra}_x[Al_{4-y}M^{octa}_y]^{VI}O_{20}(OH)_4]$	Al^{3+}	(y = 0)	$0.34 \leq x \leq 1.34$ / $x = 0.66$	HTR	300		Thermodynamics of the formation	349
		(y = 0)		HTR	260–430		Thermodynamics of the formation	349
		(y' = 0)	$0.80 \leq x' \leq 1.56$	HTR	220		Thermodynamics of the formation	351
		Fe^{3+}	$x = 1.15, y = 1.53$	RE	95		Thermodynamics of the formation	438
$[Si_{8-x}M^{tetra}_x[Mg_{6-y}M^{octa}_y]^{VI}O_{20}(OH)_4]$	Al^{3+}	Al^{3+}	$\{ 0.33 \leq x \leq 1.61;\ 0 \leq y \leq 0.05 \}$	HTR	300	UV-Vis, ^{27}Al-NMR	Dye organisation	353
		Fe^{3+}	$\{ x' = 2;\ y' = 1 \}$	HTR	100–250	IR, XRD(060)	Fundamental study	354
		(y = 0)	$0.34 \leq x \leq 2.68$	HTR	260–450	^{27}Al, ^{29}Si-NMR, Al-EXAFS	Thermodynamics of the formation	349
		(y = 0)	$x = 0.66$	HTR	550		Thermodynamics of the formation	355
		(y = 0)	$x \leq 1.88$	HTR	400		Thermodynamics of the formation	356
		(y' = 0)	$0.2 \leq x' \leq 1.2$	RE	90		Solid-acid catalysis	357 and 358
$[Si_{8-x}M^{tetra}_x[Co_6]^{VI}O_{20}(OH)_4]$	Al^{3+}	—	$0.2 < x' < 0.9$	RE	90	^{27}Al, ^{29}Si-NMR,	Solid-acid catalysis	359
$[Si_{8-x}M^{tetra}_x[Zn_6]^{VI}O_{20}(OH)_4]$		—	$0.2 \leq x' \leq 2.4$	RE	90	Al-EXAFS	Solid-acid catalysis	359
$[Si_{8-x}M^{tetra}_x[(Ni, Co)_6]^{VI}O_{20}(OH)_4]$		—	$x' = 2$	HTR	100–250	IR, XRD(060)	Fundamental study	354
$[Si_8]^{IV}[Al_{4-y}M^{octa}_y]^{VI}O_{20}(OH,F)_4]$		Mg^{2+}	$0.40 \leq y' \leq 0.80$	HTR	220	^{19}F-NMR	Fundamental study	413
		Zn^{2+}	$y' = 0.4, 0.8$	HTR	220	^{19}F-NMR, Zn-EXAFS	Fundamental study	360
$[Si_8]^{IV}[Fe^{3+}_{4-y}M^{octa}_y]^{VI}O_{20}(OH)_4]$		Mg^{2+}	$0.1 \leq y \leq 2$	HTR	200	XRD(060)	Fundamental study	410
$[Si_8]^{IV}[Mg_{6-y}M^{octa}_y]^{VI}O_{20}(OH)_4]$		Fe^{3+}	$0.6 \leq y \leq 2$	HTR	200	XRD(060)	Fundamental study	410
$[Si_8]^{IV}[Mg_{6-y}M^{octa}_y]^{VI}O_{20}(OH, F)_4]$		Li^+	$y' = 0.57$	RE	—	SAXS	Fundamental study	426
		Li^+	$0.07 \leq y' \leq 1.4$	RE	—	XRD(001)	Varying layer charge for adsorbent design	430,431
		Li^+	b	SSR	1650	XRD (single-crystal refinement)	Homogeneous layer charge for homogeneous pore and nanocomposite	460
$[Si_8]^{IV}[Ni_{6-y}M^{octa}_y]^{VI}O_{20}(OH, F)_4]$		Ni^{2+}	$y' = 0.6$	HTR	200		Precursor of catalyst	361
$[Si_8]^{IV}[Mn_{6-y}M^{octa}_y]^{VI}O_{20}(OH, F)_4]$		Li^+	$y' = 0.8$	HTR	150		Fundamental study	411
$[Si_8]^{IV}[Zn_{6-y}M^{octa}_y]^{VI}O_{20}(OH, F)_4]$		Li^+	$y' = 0.8$	HTR	150		Fundamental study	383

^{a} RE: reflux, HTR: hydrothermal reactions, SSR: solid-state reactions. ^{b} The chemical formula of $Na_{0.05}Mg_{6.52}Li_{1.12}Si_{7.93}O_{21.91}F_{2.09}$.

10546 | *Chem. Soc. Rev.*, 2024, **53**, 10523–10574

This journal is © The Royal Society of Chemistry 2024

$[Si_{8-x}M^{tetra}{}_x]^{IV}[Al_{4-y}M^{octa}{}_y]^{VI}O_{20}(OH)_4$ and $[Si_{8-x}M^{tetra}{}_x]$-$^{IV}[Mg_{6-y}M^{octa}{}_y]^{VI}O_{20}(OH)_4$, respectively (Table 8).

4.4. Roles of isomorphous substitution in the functions of smectites

4.4.1. Heteroelements in T. The most common M^{tetra} is Al^{3+}, whereas several types of M^{octa} are incorporated in the octahedral sheet (O) (Table 8). When the Al/Si ratio is higher than that in the "pyrophyllite" structure $[Si_8]^{IV}[Al_4]^{VI}O_{20}(OH)_4$ (eqn (1)) in the range of x less than 1.56 (Table 8),[349,351,368,369] the host formula (the charge compensating cation is omitted) is expressed as $[Si_{8-x}Al_x]^{IV}[Al_4]^{VI}O_{20}(OH)_4$ ("dioctahedral smectites").

The phase diagram of smectites was summarised by Kloprogge *et al.*[370] The dioctahedral smectite was obtained as single phase at $0.34 \leq x \leq 1.34$ when the synthesis conditions were 300 °C and 100 MPa (Table 8).[349] Single-phase smectite with the x of 0.66 was exemplified at the temperature range 260–430 °C (Table 8).[349] Instead of Al^{3+} in O, three Mg^{2+} ions are incorporated in O in half of the unit cell with the Si^{4+}–Al^{3+} substitution in T ("trioctahedral smectites"), where the formula is expressed as $[Si_{8-x}Al_x]^{IV}[Mg_6]^{VI}O_{20}(OH)_4$. When x was 0.66, a single phase was achieved in the temperature range of 260–450 °C. In the case of $0.34 \leq x \leq 1.34$, 550 °C was required to obtain a single phase (Table 8).[355] A high concentration of Al^{3+} in the initial mixture and high temperature were preferred for the Si^{4+}–Al^{3+} substitution in T (100 MPa).[369]

The Si^{4+}–Al^{3+} substitution in T was discussed for trioctahedral smectites using a reference clay (JCSS3501, synthetic saponite) for application in solid-acid catalysis[371] and dye immobilisation.[372–374] The synthesis and characteristics of saponite (one of trioctahedral smectites) were summarised in a recent review.[375] The maximum x value was 1.88 (Table 8), when the preparation was conducted at 450 °C and at $x' = 2.0$ (x' corresponds to x in the initial mixture for the preparation).[356] When the preparation was conducted at 300 °C and 8.5 MPa for 6 h, x in $[Si_{8-x}Al_x]^{IV}[Mg_{6-y}Al_y]^{VI}O_{20}(OH)_4$ was in the range of 0.33 to 1.61 (Table 9). A small amount of Al^{3+} was substituted in O.[353] It was confirmed experimentally that the CEC varied depending on x. Cationic porphyrins were immobilised without aggregation as a result of matching the distances of the positive charge of the porphyrins with that of the negative charge on the silica layer, giving highly emissive materials (dye aggregation

Table 9 Chemical compositions determined using XRF for trioctahedral smectites with varying x and y values[353]

$\{[Si_{8-x}Al_x]^{IV}[Mg_{6-y}Al_y]^{VI}O_{20}(OH)_4\}^{-(x-y)}$			CEC/meq $(100\ g)^{-1}$	Inter-charge distance/nm
x	y	$x-y$		
1.61	0.05	1.56	195	0.83
1.32	0	1.32	168	0.92
1.11	0	1.11	142	1.00
1.03	0	1.03	132	1.04
0.79	0.01	0.78	100	1.19
0.56	0.03	0.53	69	1.45
0.45	0	0.45	59	1.57
0.33	0.03	0.30	39	1.92
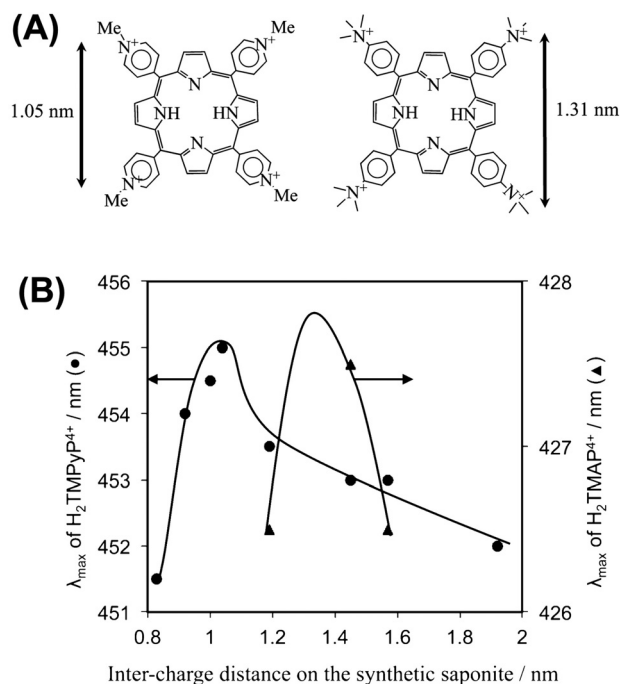
Fig. 17 (A) Structures of cationic porphyrins H_2TMPyP^{4+} and H_2TMAP^{4+}, where the distances between quaternary ammonium (arrow) are 1.05 and 1.31 nm, respectively and (B) relationship between the inter-charge distance on the trioctahedral smectites shown in Table 8 and the position of the absorption maximum for ● H_2TMPyP^{4+} and ▲ H_2TMAP^{4+} on the smectites. Reprinted with permission from ref. 353. Copyright 2011, the American Chemical Society.

usually deactivates the excited state *via* energy transfer between the dyes: Fig. 17).

Solid-acid catalysts were obtained by Si^{4+}–Al^{3+} substitution in T.[331,371,376] Acid-treatment activated smectites to be Brønsted acids because the protons in the Si^{4+}–O–Al^{3+}-OH bonds participated as Brønsted acidic sites, as seen in aluminosilicate zeolites. Pyridine has been employed as a probe for evaluating the acidic sites (IR and temperature-programmed desorption (TPD) are used to distinguish physisorption and chemisorption at Brønsted and Lewis acid sites, and by hydrogen bonding). The desorption behaviour of pyridine depended on the particle size (60% of montmorillonite JCSS3101 particles are >0.2 μm, whereas 90% of synthetic smectite JCSS3501 was <0.2 μm).[371] The acid-treatment of smectites with high magnesium contents (trioctahedral smectites, O = Mg^{2+}) more readily leached Mg^{2+} than that containing a higher proportion of Al^{3+} as M^{octa}, giving more acidic sites. This difference was explained by the difference in the bond energy of Mg–O (362 kJ mol^{-1}) from that of Al–O (511 kJ mol^{-1}). Some of the cations leached from O to migrate into the interlayer space as exchangeable cations, which also participated as catalytically active species.

4.4.2. Heteroelements in O. In addition to the substitution in T, that in O is also seen. A typical main component in O is Mg^{2+}, *i.e.*, $[Si_8]^{IV}[Al_{4-y}Mg_y]^{VI}O_{20}(OH)_4$ and $[Si_8]^{IV}[Mg_{6-y}M^{octa}{}_y]^{VI}O_{20}(OH)_4$ (Table 8). An important mineralogical problem is the extent of the substitutions in O between heterovalent cations (possible existence of "intermediate" di-tri-octahedral smectites).

This journal is © The Royal Society of Chemistry 2024

Chem. Soc. Rev., 2024, **53**, 10523–10574 | **10547**

Fig. 18 Octahedral layer of $Na_{0.8}[Si_8]^{IV}[Al_{3.2}Mg_{0.8}]^{VI}O_{20}(OH)_4$ viewed normal to the surface. The average distribution of Mg defects (highlighted) is shown. Four types of "defect" distribution: (1) a total of 35% of the Al atoms is surrounded by three Al atoms and no Mg; (2) 55% of the Al atoms is surrounded by two Al atoms and one Mg atom; (3) 10% of the Al atoms is surrounded by one Al atom and two Mg atoms; and (4) none of the Al atoms are surrounded by three Mg neighbours. Reprinted with permission from ref. 377. Copyright 2005, the American Chemical Society.

Decarreau *et al.* synthesised smectites with Al^{3+} and Mg^{2+} as octahedral cations *via* hydrothermal reactions at 200 °C and equilibrium pressure (almost 16 bars) for 15 to 30 days.[354] They concluded that the segregation of Al^{3+} and Mg^{2+} in O was common and led either to clusters within O or to the phase separation of two different phases. In contrast, in a molecular dynamic simulation, average distribution of the isomorphous substitution was employed in the structural unit.[377,378] A "defect (coordinated with Mg^{2+} in the defect)" distribution in a montmorillonite model with the average CEC = 108 meq/100 g, y = 0.8, $Na_{0.8}[Si_8]^{IV}[Al_{3.2}Mg_{0.8}]^{VI}O_{20}(OH)_4$, was adapted, as shown in Fig. 18. Several defect distributions were possible depending on the size of the model cell. They all contained domains with a density of three defects per square nanometer to the density of one defect per square nanometer.[377] The layer charges were directed as $x + y$ = 0.50, 0.62, 0.76, and 0.88 per unit cell, which were in the typical charge range of smectite[378] to understand "how does the layer charge influence the attractive force of the adsorbed water molecules with the silicate layer?"

Both Lewis (octahedral) and Brønsted (tetrahedral or interlayer cations) acidic sites have been investigated for application as solid-acid catalysts.[330,379,380] Bifunctional catalysts were designed when basic nanoparticles (*e.g.*, Pt) were deposited.[381] The Lewis acidic sites emerged from Zn^{2+} in O were effective in a catalytic reaction (Friedel–Crafts alkylation of benzene) with

the aid of the Brønsted acidic sites, which were derived from the $Si^{4+}–Al^{3+}$ substitution in T. The molar Al/Si ratio was varied in $[Si_{8-x}Al_x]^{IV}[O_6]^{VI}O_{20}(OH)_4$ as $0.2 \leq x' \leq 1.2$ (O = Mg^{2+}), $0.2 \leq x' \leq 2.4$ (O = Zn^{2+}), and $0.2 \leq x' \leq 0.9$ (O = Co^{2+}) (Table 8)[357,358] to examine the catalytic activity in *n*-alkane cracking above 200 °C in an inert atmosphere.[359] The interlayer cation was exchanged with Al^{3+} to enhance the acidic properties. However, the reduction of Ni^{2+} in O by hydrogen resulted in the formation of metallic Ni particles, causing deactivation by coke formation. The substitution of Ni^{2+} with Co^{2+} in O suppressed the coke formation.[382]

Transition metal ions such as Ni^{2+}, Co^{2+}, Mn^{2+}, Fe^{3+}, and Zn^{2+} have been incorporated in O (Table 8).[383,384] Hydrothermal reactions led the incorporation of Zn^{2+} in O as compared to Cu^{2+}, Co^{2+} or Ni^{2+}.[358] Ti^{4+} was incorporated as octahedrally coordinated species, when Zn^{2+} was incorporated in O of a (fluoro)smectite.[385]

The incorporation of iron with varying oxidation states has been studied. Iron in O has been recognised as an electron donor/acceptor[386–392] and energy acceptor to deactivate the excited state of the adsorbed luminophores.[393–396] The luminescence quenching is not favoured for designing photoluminescent materials, and thus synthetic 2:1-type phyllosilicates have been used. Alternatively, the quenching of the excited state by iron was used to stabilise dyes upon photoirradiation.[396] When rhodamine 6G was adsorbed on 2:1-type phyllosilicates with varying iron contents, the dye stabilities were proportional to the quenching efficiency, which was correlated with the iron content (Fig. 19). This is an important phenomenon given that dye stability is required for the development of dye-clay pigments.[397] Along this line, a bentonite with a low iron content was reported recently.[398] The mechanical properties of a biopolymer hydrogel were improved using the bentonite, where synthetic hectorites did not have positive effects. Due to the low iron content, the photoluminescence from the adsorbed cyanine dyes on the clay in the hydrogel was seen and a unique photoluminescence mechanochromism was reported.[373,399]

A bentonite with high iron content was also found and the state of the iron was extensively characterised to be octahedrally coordinated Fe^{2+} probably in T. The bentonite was shown to be a photocatalyst for H_2 evolution from aqueous methanol (Fig. 20).[386] The layer charge varied in response to the content of Fe^{3+} and Fe^{2+}, affecting the hydration of the interlayer cations and swelling pressure.[400–402] Iron-containing smectites have been synthesised,[403–408] where a reducing agent (hydrazine or sodium dithionite) was required to obtain Fe^{2+}-rich (ferruginous) smectites. Ferruginous smectites (nontronite) included iron as $Fe^{2+}_{2.8}(Si, Al)_8O_{20}$ for the SWa-1 sample (Grant County, Washington, USA, Clay Mineral Society),[367] and $Fe^{2+}_{3.6}(Si, Al)_8O_{20}$ for Garfield nontronite (Spokane, Washington, USA, API-no. 33-A).[409] The syntheses were performed at 90 °C for 2–3 weeks, and the amounts of Fe were $Fe^{2+}_{2.8}(Si, Al)_8O_{20}$[408] and $Fe^{2+}_{1.5}(Si, Al)_8O_{20}$.[362] According to the IR absorption band due to the $Fe^{3+}–Al–OH$ bonds, Al^{3+} and Fe^{3+} were miscible (not Fe^{2+} because the ionic radius of Fe^{2+} was too

10548 | *Chem. Soc. Rev.*, 2024, **53**, 10523–10574

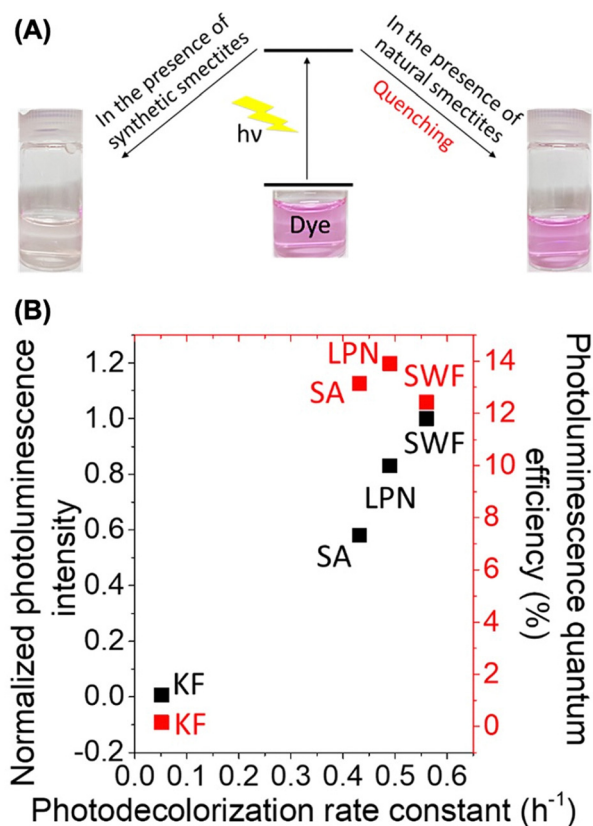This journal is © The Royal Society of Chemistry 2024

Fig. 19 (A) Photograph of an organic luminophore (Rhodamine 6G) and (B) relationship of the photodecolorisation rate constant with the normalised photoluminescence intensity (black) and the photoluminescence quantum efficiency (red) of SWF-R6G, SA-R6G, LPN-R6G, and KF-R6G suspensions.[396]
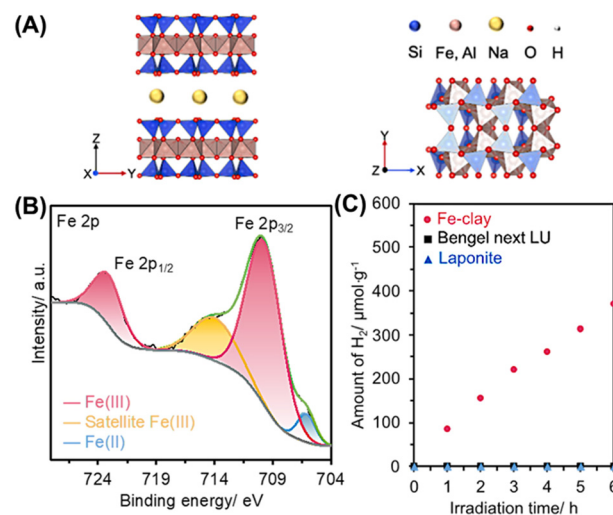

Fig. 20 (A) Polyhedral model of the smectite structure from the [100] direction and [001] direction, (B) Fe 2p XPS spectrum of Fe-clay, and (C) photocatalytic H_2 evolution of Fe-clay (red circle), Bengel next LU (black square), and LAPONITE® (blue triangle) from aqueous MeOH.[386]

large to be miscible with Al^{3+}) in O.[362] Mg^{2+} and Fe^{3+} were miscible in O (Table 8).[354,410] The incorporation of Mn in O of smectite has scarcely been reported, which is probably because of the difficulty in controlling the oxidation state of Mn.[411]

4.4.3. Vacancy in O. Lattice defects/vacancies in the octahedral sheets also generate a negative charge. The solution pH played an important role in crystallising $[Si_8]^{IV}[Mg_{6-y}]^{VI}$-$O_{20}(OH)_4$.[412] Tosca and Masterson investigated the influence of pH on silica oligomerisation for T and precipitation of $Mg(OH)_2$ at 25 °C.[412] Vacancies in O arose if the velocity for T was higher than that for O. At a relatively high pH, a greater number of octahedral vacancies was generated as the velocity of silica oligomerisation was higher than that for $Mg(OH)_2$ precipitation.

Torii et al.[361] prepared $[Si_8]^{IV}[Ni_{6-y}]^{VI}O_{20}(OH, F)_4$ in the presence of HF at an atomic F/Si ratio in the range of 0 to 1/2 in the initial compositions. When the HF amount was larger, a smaller amount of vacancy was shown by the methylene blue adsorption. Replacing OH with F resulted in lower viscosity in the aqueous slurry. Al-rich fluorophyllosilicates ($[Si_8]^{IV}$-$[Al_{4-y}Zn_y]^{VI}O_{20}(OH, F)_4$, $y' = 0.4$ and 0.8) were synthesised at 220 °C in the presence of HF.[360,413] Despite the large difference in the ionic radius between Al^{3+} and Zn^{2+}, they were adjacent to each other (miscible) and bridged by oxygen in O.

Dioctahedral-type 2:1 phyllosilicates (montmorillonite, $[Si_8]^{IV}[Al_{4-y}Mg_y]^{VI}O_{20}(OH)_4$ in the most common example) have vacancies in O. Interlayer Li^+ is migrated to O to decrease the layer charge. This phenomenon is named the Hoffman–Klemen effect.[414] This is a method for the post-adjustment of the y value in this smectite system. The reduced charged silicates have been used[415] as a clay-based gas barrier film,[416] adsorbents for a cationic dye,[417] a polymer,[418] and organic contaminants.[419–422]

LAPONITE® is a synthetic hectorite, in which Li^+ is fixed in O: $[Si_8]^{IV}[Mg_{6-y}Li_y]^{VI}O_{20}(OH)_4$, and its reported formula is $Na_{0.7}[Si_8]^{IV}[Mg_{5.5}Li_{0.3}]^{VI}O_{20}(OH)_4$.[363,423] Its synthesis, characteristics, and applications were previously summarised in a review article.[424] A hectorite analogue was prepared using LiF, $Mg(OH)_2$, and silica sol under reflux condition[425] at the molar ratio of $Li:Mg:Si = 1.4:5.3:8$[426] in the starting mixture ($y' = 0.7$ in $[Si_8]^{IV}[Mg_{6-y}Li_y]^{VI}O_{20}(OH, F)_4$, where the amount of Li was twice in the formula). Fluoride in LiF was proposed to be an accelerator for crystallisation.[425] The structural OH group was partially substituted with F. Tetraethylammonium was used to assist crystallisation and incorporated as an exchangeable cation.[427] A small amount of actinoids (Am^{3+}[364] and Cm^{3+}[365]) and lanthanoids (Eu^{3+})[428] in the range of $10^{-3}–10^{-5}/Mg^{2+}$ was doped in O of the tetraethylammonium form. Another example was proposed for preparing analogues at 180 °C by Torii and co-workers, where the atomic ratios of $Li:M:Si$ were $0.6:5.4:8$ ($M = Ni^{2+}$)[361] and $0.8:5.2:8$ ($M = Mg^{2+}$)[429] in the starting mixtures with the formula of $[Si_8]^{IV}[M_{6-y}Li_y]^{VI}O_{20}(OH)_4$.

The limitation of the Li^+-fixation in O was examined when hectorite was prepared using LiF, $Mg(OH)_2$, and SiO_2 by varied $Li:Mg:Si$ ratio in the starting mixture (Table 8).[430,431] The variation of y has been frequently discussed by CEC. The CEC varied empirically in the range of 40 to 90 meq/100 g, when y' ranges from 0.07 to 1.4 in $[Si_8]^{IV}[Mg_{6-y}Li_y]^{VI}O_{20}(OH)_4$. The high solubility of Li^+ in water and uncontrollable formation of vacancies in the MgO_6 octahedral sheet make it difficult to
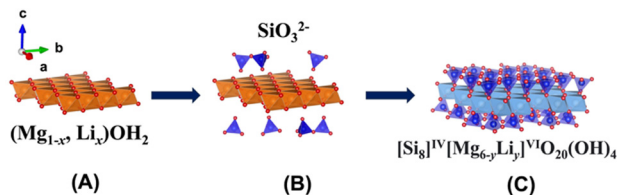
This journal is © The Royal Society of Chemistry 2024

Chem. Soc. Rev., 2024, 53, 10523–10574 | 10549
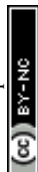
Fig. 21 Route for the formation of hectorite: (A) substitution or fixation of Li into brucite $Mg(OH)_2$ sheet, (B) adsorption of silicate anions on the octahedral sheet and (C) progress of the silicate anions to form the 2:1 type. phyllosilicate.[427]

precisely control the amount of Li^+-fixation in O. However, the Li^+/Mg^{2+} ratio in the starting mixture was dominant in determining the CEC, which was directly influenced by the Li^+-fixation in O. An excess amount of silica sol did not influence the layer charge density of the hectorite analogue.[432] Microwave and ultrasonication were used to promote the migration of Li^+ toward the vacancy in O to decrease the CEC.[433,434] It was difficult to obtain pure hectorite giving the remaining amorphous silica in the product.

The mechanism of Li^+-fixation in O is still controversial and two schemes were proposed, as follows: (1) migration of Li^+ from the interlamellar to O upon heat treatment[435] and (2) substitution or Li^+-fixation into O during the hydrothermal reactions (Fig. 21).[427] Regarding the formation of 2:1-type phyllosilicate, the mechanism in the initial stage was kinetically discussed using an *in situ* SAXS technique during the reactions for 48 h at 100 °C.[427] The SAXS data showed a progressive increase in the power law value with time from 2.39 to 3.36 recorded at a low Q (nm^{-1}) region, indicating condensation into more dense structures. The ^{29}Si MAS NMR spectra displayed a Q^3 signal, referring to the number of branching units typical of sheet silicate structures, which appeared after 1 h and intensified after 4 h, the time at which a (001) reflection (1.50 nm) at a high Q (nm^{-1}) region was observed in the SAXS pattern.

4.5. Synthetic methods for 2:1-type phyllosilicates

2:1-type phyllosilicates have been synthesised[370] and the methods can be classified into three groups, as follows: (i) precipitation from an aqueous solution at room temperature and

0.1 MPa for a long time (Section 4.5.1), (ii) hydrothermal reactions of a stoichiometric mixture of amorphous and/or crystalline oxide solids (Section 4.5.2), and (iii) melting of oxides in metal fluorides as a flux *via* solid-state reactions (Section 4.5.3).[370] Part (i) evokes chemical weathering including lateritic weathering condition as precipitation of amorphous $Al(OH)_3$ with coprecipitating goethite and silica.[436] Homogeneously mixed glasses are preferred in (ii), which are evoked from quenching magma/lava by water.[368,369,437] (iii) High-purity reagents are necessary for stoichiometry in a fluorine medium at a high temperature.[352]

4.5.1. Precipitation of 2:1-type phyllosilicates under ambient conditions. Smectite was precipitated from low-concentration solutions of SiO_2 (30 ppm) and Al_2O_3 (3 ppm) at 20 °C for 3 months at a high Mg^{2+} concentration and higher pH. Its formation mechanism was explained as the initial formation of $Mg(OH)_2$, followed by the polycondensation of silica on the brucite layers.[438] Under alkaline conditions (pH 9–10), it was possible to precipitate 10 ppm Mg, whereas at pH 8, 1250 ppm Mg (seawater concentration) was necessary.[438] Subsequently, the polycondensation with silica sol was followed by forming a T–O–T layer. Even at a dilute Zn^{2+} concentration (1–2.5 ppm), a smectite containing Zn^{2+} in O was formed at 20 °C by aging for 1 year.

The effective ionic radius of the components are important factors in designing 2:1-type phyllosilicates with a controlled composition (Table 10). The presence of Fe^{2+} enabled the formation of O.[436] Harder also suggested that the small size of Al^{3+} made it difficult to be installed in O, whereas appropriate sizes ranging 0.078 to 0.082 nm[436] or 0.069 to 0.078 nm[129] were necessary to form O. This is a reason for the formation of an Fe^{2+}-rich (ferruginous) phyllosilicate under reducing conditions. It became possible to crystallise tetrahedrally coordinated Al^{3+} in 2:1-type phyllosilicates with the help of divalent cations, which enable the direct formation of phyllosilicates. The mechanism for the primary formation of O seems to be different from that for the formation of Mg–Al/LDHs (uptake of Mg^{2+} by the Al hydroxide is the possible reaction for the formation of the LDH).

Organosilanes were reacted at room temperature with metal chlorides to form 2:1-type phyllosilicate derivatives,[439,440]

Table 10 Influence of ionic radius on the formation of 2:1-type phyllosilicates at surface temperatures from chemically pure solutions

	Effective radius of ion in octahedral coordination[ab]/nm		Synthesis of 2:1-type phyllosilicates[a]
Mg^{2+}	0.078	0.0720	Possible
Ni^{2+}	0.078	0.0690	Possible
Co^{2+}	0.082	0.0745 (HS: high spin)	Possible
Zn^{2+}	0.083	0.0740	Possible
Fe^{2+}	0.082	0.0780 (HS)	Possible
Fe^{3+}	0.067	0.0645 (HS)	Not possible under oxidative condition
Cu^{2+}	0.070	0.073	Difficult in chemically pure solutions
V^{3+}	0.065	0.0640	Difficult in chemically pure solutions
Cr^{3+}	0.064	0.0615	Difficult in chemically pure solutions
Mn^{2+}	0.091	0.0830 (HS)	Probably too large for clay minerals
Mn^{3+}	0.070	0.0645 (HS)	Difficult
Al^{3+}	0.057	0.0535	Not possible in chemically pure solutions at low temperatures

[a] H. Harder, *Clay Miner.*, 1977, **12**, 281–288.[436] [b] R. D. Shannon, *Acta Cryst., A*, 1976, **32**, 751–767.[129]

10550 | *Chem. Soc. Rev.*, 2024, **53**, 10523–10574

This journal is © The Royal Society of Chemistry 2024

Table 11 Apparatus for the synthesis of clay minerals[452]

Reactions	Reactor	Maximum pressure	Maximum temperature (°C)	Scale of production (mL)
Precipitation	Beaker	Atmospheric	100	No upper limit
Hydrothermal reactions	Morey type	50 MPa	350	<1000
	Autoclave	200 MPa	600	<1000
	Test tube	1 GPa	1100	<0.5
	Internal heat type	1 GPa	1400	<30
	Pin cylinder type	6 GPa	1800	<0.1
	Belt type	8 GPa	2500	<1000
	Bridgman anvil	30 GPa	3000	<0.01
	Diamond anvil	200 GPa	3000	10^{-5}
Solid-state reactions	Electronic furnace	Vacuum $\sim$ atmospheric	1700	<50

which were later named "aminoclay"[441,442] and "organo-talc",[443] after the pioneering study by Fukushima and Tani on the preparation of 2:1-type 3-(methacryloxy)propyl phyllosilicate with $O = Mg^{2+}$, Ni^{2+} for a polymer additive.[444,445] The amphiphilic nature of $RSiO_3$ ($R = C_8H_{17}$) also assisted the formation of a T–O–T layer at room temperature; this type of octylsilyl derivative of 2:1 phyllosilicate is based on the structural formula of $[Si_{8-x}Al_x]^{IV}[Al_4]^{VI}O_{20}(OH)_4$[446,447] and $[Si_{8-x}Al_x]^{IV}[Mg_6]^{VI}O_{20}(OH)_4$.[447–449] Reflux or hydrothermal conditions were employed to prepare various functionalised phyllosilicate derivatives ($R = CH_3$,[450] C_6H_6,[450] 3-(methacryloxy)propyl,[451] and 3-acryloxypropyl[451]) based on the structure of $[Si_8]^{IV}[Mg_{6-y}Li_y]^{VI}O_{20}(OH)_4$. It is worth examining the incorporation of heteroelements in the T of these organic derivatives of 2:1 phyllosilicates.

4.5.2. Hydrothermal synthesis of 2:1-type phyllosilicates. The apparatus and the conditions for the preparation of smectites are listed in Table 11 with the upper limits of pressure, temperature, and mass of product for each apparatus.[452] A hectorite analogue, $[Si_8]^{IV}[Mg_{6-y}Li_y]^{VI}O_{20}(OH, F)_4$, was obtained, as described in Section 4.4.3, and the dosage of organic molecules or cations assisted its crystallisation.[453] The nominal compositions for Mg and Si in the initial mixture were maintained after the crystallisation, whereas a larger amount was required for the Li dosage because of its high solubility in water. (The reaction mechanism was already introduced in the Section 4.4.3.) The reactions were performed using Morey-type autoclave, where the pressure is often autogenous water pressure. Researchers prepared materials of desired structures and compositions based on the phase diagram under controlled pressure, if available (Section 4.4.1). Smectite single crystals of several tens of micrometers in lateral size were successfully synthesised at pressure higher than 3 GPa (up-to 5.5 GPa) and temperature of 1000 °C using a belt-type high-pressure apparatus.[454] The smectite crystals were considered to be quenched crystals metastably formed from the hydrous silicate melts formed at high pressures and temperatures.

4.5.3. Ceramic processes; solid-state reactions and the formation of 2:1-type phyllosilicate from melt. Solid-state and melt syntheses were applied to prepare 2:1-type phyllosilicates, where the OH groups in smectites were substituted with fluorine. The temperature and pressure in these syntheses were below 1700 °C and normal pressure, respectively (Table 11). Careful melt synthesis was investigated by Breu to prepare

fluorosmectites with nominal compositions of $Na_{1.0}[Si_8]^{IV}$-$[Mg_{5.0}Li_{1.0}]^{VI}O_{20}F_4$[352] and $K_{0.6}[Si_8]^{IV}[Mg_{5.4}Li_{0.3}]^{VI}O_{20}F_4$ with a homogeneous charge distribution.[455] High-purity reagents of LiF, MgF_2 (>99.9%), MgO (99.95%), NaF (99.99%), and washed and calcined SiO_2 (99.9%) were used.[352] To avoid gravity segregation in the melt, the crucible was aligned horizontally with rotation by 60 rpm during heating to 1550 °C for 1 h, and finally to 1650 °C for another 15 min. This method is advantageous for the large-scale production (0.85 kg[352]) of the product with a composition similar to the initial composition of $K_{0.96}[Si_8]^{IV}[Mg_{5.09}Li_{0.86}]^{VI}O_{20}F_4$.[455] High structural order was found for the synthetic fluorohectorite in contrast to smectites, and a huge aspect ratio of 20k was realised.[456] Accordingly, structural coloured nanosheet suspensions[366] and gas barrier films prepared from suspension were developed.[457–459] A stretchable nanocomposite barrier film for improving water vapour permeability was obtained by sandwiching poly(ethylene glycol) (PEG)-fluorohectorite crystalline (Bragg stack) barrier films between plasticised poly(vinyl alcohol) (PVOH) (Fig. 22).

A synthetic strategy was developed to obtain pillared clays with a homogeneous micropore distribution.[460–463] The homogeneous charge distribution was confirmed by the two-dimensional $3a \times b$ super-cell (Fig. 23A and B) in Me_2DAB-CO^{2+}(N,N-dimethyl-1,1-diazabicyclo[2.2.2]octane dication)-[460] and 2H-DABCO (diprotonated 1,4-diazabicyclo[2.2.2]octane)-exchanged fluorohectorites.[461]

Charge homogeneity was also shown in a high-charged phyllosilicate, an iron-containing Cs-exchanged mica $(Cs_{1.96}[Si_8]^{IV}[Fe^{2+}_{3.86}Li_{2.02}]^{VI}O_{20}F_4)$.[462] Fig. 23C illustrates the orientation of the pillar (Me_2DABCO^{2+}) with its C_3 axis tilted by approximately 24° against the ab plane. Although two of the C_2H_4 handles protruded into the silicate layers, the third one was in the hexagonal plane of the interlayer space.[463] The layer charge was reduced as CEC from 84 to 59 meq/100 g (Fig. 23) by the migration of interlayer Mg^{2+}, which was exchanged with interlayer K^+ in the pristine fluorohectorite.[455] The sizes and volume of the micropores created by Me_2DABCO^{2+} and tris(2,2′-bipyridine)rhodium(III) ($[Rh(bpy)_3]^{3+}$) increased by the reduction in the layer charge.

4.6. Characterisation of 2:1-type phyllosilicate

4.6.1. Layer charge density. The Green-Kelly test[464] using ethylene glycol vapour exposure is used to estimate the layer charge of the unit cell.[465] Solvation of the interlayer cation with

This journal is © The Royal Society of Chemistry 2024

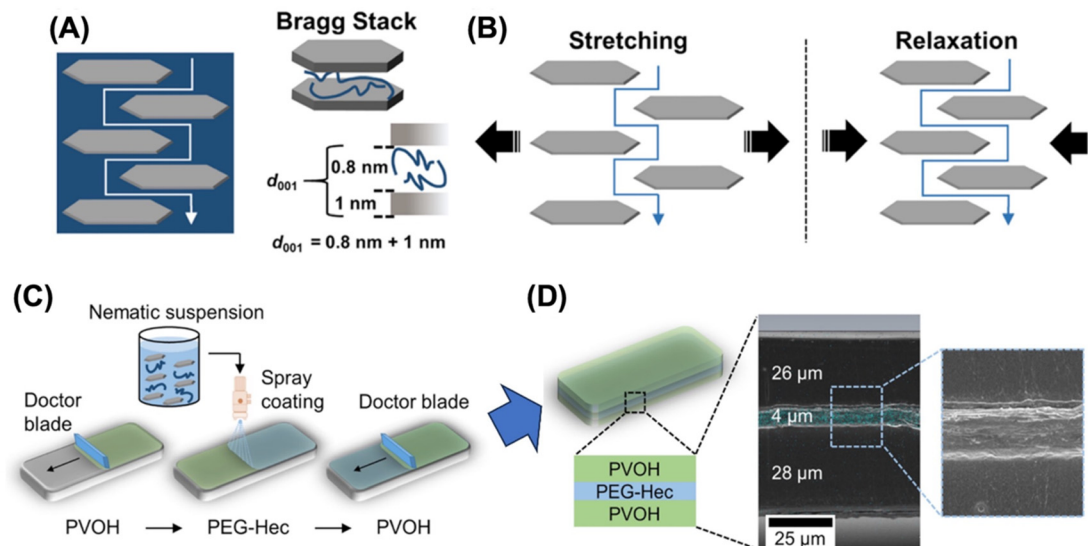*Chem. Soc. Rev.*, 2024, **53**, 10523–10574 | **10551**

Fig. 22 (A) Sketch of the tortuous path (white) of a gas permeate dodging impermeable clay nanosheets incorporated in a polymer matrix (blue). (B) Tortuous path of a clay nanocomposite barrier film upon uniaxial stretching and relaxation. (C) Sketch of the sequential coating process to produce a self-standing barrier laminate. (D) Schematic structure and SEM micrographs of a cross section of the self-standing barrier laminate. Elemental mapping of Si (cyan) *via* EDX spectroscopy indicates no interdiffusion of fluorohectorite nanosheets into the poly(vinyl alcohol) (PVOH) layers.[457]
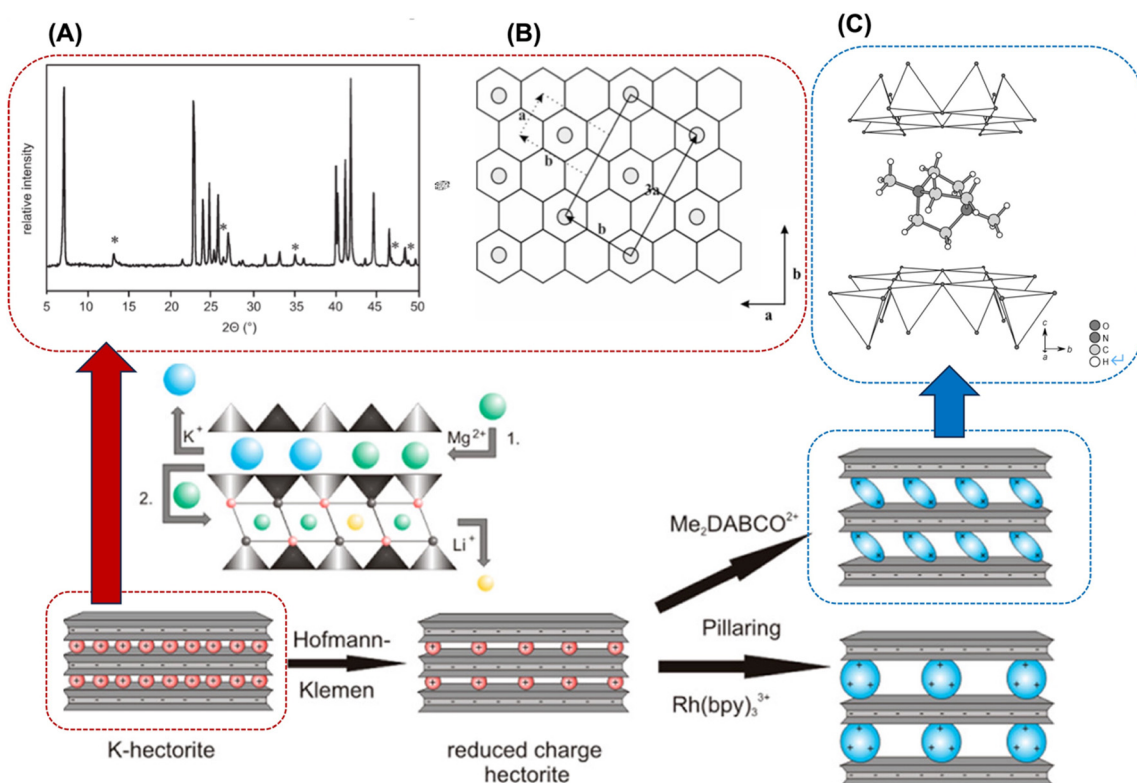
Fig. 23 Schematic of pillaring process using Me_2DABCO^{2+} (*N*,*N*-dimethyl-1,1-diazabicyclo[2.2.2]octane dication) and tris(2,2′-bipyridine)rhodium(III) ([$Rh(bpy)_3$]$^{3+}$). The layer charge was reduced by the migration of Mg^{2+}, which was exchanged with K^+ in the pristine fluorohectorite.[455] (A) Powder XRD pattern of 2H-DABCO-ecchanged fluorosmectite. Asterisks (*) mark reflections due to the two-dimensional $3a \times b$ super-cell. (B) Scheme of the $a \times b$ super-cell of pillars in 2H-DABCO-fluorosmectite. The unit cell of the parent fluorohectorite is shown as dotted lines.[460] (C) Results of the X-ray single-crystal refinement (tetrahedral sheet of the layered silicate and Me_2DABCO^{2+} in the interlayer space).[463]

ethylene glycol expands the interlayer space in K^+-saturated smectites, accompanied by an increase in the d_{001} spacing upon

reducing the layer charge. The *LayerCharge* computer code[466] determined the layer charge (a lower threshold of 0.39 e$^-$/half
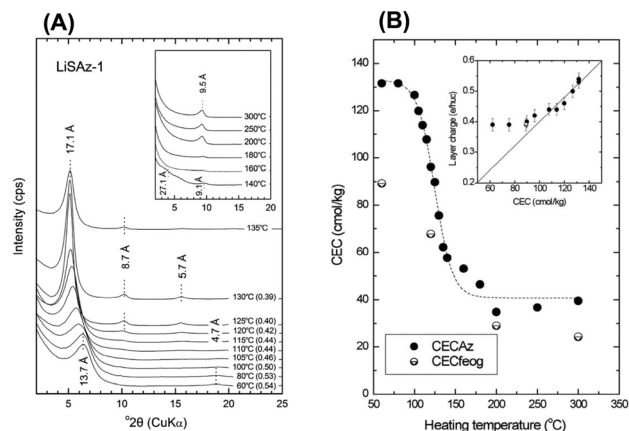
Fig. 24 (A) Room-temperature XRD patterns of K-saturated and ethylene glycol-solvated LiSAz-1 samples pre-heated in the range of 60–135 °C for 24 h. Layer charges (e$^-$/(Si, Al)$_4$O$_{10}$(OH)$_2$) calculated according to ref. 465 are shown in parentheses. The inset shows the patterns of the corresponding samples heated at higher temperatures and up to 300 °C. Note the appearance of a new peak ∼9.5 Å, which indicates collapsed layers. (B) Dependence of CEC on the heating temperature. The inset compares the layer charge and CEC data of the same samples. Reprinted with permission from ref. 466. Copyright 2013, Springer.

of the unit cell). A temperature in the range of 60 °C to 130 °C increased the d_{001} spacing from 1.37 to 1.71 nm (Fig. 24A) with a decrease in the layer charge from 0.54 to 0.39 e$^-$/half of the unit cell. Above this temperature, the ordering of the lamellar structure became lower, whereas a reduction in CEC, which was determined by the reactions with ammonium acetate, was observed (Fig. 24B).

Quantitative ion exchange of the interlayer cation with a series of alkylammonium ions using varying alkyl chain lengths has been proposed as a method for the determination of the layer charge density.[467] The d_{001} spacing should increase with the layer charge of 2:1-type phyllosilicates (Fig. 25), corresponding to the inclination of the alkyl chains. Owing to their adsorption selectivity in 2:1-type phyllosilicates, alkylammonium ions are a good indicator of estimating the layer charge, even when accessory minerals are present. After the ion exchange, interactions of another guest (solvent) with the intercalated alkylammonium became a dominant driving force for the guest inclusion to expand the interlayer space[468,469] in several
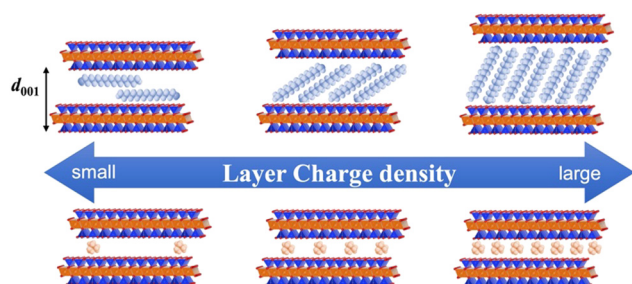
Fig. 25 Schematic of the variation in the arrangements of the intercalated alkylammonium ions in 2:1-type phyllosilicates depending on layer charge density.

applications as rheology-controlling agents[318,469] and plastic fillers.[470] Purification and classification were necessary to optimise the performances of the materials.[471–473]

4.6.2. Li$^+$-fixation in O. Li$^+$-fixation in O was examined based on the stretching vibration of OH in O in the IR spectrum.[465] The second derivative spectra of Al–OH stretching in O were employed to determine the anharmonicity value X (eqn (5)).

$$X = (2\nu_{01} - \nu_{02})/2 \qquad (5)$$

where ν_{01} and ν_{02} are the frequencies of the stretching vibration and its overtone, respectively. The X value ranged from 87–88 cm^{-1} for the dioctahedral and 84–85 cm^{-1} for the trioctahedral types. When a dioctahedral smectite (SAz-1) was heated at 300 °C, the X value decreased to 85 cm^{-1}, indicating the fixation of Li$^+$ into the Al^{3+}–Al^{3+}-vacancy in O (forming trioctahedral sheet).

The migration of Li$^+$ into montmorillonite was investigated by ^{7}Li NMR.[474] Heat-treatment up to 250 °C split the signals at −0.16 and −0.60 ppm. The former signal, which was observed before heating, was attributed to the tetrahedrally to pentahedrally coordinated Li$^+$ located in the interlayer space in a symmetrical environment due to the presence of water. The spectral shift to −0.60 ppm upon heating at 250 °C indicated a more strongly bonded cation in the octahedral coordination. Combined with the ^{19}F-MAS NMR result, the Li$^+$ migration occurred in two steps, as follows: at 110 °C, 86% of Li$^+$ moved to the hexagonal cavity of the basal surface in T. The remaining interlayer Li$^+$ migrated progressively to this cavity upon heating at 170 °C to 250 °C.

The chemical shift of the resonances in the ^{19}F NMR spectra is determined by the average electronegativity of the groups attached to F. Therefore, it was employed to determine the elements in O.[439] The larger electronegativity of Zn^{2+} than Mg^{2+} resulted in a less (shielded) chemical shift in a fluorohectorite. The incorporation of Li$^+$ into vacancies of O was reflected in the resonances; it was ascribed as F bound to three elements in O, either containing two Zn^{2+} and one Li$^+$ or one Zn^{2+} and two Li$^+$.

4.6.3. Location of the heteroelements in 2:1-type phyllosilicate. The coordination numbers of the heteroelements are a clue to monitor their location. Although ^{27}Al-MAS NMR spectroscopy is a method for identifying coordination, the quantitative analysis of the ^{27}Al spectra is difficult[475] because of the strong ^{27}Al resonances in Al in T. The resonances due to Al^{3+} in O are considerably weaker than that expected based on chemical analysis. An amorphous aluminium (hydro)oxide would also interrupt the accuracy. ^{29}Si MAS NMR spectra provided supporting evidence for the Al occupancy.[476] The ^{29}Si spectra of the synthetic [Si$_{8-x}$Al$_x$]^{IV}[Mg,Zn$_6$]^{VI}O$_{20}$(OH)$_4$ displayed three Q-type signals at approximately −94, −90 and −85 ppm, corresponding to Q^{3}Si(0Al), Q^{3}Si(1Al) and Q^{2}S, respectively.[384]

Given that the d spacing of the (060) reflection in XRD reflects the ionic radius of the main components in O,[477] it has been used to identify dioctahedral (Al^{3+}–Al^{3+}-vacancy) or trioctahedral (Mg^{2+}–Mg^{2+}–Mg^{2+}) type. Depending on the amount of heteroelements in O, the d_{060} spacing changes.[354] Although the similar ionic radius of Ni^{2+} and Mg^{2+} made it

This journal is © The Royal Society of Chemistry 2024

Chem. Soc. Rev., 2024, **53**, 10523–10574 | **10553**

difficult to identify (d_{060} = 0.1520 and 0.1523 nm), the difference in the ionic radius between Ni^{2+} and Co^{2+} caused a change in the d_{060} spacing, respectively. This obeyed Vegard's law, which is interpreted as direct proof of a solid-solution. In the case of Fe^{3+} and Mg^{2+}, because of the small difference in their ionic radius, a linear change was observed in the relationship between the composition and the d_{060} spacing. On the contrary, in the case of the Mg^{2+}–Al^{3+} combination, the relation was not linear, indicating the immiscibility of Al^{3+} and Mg^{2+} in O. The IR absorption band of OH stretching in O is useful as an alternative to d_{060} when the ionic radius of two cations is similar.[354]

^{19}F NMR was used to discuss the states of the heteroelements. Zn^{2+} and Al^{3+} were miscible in O of a fluorophyllosilicate ($[Si_8]^{IV}[Al_{4-y}Zn_y]^{VI}O_{20}(OH, F)_4$, y' = 0.4 and 0.8), as indicated by the splitting of the signal in its ^{19}F NMR spectrum, where one was attributed Zn^{2+}–Al^{3+} (−142 ppm) and the other Al^{3+}–Al^{3+} (−133 ppm).[360] The former signal was intense when the y value increased from 0.4 to 0.8.

Extended X-ray absorption fine structure (EXAFS) spectroscopy has been used to monitor the local structures of O. A fluorophyllosilicate ($[Si_8]^{IV}[Al_{4-y}Zn_y]^{VI}O_{20}(OH, F)_4$, y' = 0.4 and 0.8 in nominal) was examined to determine its interatomic distances and the apparent (average) coordination number of Al^{3+}.[360] In addition to the interatomic Zn^{2+}–Zn^{2+} distance of 0.311 nm, a short distance of 0.298 nm was obtained, indicating neighbouring Zn^{2+} with Al^{3+} between the oxygen in O. The coordination number was four, indicating the presence of vacancy in O, as well as Si^{4+}–Al^{3+} substitution in T.

4.6.4. Possible roles of iron as the heteroelement. Iron in smectites decreases the NMR spectral resolution and complicates the interpretation of the local structures because of its paramagnetic effects. Thereby, IR, Mössbauer, and EXAFS spectroscopy are useful tools for monitoring iron-containing structures. Also, in NMR studies, leaching iron from the samples and preparing non-iron samples are required.

Mössbauer spectra have been used to examine the valence, coordination number, and structural symmetry of Fe in smectites.[478] Given that the quadrupole shift (QS) and the isomer shift (IS) of high-spin Fe^{3+} are smaller than that of high-spin Fe^{2+} and their values are defined, the Fe^{2+}/Fe^{3+} ratio can be determined. The QS of Fe-containing clays is reversibly changed by the oxidation/reduction of Fe.[367,479,480]

Dithionite ($S_2O_4^{2-}$) and hydrazine (N_2H_4) were used to reduce Fe in smectites.[481] The reduction of the structural Fe^{3+} was proposed[482] based on the literature[400] using sodium dithionite in a citrate-bicarbonate buffer solution as the reducing agent. The layer charge increased upon the reduction of Fe^{3+}. Stucki and Roth[483] proposed that a couple of hydroxyl groups bound to Fe^{2+} and Fe^{3+} in O was removed by releasing H_2O, followed by combining H^+ in the aqueous solution with the remaining oxygen atoms in O to form a hydroxyl group. The resulting OH group was predicted to bind to Fe^{2+} and Fe^{3+} as pentahedral coordination (later this prediction was modified to Fe maintains octahedral coordination after complete reduction through Fe-EXAFS studies[409]). Gan et al. used a two-step reduction for the reduction of Fe^{3+},[484] generation of SO_2^-·

radical from sodium dithionate and the reduction of Fe^{3+} by combining with H^+ in the solution, which compensated the charge generated by the removal of the hydroxyl group in O.

Fe^{2+} in a reduced Fe-rich smectite was examined to apply the products of varying layer charges obtained by Li^+-fixation.[367] Mössbauer spectroscopy proved that more than 20% of the total Fe was stabilised as Fe^{2+} by heat treatment in N_2 at 260 °C for 24 h.

4.7. Summary and perspectives

In O of montmorillonite, $[Si_8]^{IV}[Al_{4-y}Mg_y]^{VI}O_{20}(OH)_4$, the two cations with oxygen between are not necessarily next to each other (described in Section 4.4.2). After the formation of the brucite $Mg(OH)_2$ layer, the condensation of silicate anions on the layer gave 2 : 1-type phyllosilicate (T–O–T layer: Fig. 21). This reaction was rapid (preferential adsorption of silicate anions to carbonate ones) compared to substituting Al^{3+} for Mg^{2+}. Dissolved CO_2[436,438] and carbonate anions[485,486] did not affect the formation of trioctahedral smectite.[486] The large difference in ionic radii between Mg^{2+} and Al^{3+} is the reason preventing Al^{3+} substitution in O.[438] Therefore, the expression of the isomorphous substitution, $[Al_{4-y}Mg_y]^{VI}$, in the formula of montmorillonite should be apparent or nominal, and the negative charge should originate from the vacancy in O.

A high concentration of Al^{3+} in the starting mixtures or a high temperature was necessary to obtain a dioctahedral smectite, beidellite ($[Si_{8-x}Al_x]^{IV}[Al_4]^{VI}O_{20}(OH)_4$). Al^{3+} and Zn^{2+} coexisted in O of fluorophyllosilicate ($[Si_8]^{IV}[Al_{4-y}Zn_y]^{VI}O_{20}(OH, F)_4$, y' = 0.4 and 0.8 in nominal) (Section 4.4.3).[360]

According to Loewenstein's rule, the amount of Si^{4+}–Al^{3+} substitution in T is limited within Al/Si = 1/3, as shown in Table 8 (A recent ^{17}O-MAS NMR study should be noted as being in disagreement with Lowenstein's rule with Si^{4+}–Al^{3+} substitution in T of synthetic micas[487]). The charge per unit cell ($x + y$) of smectites is in the range of $0.4 \leq x + y \leq 1.2$, which is approved by the AIPEA Nomenclature Committee or the IMA Commission on New Minerals and Mineral Names. This range resulted from the limitation of Si^{4+}–Al^{3+} substitution in T, in addition to the amount of vacancy in O. The amount of vacancy in O should be influenced by the solution pH during the formation, given that vacancies may arise if the sheet expansion rate of T is higher than that of O (Section 4.4.3). Further kinetic study on the balance of the sheet expansion will optimised the amount of vacancies. The migration of Li^+ from the interlayer space toward the vacancy (Hoffman–Klemen effects) reduces the negative charge by heating at around 250 °C, losing hydrated water around Li^+ (Section 4.6). The mechanism of the incorporation of Li^+ in O of hectorite during the synthesis (during precipitation or drying) is still unclear (Section 4.4.3).

The synthesis of 2 : 1-type phyllosilicates with various heteroelements at 220 °C or lower temperatures was overviewed (Section 4.4.2 and Table 8). The cations with similar ionic radii, 0.07 nm, in O (e.g., O = Ni^{2+}–Co^{2+} [354] and Mg^{2+}–Fe^{3+} [410]) were miscible in O based on Vegard's law (Section 4.6). As schematically shown in Fig. 26, the Ni^{2+} and Mg^{2+} cations at a 1 : 1 atomic ratio became miscible in a 2 : 1-type phyllosilicate, when the synthesis temperature was increased from 100 °C to

10554 | Chem. Soc. Rev., 2024, **53**, 10523–10574

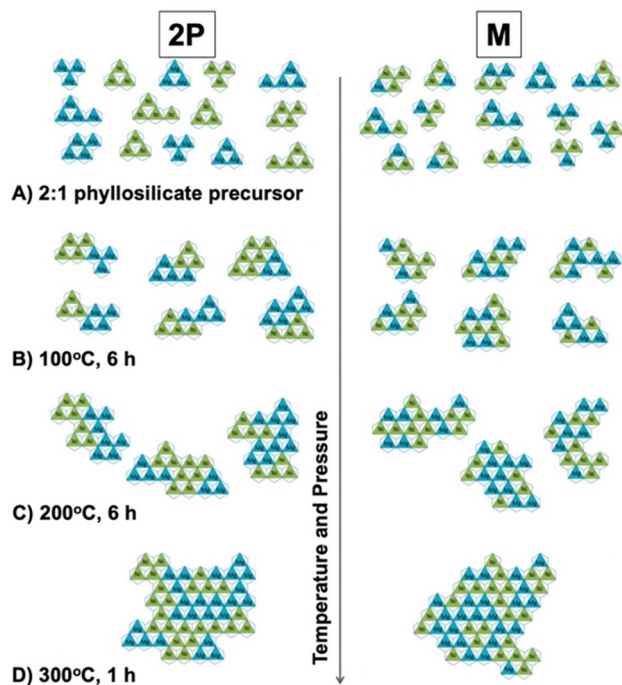This journal is © The Royal Society of Chemistry 2024

Fig. 26 Proposed model of the locational changes in Mg^{2+} (blue) and Ni^{2+} (green) at 1:1 atomic ratio under hydrothermal conditions in the octahedral sheet of a phyllosilicate. Conditions are (A) after precursor precipitation, after synthesis at (B) 100 °C, (C) 200 °C, and (D) 300 °C for 6 h. The model was also compared based on the difference in the precursor preparation (2P and M), where 2P and M designate subsequent and simultaneous dosages of Mg^{2+} and Ni^{2+}, respectively. Reprinted with permission from ref. 488. Copyright 2015, the American Chemical Society.

300 °C.[488] However, hydrothermal synthesis at 300 °C may be difficult to prevent the thermal decomposition of the target mineral and cogeneration of accessory minerals. Although water is a commonly used flux for crystallising 2:1-type phyllosilicates, the location and the amount of heteroelements in the products were not critically controlled. The fluorohectorite prepared by solid-state reaction at 1650 °C (Section 4.5.3) had a highly homogeneous charge distribution.[352,366,455–458]

In addition to precise control of the charge distribution, incorporating functional units in the silicate layers is a challenging task for designing multiply-functionalised materials, as shown by the redox ability in Fe-containing bentonite[386,401] (Sections 4.4.2 and 4.6.4). The aforementioned hybridisation of LDHs with functional particles (Section 2.6) was also reported in a 2:1-type phyllosilicate structure for modifying and improving its performances.[489–491] Huge crystals (high aspect ratio)[456] exhibit superior functionalities including optical[457] and gas barrier properties (Section 4.5.3).[458] The structural and morphological variation in 2:1-type phyllosilicates will satisfy the requirements in photochemical reactions, optics, selective adsorption, and catalysis and lead to unexplored applications.

5. Layered transition metal oxides

Besides the layered oxides and hydroxides of main elements, layered transition metal oxides with interlayer reactivity are
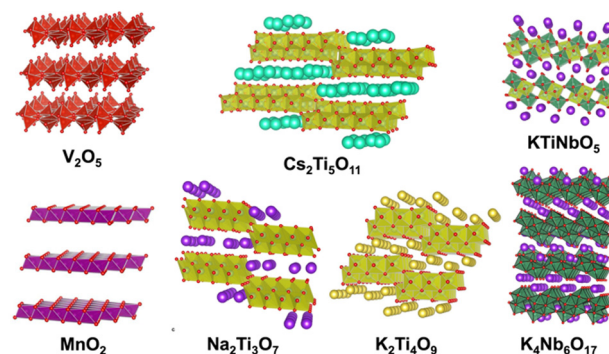
Fig. 27 Variation in LTMOs.[492–498] The crystal structure was drawn using the VESTA program.[44]

known (hereafter abbreviated as LTMO) (Fig. 27).[492–498] LTMOs are distinguished from the layered oxides/hydroxides of main elements by the variation in their electric, electronic, optical, and magnetic characteristics. Similar to bulk transition metal oxides, the characteristics of LTMOs are designed by isomorphous substitution.

Simple metal oxides with layered structures such as RuO_2, V_2O_5 and MnO_2 are known.[499–502] These LTMOs accommodate cations through redox reactions. For example, a layered MnO_2 (birnessite) accommodates alkali or alkaline earth metal ions in its interlayer space for compensating the negative charge of the host layer, which is caused by the difference in the oxidation state of manganese ions. The layer charge is variable depending on the redox reaction employed, and the average oxidation state of the manganese in birnessite was reported to be between 3.4 and 3.99.[502] Although V_2O_5 and MnO_2 have been synthesised through solution routes,[501,502] some metal salts of LTMOs (layered alkali titanates and layered alkali niobates are known examples) with a defined stoichiometry (e.g., $A_2Ti_nO_{1+2n}$) are obtained by solid-state reactions. The incorporation of heteroelements in LTMOs and their characteristics such as chemical, electric, electronic, magnetic, and optical properties have been examined thus far.

Ion exchange reaction is used to tune the characteristics of LTMOs. For example, the protonated forms of LTMOs, which are obtained by the acid treatment of LTMOs, exhibit characteristics different from that of LTMOs. Protonated forms of LTMO are exfoliated into nanosheets through an ion exchange reaction with the appropriate alkylammonium salts.[503–506] The obtained nanosheet is regarded as an anisotropic single crystal of transition metal oxide with an atomic-order thickness and bulk lateral size. As a unique magneto-optical property, an LTMO nanosheet with a high-aspect ratio was shown to orient along the magnetic field and its orientation was switchable by photoirradiation, which reduced Ti^{4+} in the LTMO nanosheet and Ti^{3+} was oxidised in the dark spontaneously, suggesting that the LTMO-based nanosheet is likely to be applicable as an optical switch operated by light and magnet (Fig. 28).[507] The nanosheets were deposited on a substrate by drop casting,[508–510] Langmuir–Blodgett method,[308] layer-by-layer assembly[510,511] and spin-coating[512,513] for device design.[514]
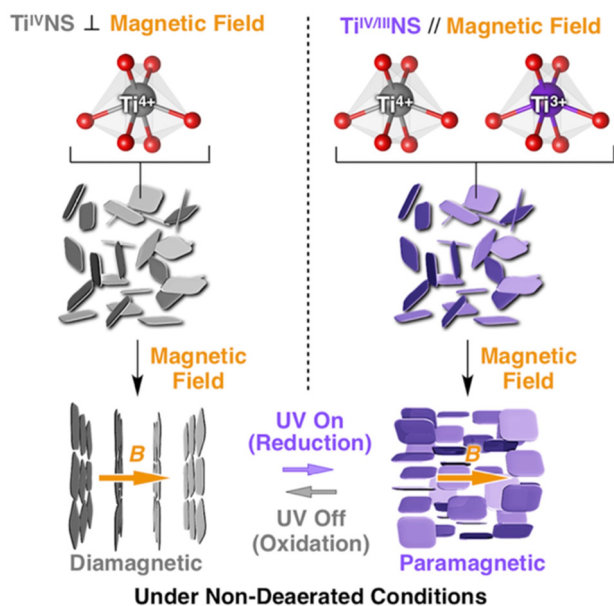
This journal is © The Royal Society of Chemistry 2024

Chem. Soc. Rev., 2024, 53, 10523–10574 | 10555

Fig. 28 Schematics of the magnetic orientation; Ti^{4+}-based nanosheet ($Ti^{IV}NS$; left) and its reduced form containing Ti^{3+} species ($Ti^{IV/III}NS$; right) orient their 2D planes orthogonal and parallel to the applied magnetic field, respectively. Reprinted from ref. 507. Copyright (2018), the American Chemical Society.

The nanosheets of LTMO were also used as building blocks of hetero-assemblies with other nanoparticles to design porous hetero-structures for application as electrodes, catalysts, photocatalysts, and adsorbents.[47,515–517] The layered structure with expandable interlayer space was useful for molecular recognition photocatalytic reactions.[518–520] Thus, the preparation and the modification of various LTMOs have been investigated for a wide variety of applications.

Fig. 29 shows the characteristics of LTMOs designed by isomorphous substitution. Isomorphous substitution has also been used to impart functional units in the LTMO lattice. For example, light-emitting materials by the emission from the rare earth elements in LTMOs have been reported.[521–524] Surface characteristics including soft-hard acid (surface ion mobility), swelling (dispersion) and acidity, which are correlated with application in solid-electrolytes, fillers (UV-absorber using the band gap absorption) and solid-acid catalysts, have been designed by isomorphous substitution. Different from the common targets reported for main element oxides/hydroxides (Sections 2–4), the band structure of LTMOs has been tuned by isomorphous substitution (doping), resulting in the designed electrical conductivity, magnetic and optical properties for a wide range of applications starting from superconductor to dielectric[525–527] applications. Among the many functions of LTMOs designed by isomorphous substitution, catalytic functions are a representative example. The substitution has been used to control the adsorptive properties and band structure as well as incorporate single-atom catalysts. In this review article, lepidocrocite-type layered titanates and a layered perovskite ($KCa_2Nb_3O_{10}$) (Fig. 30) will be introduced as representative

examples of LTMOs to explain the important effects of the incorporation of heteroelements in the structure of LTMO on their characteristics.
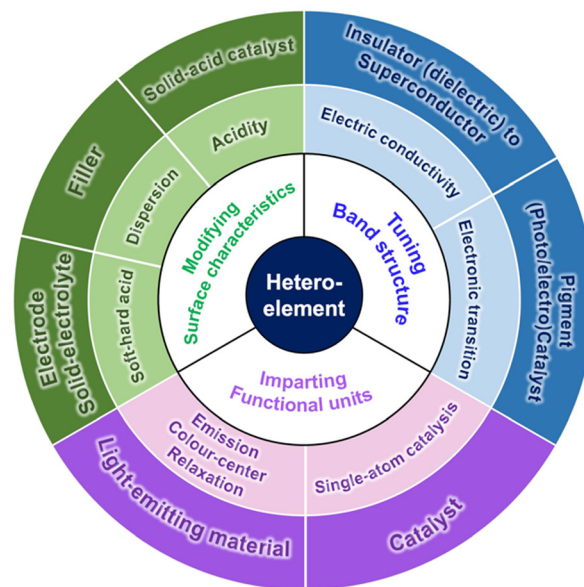
Fig. 29 Roles of heteroelements and the functions/applications designed by isomorphous substitution in LTMOs.

5.1. Crystal structures of lepidocrocite-type layered titanates and a layered perovskite ($KCa_2Nb_3O_{10}$)

Lepidocrocite-type layered titanates are characterised by s single-layer titanium oxide sheet, where the Ti in the octahedrally coordinated TiO_6 site is replaced with heteroelements.
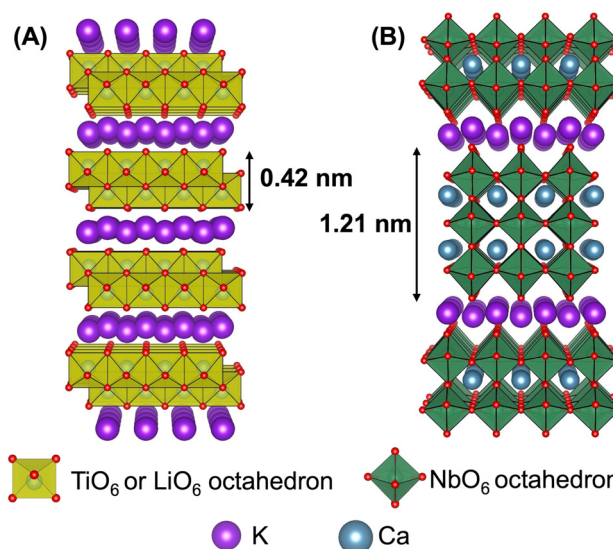

Fig. 30 Crystal structures of (A) lepidocrocite-type layered titanate $K_{0.8}Ti_{1.73}Li_{0.27}O_4$ and (B) Dion–Jacobson-type layered perovskite $KCa_2Nb_3O_{10}$. The structural parameters were referred from ref. 528 and 529, respectively. The crystal structure was drawn using the VESTA program.[44]

10556 | Chem. Soc. Rev., 2024, 53, 10523–10574

This journal is © The Royal Society of Chemistry 2024

Table 12 Functions of lepidocrocite-type layered titanate designed *via* isomorphous substitution

Function	M_{HE}	M_{HE}/M_{OE} (Ti) atomic ratio
Photocatalysis (Vis.)	Fe, Ni	1/5–2/5
Magnetism	Fe, Co, Mn	1/20–2/5
Solid acidity	Zn, vacancy	8.3/100–17.5/100

Layered perovskites have multilayered structures with varying compositions, where several sites can be replaced with hetero-elements. Perovskites with varying layer thicknesses have been designed, showing their extended possibilities. To make the discussion simple, examples of $KCa_2Nb_3O_{10}$ will be mainly introduced.

5.1.1. Heteroelement incorporation into lepidocrocite-type layered titanate. Lepidocrocite-type layered titanates consist of an anionic titanium oxide layer and exchangeable interlayer cation and characterised by the general formula $A'_a Ti_{2-x}M_{HEx}O_4$ (A', interlayer cation; M_{HE}, vacancy (h) or heteroelements such as Li, Zn, Ni, Co and Fe; $x = a/(4 - n)$, where a and n represent the number of interlayer cations per unit formula and the valence of the M_{HE} cation, respectively) (Fig. 30).[528–534] The 2D structure of the titanium oxide layer is formed by the assembly of 1D chains of edge-shared TiO_6 octahedron through edge-sharing along the a direction.[528] The negative charge in the titanium oxide layer arises from isomorphous substitution as $Ti^{4+} \rightarrow$ vacancy or M_{HE}^{n+} ($n < 4$). The origin of the permanent negative charge is similar to that for smectite. Ti is substituted with M_{HE} with the x of up to ~ 0.8 (equivalent to 2/5 of all the Ti sites), making its compositional variation wide. The functions of lepidocrocite-type layered titanate, which are designable by heteroelement and M_{HE}/M_{OE} (the original element, Ti) ratio, are summarised in Table 12. One application of lepidocrocite-type layered titanate taking advantage of its compositional variation is to construct a multilayer film of diluted magnetic semiconductors, which is useful in the field of spintronics.[535–539] The a value, which is equivalent to the number of interlayer cations per $Ti_{2-x}M_{HEx}O_4$ unit, was correlated with the interlayer cation species, and the typical value was reported to be 0.70, 0.75, and 0.80 for Cs, Rb, and K, respectively.[528] The low charge density ($2.63–4.00(-)$ nm^{-2}) compared with other LTMOs, which is likely favourable in accommodating guest species into the interlayer space based on relaxed the electrostatic interactions between the titanium oxide layer and interlayer cation, is another characteristic of lepidocrocite-type layered titanate. Consequently, lepidocrocite-type layered titanate has been used as a host material for designing nanostructured composites or exfoliated into titanate nanosheets through ion-exchange reaction with the tetrabutylammonium ion.[503,504,540]

5.1.2. Heteroelement incorporation into Dion–Jacobson-type layered perovskite. As a layered perovskite with ion-exchange ability, Dion–Jacobson phase $A'[A_{m-1}B_mO_{3m+1}]$ (A', interlayer cation; A, alkali earth metals; B, transition metals; m, thickness of the perovskite layer) is the most commonly reported example.[541–546] The crystal structure of $KCa_2Nb_3O_{10}$, a typical example of Dion–Jacobson phase, is shown in Fig. 30. Compared with the titanate layer of the lepidocrocite-type layered titanate $K_{0.8}Ti_{1.73}Li_{0.27}O_4$ (0.42 nm), the perovskite layer of $KCa_2Nb_3O_{10}$ (1.21 nm) is thicker, and Dion–Jacobson phases with a thicker layer are known.[547–550] The thickness of the perovskite layer has been correlated with the characteristics of the materials.[547,548,551–553]

Table 13 summarises the functions of the Dion–Jacobson phase with $m = 3$ depending on the heteroelement and the atomic ratio, M_{HE}/M_{OE}. The M_{HE}/M_{OE} ratio in both the A and B sites has been varied to tune the characteristics of layered perovskites.[554–561] The number of interlayer cations per unit formula (A') is variable, in accordance with the change in the charge density in the perovskite layer upon the substitution of M_{OE} by M_{HE} with different valence.[555]

5.2. The roles of heteroelements in the characteristics of LTMOs

5.2.1. Photocatalysis, controlled activity by heteroelements. Photocatalysis is a well-explored function of semiconducting LTMOs. Photocatalytic activity is correlated with their band structure, which can be modified by isomorphous substitution. As reactants can be diffused into the interlayer space, LTMO is regarded as a high surface area photocatalyst compared with its bulk counterparts. To take advantage of the large surface area per volume, exfoliation into LTMO-derived nanosheets has been done.[503,504] The colloidal suspension of nanosheets is beneficial for efficient light absorption due to the less light scattering as well as the quantum size effect. The nanosheets enable the smooth migration of photogenerated charges to the surface-adsorbed reactants, leading to efficient charge separation. The migration of electrons and holes to different directions based on the two-dimensional morphology

Table 13 Functions of Dion–Jacobson-type layered niobate ($m = 3$) designed *via* isomorphous substitution

Function	Isomorphous substitution					
	A site			B site		
	M_{OE}	M_{HE}	M_{HE}/M_{OE} atomic ratios	M_{OE}	M_{HE}	M_{HE}/M_{OE} atomic ratio
Electric conducting	Ca	La, Sr, Nd, Sm, Gd, Se	1/50–1/5	Nb	—	—
Dielectric	Ca, Sr	Sr, Bi	1/10–1/2	Nb	Ta	6.7/100–1/3
Photocatalysis	Ca	Sr	1/8–3/4	Nb	Mo, Ta	−1
Solid acidity	Ca	La	1/4–1	Nb	Ti	8.3/100–2/3
Electrocatalysis	Ca	—	—	Nb	Vacancy	3.3/100–13.3/100

This journal is © The Royal Society of Chemistry 2024

Chem. Soc. Rev., 2024, **53**, 10523–10574 | **10557**

of nanosheets has been pointed out as a beneficial aspect for efficient charge separation.[562,563]

The roles of isomorphous substitution are divided into two, as follows: (i) the control of band edges and (ii) the creation of localised energy states in the band gap. The position of the band edges (the valence band maximum and the conduction band minimum) determines the photo-absorption and the redox potentials of the semiconductors, which are important in energy conversion, energy storage, and energy transfer applications. Alternatively, excitation from the localised energy states to the conduction band minimum often imparts visible-light absorption to semiconductors whose band gap energy is equivalent to UV light. As another case, visible-light absorption associated with the colour centre created by oxygen vacancy formed for compensating positive charge deficiency was reported.[564] Compared with the control of the band edge positions, the amount of the heteroelement required for the localised energy state creation is generally small.[559,565]

The Ti in lepidocrocite-type layered titanate has been substituted by heteroelements with the M_{HE}/M_{OE} value of $\sim 2/5$, and the compositional variation has been correlated with the band structure modification.[566] As shown in Fig. 31, the absorption edge for a colloidal suspension of $K_{0.8}Ti_{1.2}Fe_{0.8}O_4$ nanosheet was located at the wavelength of *ca.* 400 nm, which is remarkably longer than that for the titanate nanosheet obtained from a lepidocrocite-type layered titanate containing vacancy, $Cs_{0.7}Ti_{1.825}h_{0.175}O_4$.[567] This indicated a decrease in the band gap energy by the Fe-incorporation. Also, the tail of the absorption edge was observed in the wavelength range of
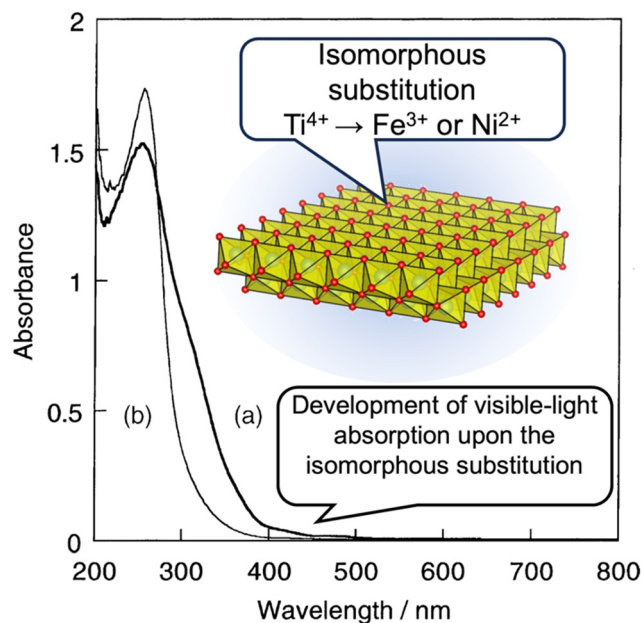
Fig. 31 Example of the functionalisation of lepidocrocite-type layered titanate by isomorphous substitution; development of visible-light absorption and red-shift in the light absorption edge. The absorption spectra correspond to an aqueous colloidal suspension (0.16 g dm^{-3}) of nanosheets derived from the protonated forms of (a) $K_{0.8}Ti_{1.2}Fe_{0.8}O_4$ and (b) $K_{0.8}Ti_{1.6}Ni_{0.4}O_4$.[566]
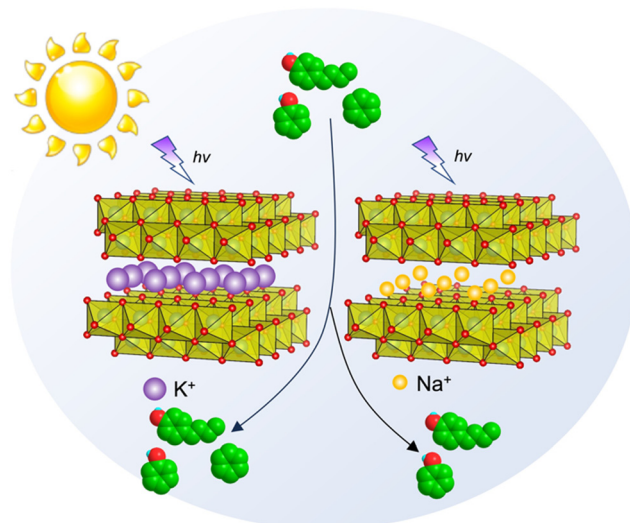

Fig. 32 Schematic of molecular recognition photocatalytic reaction induced by Na$^+$-type lepidocrocite-type layered titanate with reduced layer charge density.[519]

400 nm $\leq$ in both cases of $K_{0.8}Ti_{1.6}Ni_{0.4}O_4$ and $K_{0.8}Ti_{1.2}Fe_{0.8}O_4$, resulting in colouration of the suspensions. The light absorption in the visible-light region is presumably correlated with the energy transition between the localised energy states formed by the transition metal ions and the conduction band minimum. The Fe- and Ni-substituted titanate nanosheets were used as photocatalysts to decompose the poly(diallyldimethylammonium) (PDDA) located between the nanosheets in titanate nanosheet/PDDA alternative multilayers by visible-light, indicating the visible-light responsive photocatalytic activity taking advantage of the isomorphous substitution in the lepidocrocite-type layered titanate.[566]

The layer charge density, which is correlated with the isomorphous substitution in the metal oxide layer, is a parameter that affects photocatalytic reactions through the diffusion of reactants/solvents/products into the interlayer. The layer charge density of LTMO is determined by its structures, and its modification has been examined by the introduction of heteroelements in the metal oxide layer. Post-synthetic treatment is a way to control the layer charge density.[568,569] For example, the composition of a lepidocrocite-type layered titanate, $K_{0.8}Ti_{1.73}Li_{0.27}O_4$, was controlled by dilute HCl treatment and subsequent annealing process. The interlayer K$^+$ of the product with a decreased layer charge density was replaced with Na$^+$ for the selective decomposition of benzene in a ternary aqueous solution of benzene, phenol, and 4-buthyl phenol under UV-light irradiation (Fig. 32). This molecular recognition photocatalytic reaction was not observed when $K_{0.8}Ti_{1.73}Li_{0.27}O_4$ or bulk TiO_2 was applied.[519] The lepidocrocite-type titanate with reduced layer charge density was also used as a photocatalyst for the selective conversion of benzene to phenol under visible-light irradiation after the deposition of gold nanoparticles in the interlayer space.[520] These results reinforce the roles of isomorphous substitution in the photocatalytic

10558 | *Chem. Soc. Rev.*, 2024, **53**, 10523–10574

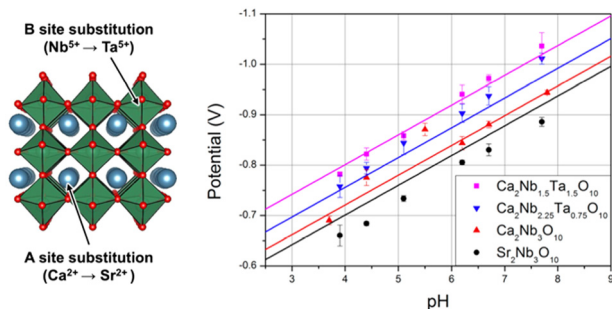This journal is © The Royal Society of Chemistry 2024

Fig. 33 Controlling the flat band position of perovskite nanosheet by iso-morphous substitution of A or B site. The flat band potential of the nanosheets with varied compositions on a tin oxide-coated glass was measured by Mott–Schottky method under valid pH.[573] The measured values are in good agreement with the Fermi level values estimated based on Matsumoto's empirical correlation between the conduction band-edge positions and band gap energies for metal oxide semiconductors (solid lines).[572]

activity of LTMOs through their controlled layer charge density and the band structure.

The band structure of layered perovskites has been controlled by isomorphous substitution with the elemental variation in the A and the B sites of the perovskite layer.[565,570] To correlate the element in the A or the B site with the band edge position in $KCa_2Nb_3O_{10}$, restacked-nanosheets of $KCa_{2-x}Sr_xNb_3O_{10}$ ($0 \leq x \leq 1.5$) and $KCa_2Nb_{3-y}Ta_yO_{10}$ ($0 \leq y \leq 1.5$) were obtained through exfoliation and re-assembly, and their optical properties and photocatalytic activity were investigated.[570] The more the A site element was substituted, the light absorption wavelength became longer. Alternatively, the opposite trend was observed for the case of the substitution of the B site element. These facts indicated that the band gap energies decreased and increased with an increase in Sr and Ta contents. The amounts of Sr (x) and Ta (y) were optimised at 0 and 1, respectively, for the photocatalytic H_2 evolution reaction, where photoexcited electrons reduced water, while photogenerated holes were consumed to oxidise an aqueous organic compound. Given that the valence band of d^0-transition metal cation-based oxides consists of O 2p orbitals[571] and the valence band maximum position is constant regardless of the composition,[572] the difference in the band gap energy indicated different conduction band minimum positions. Mallouk and co-workers applied the Mott–Schottky method to multilayers of $Ca_{2-x}Sr_xNb_3O_{10}$ ($x = 0$ or 2) or $CaNb_{3-y}Ta_yO_{10}$ ($0.75 \leq y \leq 1.5$) nanosheets assembled on a substrate by the layer-by-layer method to directly measure their flat-band potential, and successfully correlated the conduction band minimum position with the band gap energies (Fig. 33).[573] The synthesis of perovskite-based mixed anion compounds has been reported, and control of their valence band maximum position is also possible.[574–580] These results indicate the benefits of the compositional variation of Dion–Jacobson-type layered compounds for designing nanosheet-based opto/electronic materials with optimised band edge positions depending on the target applications.

Rh was incorporated into the Ti site in a lepidocrocite-type layered titanate containing vacancy[581] and the Nb site in $KCa_2Nb_3O_{10}$.[582] The nominal M_{HE}/M_{OE} ratio of $\sim 1/20$ and $1/100$ for the Ti site in a lepidocrocite-type layered titanate and the Nb site in $KCa_2Nb_3O_{10}$, respectively, was demonstrated for high photocatalytic activity in H_2 evolution from an aqueous solution of methanol compared with that loaded with Rh. Considering the amount of heteroelement, there is a possibility that the doped Rh contributed to the development of visible-light absorption properties by creating localised energy states in the band gap, while the role of Rh as a co-catalyst to suppress the charge recombination in the semiconductor nanosheets is also plausible.

The heteroelements in the titanium oxide layer of lepidocrocite-type layered titanate often leach upon acid-treatments,[528,583,584] and a defect site is generated to correlate the structural transformation of titanium oxide layer into rutile during the drying process in the air at room temperature with the aid of remaining Cl^- from the treatment with dilute hydrochloric acid.[585] A rutile nanoparticle-decorated protonated layered titanate exhibited high photocatalytic activity for the H_2 evolution reaction, benefiting from the created heterojunction, which enabled inter-particle electron transfer for retarding charge-recombination. The sensitising effect by rutile with a narrower band gap was also pointed out. This result demonstrates the beneficial aspect of defects originating from heteroelements in the design of lepidocrocite-type layered titanate-based photocatalysts.

5.2.2. Application of heteroelement incorporation in LTMO in solid-acid catalysis. The effects of isomorphous substitution on the solid-acidity of proton-exchanged LTMO have been investigated. To correlate the Brønsted acidity of $HCa_2Nb_3O_{10}$ with the heteroelements in the B site, a series of $HCa_{2-x}La_xNb_{3-x}Ti_xO_{10}$ ($0 < x \leq 2.0$), where the excess negative charge arising from the substitution of Nb^{5+} with Ti^{4+} was compensated by A site substitution, was synthesised.[556,557] The Brønsted acidity, which was evaluated by the intercalation of organo-amines, of $HLa_2Nb_1Ti_2O_{10}$ ($x = 2$) was weak compared with $HCa_1La_1Nb_2Ti_1O_{10}$ ($x = 1$), indicating that Nb played an important role in the solid acidity of $HCa_2Nb_3O_{10}$. These results indicate the importance of the selection of heteroelements for the modification of the acidity of LTMOs.

Given that proton exchange of LTMOs with varying layer charge densities leads layered solid-acids with varying H^+ (Brønsted site) densities, the correlation of the layer charge density of LTMOs with their performances as solid-acid catalyst is of interest. $HCa_2Nb_3O_{10}$ with controlled amounts of acidic sites was obtained by the acid-treatment of $K_{1-x}Ca_{2-x}La_xNb_3O_{10}$ ($0 < x \leq 1.0$), whose interlayer cation amount was controlled by the substitution of Ca^{2+} with La^{3+}.[555] Because lower charge density leads to weaker electrostatic interactions between the layer and the interlayer cation, the correlation between the catalytic activity and reactant diffusion into the interlayer is also of interest. The layer charge density was controlled by the isomorphous substitution of a Ruddlesden–Popper layered perovskite, $A_2La_2Ti_3O_{10}$ (A = K or Rb).[556] The replacement of Ti^{4+} with Nb^{5+} resulted in $A_{2-x}La_2Ti_{3-x}Nb_xO_{10}$ (A = K, Rb) ($0 \leq x \leq 1.0$). In the range of

This journal is © The Royal Society of Chemistry 2024

Chem. Soc. Rev., 2024, **53**, 10523–10574 | **10559**

$0 \leq x \leq 0.75$, all the products were the Ruddlesden–Popper phase, while the Dion–Jacobson phase was obtained in the case of $x = 1.0$. The product with the Dion–Jacobson structure spontaneously hydrated under ambient conditions, which was related to the acidity of the products. Alternatively, $H_{2-x}La_2Ti_{3-x}Nb_xO_{10}$ ($0 \leq x \leq 0.75$) did not show hydration properties for all the x values, suggesting the importance of the crystal structure in addition to the composition[556,557] in the acidity of layered perovskites.

The solid-acidity of LTMO containing alkali metal cations in its interlayer space has been investigated. The lepidocrocite-type layered titanates $Cs_aTi_{2-x}h_xO_4$ ($a = 0.67$ or 0.70; h represents vacancy) and $Cs_aTi_{2-x}Zn_xO_4$ ($a = 0.70$) were demonstrated to exhibit Lewis acidity.[586,587] The layer structure of the lepidocrocite-type layered titanate whose interlayer alkali cation was replaced by a proton generally collapsed at $<400\ °C$.[528] Alternatively, these layered solid-acids with interlayer Cs maintained their structure at above $400\ °C$, which was beneficial for the ethanol conversion reaction at $380\ °C$. The acidity of $Cs_aTi_{2-x}h_xO_4$ ($a = 0.67$) treated at $400\ °C$, which was evaluated by NH_3-TPD, was higher than that of HZSM-5 treated in the same manner. The structure of the titanate layer and the incorporated Zn or vacancy in it, in addition to the interlayer cation, were related to the acidity.

5.3. Synthetic method for heteroelement-incorporated LTMOs

To incorporate heteroelements into LTMOs, solid-state synthesis has been used, where the source of the heteroelements is mixed in the starting mixture. Given that a homogeneous distribution of the heteroelement is required, the starting mixtures were carefully prepared. The starting materials were mixed for a long period (20 h) using a ball mill for synthesising the layered perovskite applicable to the dielectric application.[525,526] Although the mixing time and the instrument used for the mixing are important to achieve homogeneity of the components, the mixing time has been scarcely described.[525,526,588]

The starting mixture is often pelletised for an intimate connection between the components to facilitate the solid-state reaction. For applications that require a higher surface area such as photocatalysts, calcination in the powder form at a lower temperature is desirable for suppressing sintering,[589,590] where the possibility of an inhomogeneous distribution of components in the final products is plausible. Alternatively, the unconventionally low synthetic temperature is worth applying given that a new composition is likely to be found according to an undeveloped phase diagram. In the case of low-temperature synthesis, careful mixing of the starting materials will be beneficial for the better distribution of heteroelements in the products. The synthesis of lepidocrocite-type layered titanates $K_{0.8}Ti_{1.73}Li_{0.27}O_4$[589] and $KCa_2Nb_3O_{10}$[590] at a temperature lower than that reported previously[528,541,591] is applicable for isomorphous substitution, where the phase separation of the added heteroelements into by-products may be suppressed.

The atmosphere in the solid-state reaction is selected depending on the objective of isomorphous substitution. Although $K_{1-x}Ca_{2-x}La_xNb_3O_{10}$ ($0 < x \leq 1.0$) was obtained through solid-state reaction in air,[555] an inert atmosphere was applied for the synthesis of $KCa_{2-x}La_xNb_3O_{10}$ whose interlayer K^+ number per $Ca_2Nb_3O_{10}$ unit was fixed to 1.[554] This is because the excess positive charge arising from the isomorphous substitution was expected to be compensated by the reduction of Nb^{5+} for the desired electric properties.[554]
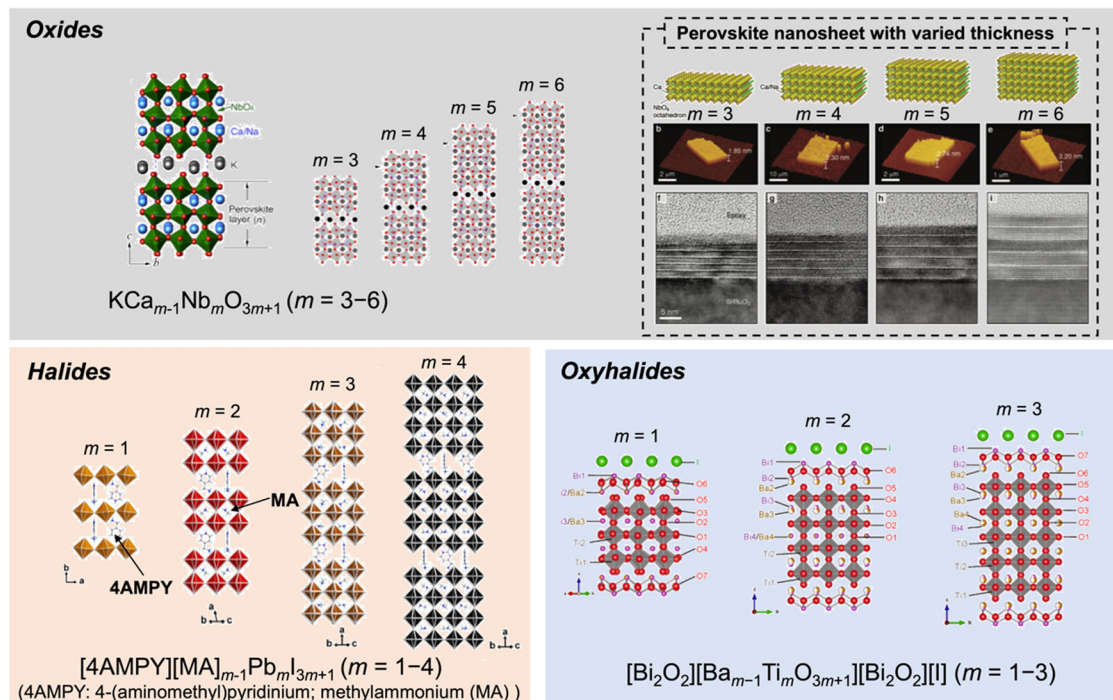

Fig. 34 Structural and compositional variation in perovskite-type layered compounds; oxides,[547,551] hallides[593] and oxyhalides.[594]

10560 | *Chem. Soc. Rev.*, 2024, **53**, 10523–10574

This journal is © The Royal Society of Chemistry 2024

Increasing attention has been directed to the design of layered perovskite-type compounds with more complicated composition/structures (Fig. 34). Regarding nanosheets derived from $KCa_{m-1}Nb_mO_{3m+1}$ (m = 3–6), it was found that the ferroelectric properties are correlated with the thickness of the perovskite layer.[547,592] Layered lead halide perovskites have attracted attention in versatile fields, including dye-sensitised solar cells, and Dion–Jacobson lead perovskite iodide with varying perovskite layer thicknesses.[593] It was demonstrated that the interlayer aromatic diammonium cations affected the structure and electric properties. Also, layered perovskite oxyhalides with a controlled layer thickness were reported, and iodide and three-layers were found to be the best among the tested samples for visible-light-induced photocatalytic water splitting.[594] Bulk perovskite oxides with more complicated compositions such as $LaMn_{0.2}Fe_{0.2}Co_{0.2}Ni_{0.2}Cu_{0.2}O_3$ were reported.[595] These results indicate that LTMOs with more complicated compositions and structures by means of carefully optimised synthetic conditions are likely to be a future intriguing topic.

5.4. Characterisation

The formation of LTMO with the desired composition is judged by confirming that all the reflections in its XRD pattern are assigned to the target product. The successful isomorphous substitution is confirmed by the changes in the lattice constant. An example of the correlation of the d value and x is shown in Fig. 35.[554] The products with heteroelements are sometimes accompanied with by-products and used in the target application although the by-products may affect the performance of the main product. Alternatively, the required amounts of the heteroelement were relatively low ($M_{HE}/M_{OE} \leq \sim 1/20$) in the development of visible-light absorption and luminescence properties,[521,522,565] making it difficult to confirm the formation of by-products by XRD. Even this small amount of impurity, which cannot be identified by XRD, will affect the materials properties. Successful doping can be confirmed by

observation using instruments such as high-resolution (HR) TEM, high-angle annular dark-field scanning transmission electron microscope (HAADF STEM) and EDS.

Besides characterisation in the solid-state, the characterisation of the dispersion of LTMOs in solvents and in polymers is worth examining. A periodic arrangement in the distance between the nanosheets in solvent or polymer matrices has been developed. Interests have been focused on the assembly of nanospheres (*e.g.*, nanoparticles and surfactant micelles) for developing structural colours inspired by nature, and LTMO-based nanosheets were demonstrated to orientate for developing structural colour.[596,597] An aqueous suspension of titanate
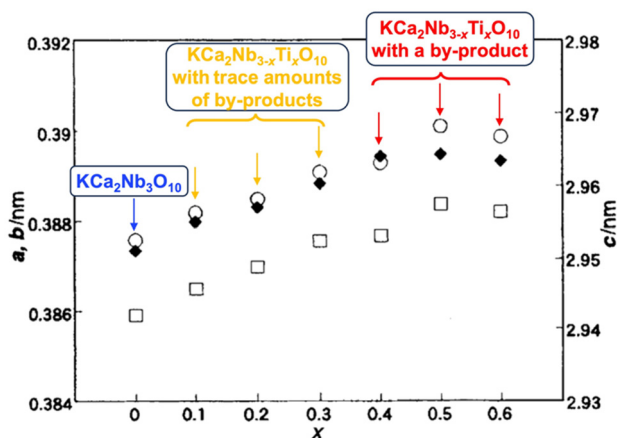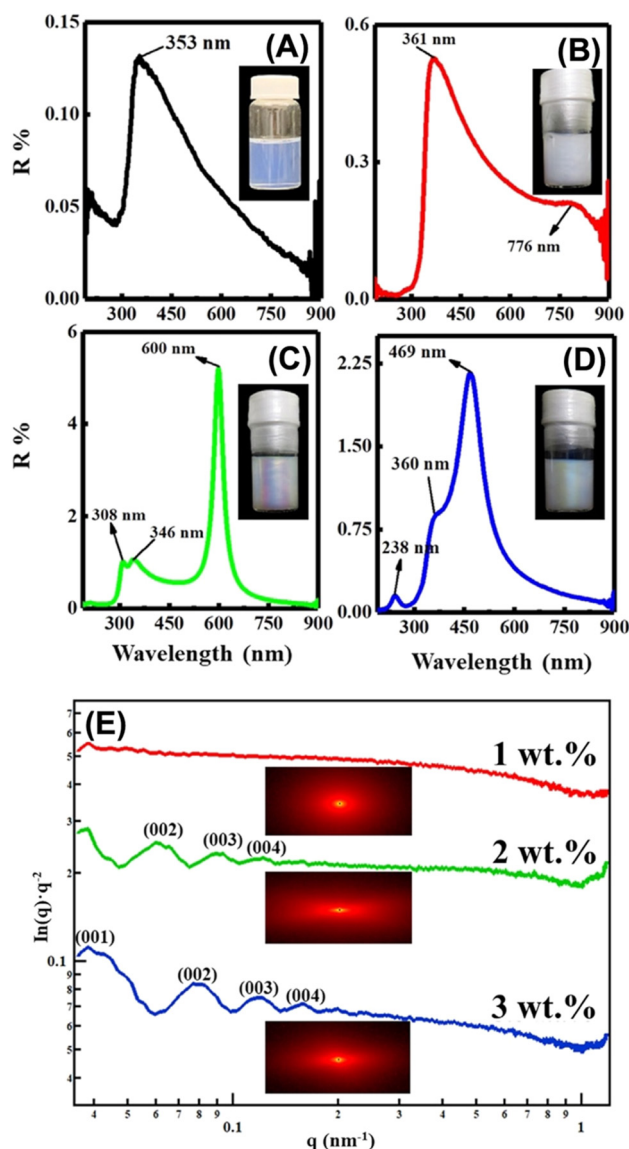

Fig. 36 Structural color of the liquid crystalline perovskite nanosheet suspension. (A)–(D) UV-Vis reflectance spectra and photographs of the colloids with the nanosheet concentration of (A) 0.1, (B) 1, (C) 2 and (D) 3 wt%. (E) Small-angle X-ray scattering and 2D patterns of the colloids with 1, 2 and 3 wt% of nanosheets. Reprinted from ref. 597. Copyright (2021), John Wiley & Sons.

Fig. 35 Variation in the lattice parameters of $KCa_2Nb_{3-x}Ti_xO_{10}$ by isomorphous substitution, where an increase in the lattice parameters of $KCa_2Nb_{3-x}Ti_xO_{10}$ are correlated with x, according to Vegard's law.[554]

This journal is © The Royal Society of Chemistry 2024

Chem. Soc. Rev., 2024, **53**, 10523–10574 | **10561**

nanosheet, which was obtained by the exfoliation of a lepidocrocite-type layered titanate, exhibited structural colour, depending on the concentration of the titanate nanosheet.[596] Also, the structural colour was controlled by external stimuli such as temperature, pH and magnetic field. The inter-nanosheet distances estimated by the UV-Vis spectra of the suspensions was in good agreement with that determined by SAXS. An aqueous colloidal suspension of perovskite nanosheets also demonstrated concentration-dependent structural colour, which was successfully explained by the variation in the inter-nanosheet distances estimated using UV-Vis spectroscopy and SAXS (Fig. 36).[597] The polymer hydrogel containing the perovskite nanosheets showed reversible mechanochromic responses, which are applicable to mechano-sensors and displays. The development of evaluation methods for understanding the characteristics of LTMO-based nanosheets will facilitate the design of novel LTMO-based materials.

5.5. Summary and perspectives

In addition to the common topics on the electric, electronic, magnetic, and optical properties of LTMOs by the incorporation of heteroelements, efforts to design surface properties, which are connected to hydration/swelling, adsorption, and catalysis, have been reported. The incorporation of heteroelements has been examined using a common ceramic process (solid-state reaction), where efforts have been made to homogenise the starting mixture by careful mechanical mixing and applying a sol–gel reaction. Post-synthetic treatments have also been examined for directing the lepidocrocite-type layered alkali titanate with varying layer charge densities, which is designed by the amount of heteroelement in the titanate sheet.[568,569] Conventional synthetic methods are worth revisiting to optimise the detailed conditions for each target function, which may extend the amount of heteroelements incorporated in LTMOs. For example, the synthesis of LTMOs by solid-state reactions at temperatures lower than the commonly reported ones[589,590] is a possible candidate.

Materials design that benefits from defects/vacancies, which are formed by the leaching of the heteroelement from the lepidocrocite-type titanate framework,[598] is also an intriguing topic. An anionic titanate nanosheet with Ti vacancy (sub-nanometric pore) let cations pass through selectively, benefitting from the electrostatic repulsion with anionic species, enabling its application as a coating material in a membrane separator for alkali metal batteries.[599] A metal-deficient titanate nanosheet was also demonstrated to be useful for electricity generation from water evaporation, where the density of vacancies was crucial for controlling the water-solid interactions that govern the material performance.[600] The important role of the Ti vacancy on the magnetic properties of lepidocrocite-type titanate was also pointed out.[601] The structural transformation of defective titanium oxide thin-layer into titanium oxide species including rutile,[584,585,602] brookite,[603,604] and Magneli phase[605] has been reported. Thus, the design of a titanate layer-TiO_2 heterojunction that is useful in electric/electronic applications is of interest.

6. Conclusion and future perspective

The partial replacement of one structural element in 2D oxides and hydroxides (nanosheets or layered materials) with hetero-elements was summarised with emphasis on the correlation of the basic chemistry of their preparation and characterisation with their application. Depending on the area of research, the phrase referring to the replacement varies (''isomorphous substitution'', ''doping'', *etc*). The application of the resulting materials includes adsorbents, catalysts, drug carriers, pigments, electrodes, and other advanced optical/magnetic/dielectric/semiconducting/superconducting materials. This concept (replacement of one structural element) has been extended to the partial replacement of two structural elements (two sites) in 2 : 1-type phyllosilicates and mixed oxides (including perovskite transition metal oxides), and the replacement of one structural element (one site) with multiple heteroelements, as seen in layered double hydroxides. Thus, the incorporation of multiple heteroelements is a way to further and more precisely modify the properties of these materials. The incorporation of multiple metal cations with unique oxidation states is thought to be chromophores of some gemstones (blue sapphire as a known example), which are fascinating examples in nature. Thus, it is necessary to prepare and characterise the materials with this compositional complexity more carefully and extensively. The important roles of vacancies have been pointed out, which will be examined further for their effects on the properties, interactions with the incorporated heteroelements, and as possible hosts to accommodate heteroelements.

The heteroelements to be incorporated and their amount have been selected objectively for each target function. Here, it should be noted that in some studies, the composition of the products was not determined experimentally, and the discussion on the properties was based on the starting composition. Thus, for the reliable discussion on the composition–property relationship, the appropriate characterisation to confirm the structural incorporation of the heteroelement is necessary. The recent development of the preparation[589,590] and modification of layered materials[547,606–608] will extend the elemental and compositional variation of heteroelements to tune the properties further. To extend the compositional variation (the heteroelement and the amount), there are two important factors, as follows: (1) crystallographic aspects and (2) synthetic methods. (1) The size of the ions for replacement (replacing elements and elements being replaced) is a factor based on structural aspects. (2) The availability and chemical reactivity of the starting materials containing the target heteroelements, and the synthetic conditions by which the main structures form without transformation or formation to/of other phases. The new and modified synthetic methods may lead to extended compositional variation (extended dopant concentration).

The hybridisation (or designing heterojunction) of 2D oxides/hydroxides[207,609–612] is a current topic in designing photo/electrocatalysts, adsorbents and other advanced functional materials. Therefore, the variation in 2D materials designed by the incorporation of heteroelements discussed herein will be

10562 | *Chem. Soc. Rev.*, 2024, **53**, 10523–10574

This journal is © The Royal Society of Chemistry 2024

useful for the extension of the combinations to design new/improved functions through the synergistic effects achieved by hybridisation.

Author contributions

The present work was written through the contributions of all authors. All authors have given approval to the final version of the review.

Data availability

All the data given in the present review article is based on the already published data as indicated in the text.

Conflicts of interest

There are no conflicts to declare.
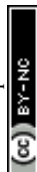
Acknowledgements

Notes and references

1 J. G. Bednorz and K. A. Muller, *ZPhys-e.B: Condens. Matter*, 1986, **64**, 189–193.
2 R. Hansen, *Gemstones: A Concise Reference Guide*, Princeton University Press, 2020.
3 G. W. Brindley and G. Brown, *Crystal Structure of Clay Minerals and their X-ray Identifications*, Miner. Soc., London, 1980.
4 J. E. Geusic, H. M. Marcos and L. G. Van Uitert, *Appl. Phys. Lett.*, 1964, **4**, 182–184.
5 A. A. Haider, H. Zhao, Y. Zi, Z. Xu, Y. Bai, Y. Cun, Y. Liu, H. Babeker, A. Saeed, Z. Song, J. Qiu, A. Huang, J. Liao and Z. Yang, *Adv. Opt. Mater.*, 2024, **12**, 2302265.
6 E. Snitzer, *Phys. Rev. Lett.*, 1961, **7**, 444–446.
7 R. M. Barrer, *Hydrothermal Chemistry of Zeolites*, Academic Press, London, 1982.
8 R. Szostak, *Molecular Sieves: Principles of Synthesis and Identification*, Blackie Academic and Profession, London, 1998.

9 M. Matsuoka and M. Anpo, *J. Photochem. Photobiol., C*, 2003, **3**, 225–252.
10 M. Anpo, *J. CO$_2$ Util.*, 2013, **1**, 8–17.
11 H. Yamashita, K. Mori, Y. Kuwahara, T. Kamegawa, M. Wen, P. Verma and M. Che, *Chem. Soc. Rev.*, 2018, **47**, 8072–8096.
12 H. Fei, J. Dong, D. Chen, T. Hu, X. Duan, I. Shakir, Y. Huang and X. Duan, *Chem. Soc. Rev.*, 2019, **48**, 5207–5241.
13 S. Kitagawa, R. Kitaura and S.-I. Noro, *Angew. Chem., Int. Ed.*, 2004, **43**, 2334–2375.
14 H. Furukawa, K. E. Cordova, M. Keeffe and O. M. Yaghi, *Science*, 2013, **341**, 974–986.
15 Q. Wang and D. Astruc, *Chem. Rev.*, 2019, **120**, 1438–1511.
16 J. Liu and C. Wöll, *Chem. Soc. Rev.*, 2017, **46**, 5730–5770.
17 M. Wen, K. Mori, Y. Kuwahara, T. An and H. Yamashita, *Chem. – Asian J.*, 2018, **13**, 1767–1779.
18 M. Woellner, S. Hausdorf, N. Klein, P. Mueller, M. W. Smith and S. Kaskel, *Adv. Mater.*, 2018, **30**, 1704679.
19 X. Zhao, Y. Wang, D.-S. Li, X. Bu and P. Feng, *Adv. Mater.*, 2018, **30**, 1705189.
20 K. Lu, T. Aung, N. Guo, R. Weichselbaum and W. Lin, *Adv. Mater.*, 2018, **30**, 1707634.
21 L. Chen and Q. Xu, *Matter*, 2019, **1**, 57–89.
22 T. Simon-Yarza, A. Mielcarek, P. Couvreur and C. Serre, *Adv. Mater.*, 2018, **30**, 1707365.
23 X. Yang and Q. Xu, *Cryst. Growth Des.*, 2017, **17**, 1450–1455.
24 A. D. Burrows, *CrystEngComm*, 2011, **13**, 3623–3642.
25 M. Y. Masoomi, A. Morsali, A. Dhakshinamoorthy and H. Garcia, *Angew. Chem., Int. Ed.*, 2019, **58**, 15188–15205.
26 L. Feng, K.-Y. Wang, G. S. Day and H.-C. Zhou, *Chem. Soc. Rev.*, 2019, **48**, 4823–4853.
27 Z. Liang, R. Zhao, T. Qiu, R. Zou and Q. Xu, *EnergyChem*, 2019, **1**, 100001.
28 H. Lin, Y. Xu, B. Wang, D.-S. Li, T. Zhou and J. Zhang, *Small Struct.*, 2022, **3**, 2100176.
29 H. Zhu, X. Gan, A. McCreary, R. Lv, Z. Lin and M. Terrones, *Nano Today*, 2020, **30**, 100829.
30 R. Kumar, S. Sahoo, E. Joanni, R. K. Singh, K. Maegawa, W. K. Tan, G. Kawamura, K. K. Kar and A. Matsuda, *Mater. Today*, 2020, **39**, 47–65.
31 Y. Zhou, X. Xu, B. Shan, Y. Wen, T. Jiang, J. Lu, S. Zhang, D. P. Wilkinson, J. Zhang and Y. Huang, *Energy Storage Mater.*, 2015, **1**, 103–111.
32 S. Ippolito, F. Urban, W. Zheng, O. Mazzarisi, C. Valentini, A. G. Kelly, S. M. Gali, M. Bonn, D. Beljonne, F. Corberi, J. N. Coleman, H. I. Wang and P. Samorì, *Adv. Mater.*, 2023, **35**, 2211157.
33 M. E. Leonowicz, J. A. Lawton, S. L. Lawton and M. K. Rubin, *Science*, 1994, **264**, 1910–1913.
34 M. Shamzhy, B. Gil, M. Opanasenko, W. J. Roth and J. Čejka, *ACS Catal.*, 2021, **11**, 2366–2396.
35 W. J. Roth and J. Čejka, *Catal. Sci. Technol.*, 2011, **1**, 43–53.
36 M. V. Opanasenko, W. J. Roth and J. Čejka, *Catal. Sci. Technol.*, 2016, **6**, 2467–2484.
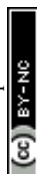37 M. Hmadeh, Z. Lu, Z. Liu, F. Gándara, H. Furukawa, S. Wan, V. Augustyn, R. Chang, L. Liao, F. Zhou, E. Perre,

This journal is © The Royal Society of Chemistry 2024

Chem. Soc. Rev., 2024, **53**, 10523–10574 | **10563**

V. Ozolins, K. Suenaga, X. Duan, B. Dunn, Y. Yamamoto, O. Terasaki and O. M. Yaghi, *Chem. Mater.*, 2012, **24**, 3511–3513.

38 M. Wang, R. Dong and X. Feng, *Chem. Soc. Rev.*, 2021, **50**, 2764–2793.

39 J.-M. Li, Q. C. Lin, N. Li, Z. H. Li, G. Tan, S. J. Liu, L. H. Chung, W. M. Liao, L. Yu and J. He, *Adv. Funct. Mater.*, 2023, **33**, 2210717.

40 G. Alberti and T. Bein, *Comprehensive Supramolecular Chemistry*, Pergamon, Oxford, 1996.

41 M. S. Whittingham and A. J. Jacobson, *Intercalation Chemistry*, Academic Press, New York, 1982.

42 W. Müller-Warmuth and R. Schöllhorn, *Progress in Intercalation Research*, Kluwer Academic, Dordrecht, 1994.

43 S. M. Auerbach, K. A. Carrado and P. K. Datta, *Handbook of Layered Materials*, Marcel Dekker, New York, 2004.

44 B. K. Momma and F. Izumi, *J. Appl. Crystallogr.*, 2011, **44**, 1272–1276.

45 V. Nicolosi, M. Chhowalla, M. G. Kanatzidis, M. S. Strano and J. N. Coleman, *Science*, 2013, **340**, 1226419.

46 V. Dudko, O. Khoruzhenko, S. Weiß, M. Daab, P. Loch, W. Schwieger and J. Breu, *Adv. Mater. Technol.*, 2023, **8**, 2200553.

47 J. L. Gunjakar, I. Y. Kim, J. M. Lee, Y. K. Jo and S. J. Hwang, *J. Phys. Chem. C*, 2014, **118**, 3847–3863.

48 W. T. Reichle, *Solid State Ionics*, 1986, **22**, 135–141.

49 D. G. Evans and R. C. T. Slade, in *Layered Double Hydroxides*, ed. X. Duan and D. G. Evans, Springer-Verlag, Berlin Heidelberg, 2005, vol. 119, pp. 1–87.

50 A. I. Khan and D. O'Hare, *J. Mater. Chem.*, 2002, **12**, 3191–3198.

51 V. Rives, *Layered Double Hydroxides: Present and Future*, Nova Science Publishers, New York, 2001.

52 H. Yi, S. Liu, C. Lai, G. Zeng, M. Li, X. Liu, B. Li, X. Huo, L. Qin, L. Li and M. Zhang, *Adv. Energy Mater.*, 2021, **11**, 2002863.

53 C. Taviot-Guého, V. Prévot, C. Forano, G. Renaudin, C. Mousty and F. Leroux, *Adv. Funct. Mater.*, 2018, **28**, 1703868.

54 R. Allmann, *Acta Crystallogr., Sect. B: Struct. Crystallogr. Cryst. Chem.*, 1968, **24**, 972–977.

55 D. Bish and G. Brindley, *Am. Mineral.*, 1977, **62**, 458–464.

56 E. S. Zhitova, N. V. Chukanov, I. V. Pekov, A. A. Zolotarev, V. V. Shilovskikh and V. N. Bocharov, *Appl. Clay Sci.*, 2023, **243**, 107070.

57 C. Frondel, *Am. Mineral.*, 1941, **26**, 295–315.

58 H. F. W. Taylor, *Mineral. Mag.*, 1973, **39**, 377–389.

59 H. F. W. Taylor, *Mineral. Mag.*, 1969, **37**, 338–342.

60 W. Feitknecht and M. Gerber, *Helv. Chim. Acta*, 1942, **25**, 131–137.

61 W. Feitknecht, *Helv. Chim. Acta*, 1942, **25**, 555–569.

62 A. C. Playle, S. R. Gunning and A. F. Llewellyn, *Pharm. Acta Helv.*, 1974, **49**, 298–302.

63 L. van der Ven, M. van Gemert, L. Batenburg, J. Keern, L. Gielgens, T. Koster and H. Fischer, *Appl. Clay Sci.*, 2000, **17**, 25–34.

64 T. Hibino, *Eur. J. Inorg. Chem.*, 2018, 722–730.

65 S. K. Jana, P. Wu and T. Tatsumi, *J. Catal.*, 2006, **240**, 268–274.

66 W. Ma, R. Ma, C. Wang, J. Liang, X. Liu, K. Zhou and T. Sasaki, *ACS Nano*, 2015, **9**, 1977–1984.

67 K. Ma, J. P. Cheng, M. Li, F. Liu and X. Zhang, *Electrochim. Acta*, 2016, **198**, 231–240.

68 A. C. Bouali, M. Serdechnova, C. Blawert, J. Tedim, M. G. S. Ferreira and M. L. Zheludkevich, *Appl. Mater. Today*, 2020, **21**, 100857.

69 V. A. Shirin, R. Sankar, A. P. Johnson, H. V. Gangadharappa and K. Pramod, *J. Controlled Release*, 2021, **330**, 398–426.

70 T. Hu, Z. Gu, G. R. Williams, M. Strimaite, J. Zha, Z. Zhou, X. Zhang, C. Tan and R. Liang, *Chem. Soc. Rev.*, 2022, **51**, 6126–6176.

71 T. Hibino and A. Tsunashima, *Chem. Mater.*, 1998, **10**, 4055–4061.

72 N. Dewangan, W. M. Hui, S. Jayaprakash, A. R. Bawah, A. J. Poerjoto, T. Jie, A. Jangam, K. Hidajat and S. Kawi, *Catal. Today*, 2020, **356**, 490–513.

73 J. Hong, C. Chen, A. Siriviriyanun, D. G. Crivoi, P. Holdway, J. C. Buffet and D. O'Hare, *RSC Adv.*, 2021, **11**, 27267–27275.

74 F. Cavani, F. Trifiro and A. Vaccari, *Catal. Today*, 1991, **11**, 173–301.

75 L. Yang, P. Yu, J. Liu, X. Li, H. Li, C. Liu, Y. Pan, B. Ye, B. Pan, C. Xiao and Y. Xie, *J. Phys. Chem. C*, 2023, **127**, 7172–7183.

76 L. Tan, Z. Wang, Y. Zhao and Y. F. Song, *Chem. – Asian J.*, 2020, **15**, 3380–3389.

77 J. An, T. Shen, W. Chang, Y. Zhao, B. Qi and Y. F. Song, *Inorg. Chem. Front.*, 2021, **8**, 996–1004.

78 Q. Xie, Z. Cai, P. Li, D. Zhou, Y. Bi, X. Xiong, E. Hu, Y. Li, Y. Kuang and X. Sun, *Nano Res.*, 2018, **11**, 4524–4534.

79 Y. Zhao, G. Chen, T. Bian, C. Zhou, G. I. Waterhouse, L. Z. Wu, C. H. Tung, L. J. Smith, D. O'Hare and T. Zhang, *Adv. Mater.*, 2015, **27**, 7824–7831.

80 P. S. Braterman, Z. P. Xu and F. Yarberry, in *Handbook of Layered Materials*, ed. S. M. Auerbach, K. A. Carrado and P. K. Dutta, Marcel Dekker, New York, 2004, pp. 373–474.

81 R. P. Wijitwongwan, S. G. Intasa-ard and M. Ogawa, *ChemEngineering*, 2019, **3**, 68.

82 G. S. Intasa-ard, S. Bureekaew and M. Ogawa, *J. Ceram. Soc. Jpn.*, 2019, **127**, 11–17.

83 G. S. Intasa-ard and M. Ogawa, *J. Solid State Chem.*, 2023, **317**, 123664.

84 G. S. Intasa-ard and M. Ogawa, *Appl. Clay Sci.*, 2022, **228**, 106615.

85 S. K. Yun and T. J. Pinnavaia, *Chem. Mater.*, 1995, **7**, 348–354.

86 N. Kobylinska, L. Puzyrnaya and G. Pshinko, *RSC Adv.*, 2022, **12**, 32156–32172.

87 Q. Xiao, Y. Yuan, J. Zhu, Z. Shi, Z. Li and J. Zhu, *J. Alloys Compd.*, 2022, **916**, 165391.

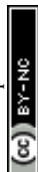88 J. Y. Lee, G. H. Gwak, H. M. Kim, T. I. Kim, G. J. Lee and J. M. Oh, *Appl. Clay Sci.*, 2016, **134**, 44–49.

10564 | *Chem. Soc. Rev.*, 2024, **53**, 10523–10574

This journal is © The Royal Society of Chemistry 2024
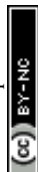
89   A. Seron and F. Delorme, *J. Phys. Chem. Solids*, 2008, **69**, 1088–1090.

90   S. Miyata, *Clays Clay Miner.*, 1983, **31**, 305–311.

91   J. W. Boclair and P. S. Braterman, *Chem. Mater.*, 1999, **11**, 298–302.

92   J. T. Kloprogge, L. Hickey and R. L. Frost, *J. Solid State Chem.*, 2004, **177**, 4047–4057.

93   Z. Gu, A. C. Thomas, Z. P. Xu, J. H. Campbell and G. Q. Lu, *Chem. Mater.*, 2008, **20**, 3715–3722.

94   U. Costantino, F. Marmottini, M. Nocchetti and R. Vivani, *Eur. J. Inorg. Chem.*, 1998, 1439–1446.

95   M. Ogawa and H. Kaiho, *Langmuir*, 2002, **18**, 4240–4242.

96   M. Adachi-Pagano, C. Forano and J. P. Besse, *J. Mater. Chem.*, 2003, **13**, 1988–1993.

97   M. Kayano and M. Ogawa, *Bull. Chem. Soc. Jpn.*, 2006, **79**, 1988–1990.

98   J. D. Yong, R. Valdez, M. Á. Armenta, N. Arjona, G. Pina-Luis and A. Olivas, *RSC Adv.*, 2022, **12**, 16955–16965.

99   L. B. Staal, S. S. C. Pushparaj, C. Forano, V. Prevot, D. B. Ravnsbæk, M. Bjerring and U. G. Nielsen, *J. Mater. Chem. A*, 2017, **5**, 21795–21806.

100   Z. Liu, R. Ma, M. Osada, N. Iyi, Y. Ebina, K. Takada and T. Sasaki, *J. Am. Chem. Soc.*, 2006, **128**, 4872–4880.

101   J. Qu, F. Li, M. Wang, S. Subakti, M. Deconinck, G. Chen, Y. Li, L. Liu, X. Wang, M. Yu and D. Wolf, *Adv. Mater. Interfaces*, 2022, **9**, 2200973.

102   F. Geng, Y. Matsushita, R. Ma, H. Xin, M. Tanaka, F. Izumi, N. Iyi and T. Sasaki, *J. Am. Chem. Soc.*, 2008, **130**, 16344–16350.

103   J. Zhao, X. R. Wang, F. W. Chen, C. He, X. J. Wang, Y. P. Li, R. H. Liu, X. M. Chen, Y. J. Hao, M. Yang and F. T. Li, *Inorg. Chem. Front.*, 2020, **7**, 737–745.

104   S. P. Newman, W. Jones, P. O'Connor and D. N. Dtamires, *J. Mater. Chem.*, 2002, **12**, 153–155.

105   M. Ogawa and S. Asai, *Chem. Mater.*, 2000, **12**, 3253–3255.

106   S. G. Intasa-ard, K. J. Imwiset, S. Bureekaew and M. Ogawa, *Dalton Trans.*, 2018, **47**, 2896–2916.

107   K. R. Poeppelmeier and S. J. Hwu, *Inorg. Chem.*, 1987, **26**, 3297–3302.

108   A. N. Ay, B. Zümreoglu-Karan and L. Mafra, *Anorg. Allg. Chem.*, 2009, **635**, 1470–1475.

109   Z. Ferencz, M. Szabados, M. Ádok-Sipiczki, Á. Kukovecz, Z. Kónya, P. Sipos and I. Pálinkó, *J. Mater. Sci.*, 2014, **49**, 8478–8486.

110   E. Conterosito, W. V. Beek, L. Palin, G. Croce, L. Perioli, D. Viterbo, G. Gatti and M. Milanesio, *Cryst. Growth Des.*, 2013, **13**, 1162–1169.

111   K. Kuramoto, S. G. Intasa-ard, S. Bureekaew and M. Ogawa, *J. Solid State Chem.*, 2017, **253**, 147–153.

112   K. Kuramoto and M. Ogawa, *Bull. Chem. Soc. Jpn.*, 2011, **84**, 675–677.

113   E. Conterosito, V. Gianotti, L. Palin, E. Boccaleri, D. Viterbo and M. Milanesio, *Inorg. Chim. Acta*, 2018, **470**, 36–50.

114   M. W. Louie and A. T. Bell, *J. Am. Chem. Soc.*, 2013, **135**, 12329–12337.

115   X. Long, S. Xiao, Z. Wang, X. Zheng and S. Yang, *Chem. Commun.*, 2015, **51**, 1120–1123.

116   L. Jin, X. Zhou, F. Wang, X. Ning, Y. Wen, B. Song, C. Yang, D. Wu, X. Ke and L. Peng, *Nat. Commun.*, 2022, **13**, 6093.

117   U. G. Nielsen, *Annual Reports on NMR Spectroscopy*, 2021, vol. 104, pp. 75–140.

118   S. Miyata, *Clays Clay Miner.*, 1980, **28**, 50–56.

119   V. P. Khusnutdinov and V. P. Isupov, *Inorg. Mater.*, 2008, **44**, 263–267.

120   E. López-Salinas, M. Garcia-Sanchez, J. A. Montoya, D. R. Acosta, J. A. Abasolo and I. Schifter, *Langmuir*, 1997, **13**, 4748–4753.

121   E. Lopez-Salinas, M. García-Sánchez, M. L. Ramón-García and I. Schifter, *J. Porous Mater.*, 1996, **3**, 169–174.

122   G. A. Caravaggio, C. Detellier and Z. Wronski, *J. Mater. Chem.*, 2001, **11**, 912–921.

123   F. Touahra, M. Sehailia, W. Ketir, K. Bachari, R. Chebout, M. Trari, O. Cherifi and D. Halliche, *Appl. Petrochem. Res.*, 2016, **6**, 1–13.

124   R. Ma, J. Liang, X. Liu and T. Sasaki, *J. Am. Chem. Soc.*, 2012, **134**, 19915–19921.

125   R. Ma, J. Liang, K. Takada and T. Sasaki, *J. Am. Chem. Soc.*, 2011, **133**, 613–620.

126   J. L. Milagres, C. R. Bellato, R. S. Vieira, S. O. Ferreira and C. Reis, *J. Environ. Chem. Eng.*, 2017, **5**, 5469–5480.

127   M. Sipiczki, E. Kuzmann, Z. Homonnay, J. Megyeri, I. Pálinkó and P. Sipos, *J. Mol. Struct.*, 2013, **1044**, 116–120.

128   J. Y. Lee, G. H. Gwak, H. M. Kim, T. I. Kim, G. J. Lee and J. M. Oh, *Appl. Clay Sci.*, 2016, **134**, 44–49.

129   R. D. Shannon, *Acta Crystallogr.*, 1976, **A32**, 751–767.

130   R. Wijitwongwan, S. Intasa-ard and M. Ogawa, *Nanomater.*, 2021, **11**, 1206.

131   R. Prihod'ko, M. Sychev, I. Kolomitsyn, P. J. Stobbelaar, E. J. Hensen and R. A. van Santen, *Microporous Mesoporous Mater.*, 2002, **56**, 241–255.

132   M. Bellotto, B. Rebours, O. Clause, J. Lynch, D. Bazin and E. Elkaïm, *J. Phys. Chem.*, 1996, **100**, 8527–8534.

133   E. López-Salinas, M. Garcia-Sanchez, J. A. Montoya, D. R. Acosta, J. A. Abasolo and I. Schifter, *Langmuir*, 1997, **13**, 4748–4753.

134   R. P. Wijitwongwan, T. K. Saothayanun and M. Ogawa, *Dalton Trans.*, 2023, **52**, 4692–4699.

135   C. Carteret, B. Grégoire and C. Ruby, *Solid State Sci.*, 2011, **13**, 146–150.

136   X. Long, S. Xiao, Z. Wang, X. Zheng and S. Yang, *Chem. Commun.*, 2015, **51**, 1120–1123.

137   S. Moolayadukkam, S. Thomas, R. C. Sahoo, C. H. Lee, S. U. Lee and H. R. Matte, *ACS Appl. Mater. Interfaces*, 2020, **12**, 6193–6204.

138   X. Zhao, X. Zhao, I. Ullah, L. Gao, J. Zhang and J. Lu, *Catal. Lett.*, 2021, **151**, 1683–1692.

139   J. Sun, Y. Li, C. Chen, T. Qi, D. Xia, W. Mao, T. Yang, L. Chen, W. Shen and S. Tang, *Talanta*, 2018, **187**, 265–271.

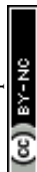140   M. Wilhelm, A. Bastos, C. Neves, R. Martins and J. Tedim, *Mater. Des.*, 2021, **212**, 110188.

This journal is © The Royal Society of Chemistry 2024

Chem. Soc. Rev., 2024, **53**, 10523–10574 | **10565**

141 G. Abellan, E. Coronado, C. Marti-Gastaldo, J. Waerenborgh and A. Ribera, *Inorg. Chem.*, 2013, **52**, 10147–10157.

142 A. Mantilla, G. Jácome-Acatitla, G. Morales-Mendoza, F. Tzompantzi and R. Gómez, *Ind. Eng. Chem. Res.*, 2011, **50**, 2762–2767.

143 D. Kang, X. Yu, S. Tong, M. Ge, J. Zuo, C. Cao and W. Song, *Chem. Eng. J.*, 2013, **228**, 731–740.

144 R. P. Wijitwongwan and M. Ogawa, *Langmuir*, 2024, **40**, 1408–1417.

145 G. Li, X. Zhang, D. Qiu, Z. Liu, C. Yang, C. B. Cockreham, B. Wang, L. Fu, J. Zhang, B. Sudduth and X. Guo, *Adv. Electron. Mater.*, 2019, **5**, 1900215.

146 X. Wang, R. Cao, S. Zhang, P. Hou, R. Han, M. Shao and X. Xu, *J. Mater. Chem. A*, 2017, **5**, 23999–24010.

147 M. Ogawa and Y. Sugiyama, *J. Ceram. Soc. Jpn.*, 2009, **117**, 179–184.

148 V. Isupov, L. Chupakhina and R. Mitrofanova, *J. Mater. Synth. Process.*, 2000, **8**, 251–253.

149 R. Ma, Z. Liu, K. Takada, N. Iyi, Y. Bando and T. Sasaki, *J. Am. Chem. Soc.*, 2007, **129**, 5257–5263.

150 R. Ma, K. Takada, K. Fukuda, N. Iyi, Y. Bando and T. Sasaki, *Angew. Chem., Int. Ed.*, 2008, **47**, 86–89.

151 J. Liang, R. Ma, N. Iyi, Y. Ebina, K. Takada and T. Sasaki, *Chem. Mater.*, 2010, **22**, 371–378.

152 H. C. Noltimier and P. A. Colinvaux, *Nature*, 1976, **259**, 197–200.

153 R. M. Taylor, *Clay Miner.*, 1984, **19**, 591–603.

154 R. Tahawy, E. Doustkhah, E. A. Abdel-Aal, M. Esmat, F. E. Farghaly, H. El-Hosainy, N. Tsunoji, F. I. El-Hosiny, Y. Yamauchi, M. H. N. Assadi and Y. Ide, *Appl. Catal., B*, 2021, **286**, 119854.

155 S. Tezuka, R. Chitrakar, A. Sonoda, K. Ooi and T. Tomida, *Green Chem.*, 2004, **6**, 104–109.

156 Y. Lin, Q. Fang and B. Chen, *J. Environ. Sci.*, 2014, **26**, 493–501.

157 M. Sui, Y. Zhou, L. Sheng and B. Duan, *Chem. Eng. J.*, 2012, **210**, 451–460.

158 T. Kameda, M. Honda and T. Yoshioka, *Sep. Purif. Technol.*, 2011, **80**, 235–239.

159 D. Wan, H. Liu, R. Liu, J. Qu, S. Li and J. Zhang, *Chem. Eng. J.*, 2012, **195**, 241–247.

160 M. Chen, F. Wu, L. Yu, Y. Cai, H. Chen and M. Zhang, *CrystEngComm*, 2019, **21**, 6790–6800.

161 X. Yang, M. T. Rahman, T. Kameda, Y. Masaki, Y. Saito, S. Kumagai and T. Yoshioka, *Mine Water Environ.*, 2020, **39**, 881–887.

162 F. Kooli, I. C. Chisem, M. Vucelic and W. Jones, *Chem. Mater.*, 1996, **8**, 1969–1977.

163 P. Z. Xu and Q. G. Lu, *Chem. Mater.*, 2005, **17**, 1055–1062.

164 D. Tichit, A. Rolland, F. Prinetto, G. Fetter, M. De Jesus Martinez-Ortiz, M. A. Valenzuela and P. Bosch, *J. Mater. Chem.*, 2002, **12**, 3832–3838.

165 L. N. Puzyrnaya, G. N. Pshinko, V. Y. Zub and O. V. Zuy, *Bull. Mater. Sci.*, 2020, **43**, 3.

166 K. Morimoto, K. Tamura, H. Yamada, T. Sato and M. Suzuki, *Appl. Clay Sci.*, 2016, **121**, 71–76.

167 Y. Lwin, M. A. Yarmo, Z. Yaakob, A. B. Mohamad and W. R. W. Daud, *Mater. Res. Bull.*, 2001, **36**, 193–198.

168 X. Wang, R. Cao, S. Zhang, P. Hou, R. Han, M. Shao and X. Xu, *J. Mater. Chem. A*, 2017, **5**, 23999–24010.

169 G. Fan, F. Li, D. G. Evans and X. Duan, *Chem. Soc. Rev.*, 2014, **43**, 7040–7066.

170 M. Chen, R. Zhu, X. Lu, J. Zhu and H. He, *Inorg. Chem.*, 2018, **57**, 7299–7313.

171 S. Mandal, S. Natarajan, S. Raja, N. Vijayalakshmi, C. Muralidharan and A. B. Mandal, *Key Eng. Mater.*, 2013, **571**, 57–69.

172 D. Wan, H. Liu, R. Liu, J. Qu, S. Li and J. Zhang, *Chem. Eng. J.*, 2012, **195**, 241–247.

173 D. Wan, Y. Liu, S. Xiao, J. Chen and J. Zhang, *Colloids Surf., A*, 2015, **469**, 307–314.

174 D. G. Cantrell, L. J. Gillie, A. F. Lee and K. Wilson, *Appl. Catal., A*, 2005, **287**, 183–190.

175 V. K. Diez, C. R. Apesteguia and J. I. Di Cosimo, *J. Catal.*, 2003, **215**, 220–223.

176 V. L. Constantino and T. J. Pinnavaia, *Inorg. Chem.*, 1995, **34**, 883–892.

177 D. G. Cantrell, L. J. Gillie, A. F. Lee and K. Wilson, *Appl. Catal.*, 2005, **287**, 183–190.

178 H. S. Chavan, C. H. Lee, A. I. Inamdar, J. Han, S. Park, S. Cho, N. K. Shrestha, S. U. Lee, B. Hou, H. Im and H. Kim, *ACS Catal.*, 2022, **12**, 3821–3831.

179 W. Jiang, A. Y. Faid, B. F. Gomes, I. Galkina, L. Xia, C. M. S. Lobo, M. Desmau, P. Borowski, H. Hartmann, A. Maljusch and A. Besmehn, *Adv. Funct. Mater.*, 2022, **32**, 2203520.

180 S. Lee, L. Bai and X. Hu, *Angew. Chem.*, 2020, **132**, 8149–8154.

181 H. Zhang, D. Pan, K. Zou, J. He and X. Duan, *J. Mater. Chem.*, 2009, **19**, 3069–3077.

182 M. Del Arco, S. Gutierrez, C. Martí, V. Rives and J. Rocha, *J. Solid State Chem.*, 2000, **151**, 272–280.

183 L. X. Zhang, J. Hu, Y. B. Jia, R. T. Liu, T. Cai and Z. P. Xu, *Nanoscale*, 2021, **13**, 7533–7549.

184 G. Su, H. Zhou, Q. Mu, Y. Zhang, L. Li, P. Jiao, G. Jiang and B. Yan, *J. Phys. Chem. C*, 2012, **116**, 4993–4998.

185 J. M. Oh, S. J. Choi, S. T. Kim and J. H. Choy, *Bioconjugate Chem.*, 2006, **17**, 1411–1417.

186 J. M. Oh, S. J. Choi, G. E. Lee, J. E. Kim and J. H. Choy, *Chem. – Asian J.*, 2009, **4**, 67–73.

187 T. Yamaguchi, H. M. Kim, B. C. Jung, Y. S. Kim and J. M. Oh, *Appl. Clay Sci.*, 2022, **225**, 106549.

188 A. W. Musumeci, T. L. Schiller, Z. P. Xu, R. F. Minchin, D. J. Martin and S. V. Smith, *J. Phys. Chem. C*, 2010, **114**, 734–740.

189 H. J. Kim, J. Y. Lee, T. H. Kim, G. H. Gwak, J. H. Park and J. M. Oh, *Appl. Clay Sci.*, 2020, **186**, 105454.

190 M. S. Usman, M. Z. Hussein, A. U. Kura, S. Fakurazi, M. J. Masarudin and F. F. A. Saad, *Mater. Chem. Phys.*, 2020, **240**, 122232.

191 T. H. Kim, J. Y. Lee, M. K. Kim, J. H. Park and J. M. Oh, *RSC Adv.*, 2016, **6**, 48415–48419.

10566 | *Chem. Soc. Rev.*, 2024, **53**, 10523–10574

This journal is © The Royal Society of Chemistry 2024

192 D. G. Jeung, T. H. Kim and J. M. Oh, *Nanomater.*, 2021, **11**, 44.

193 S. Mansingh, D. P. Sahoo, L. Paramanik, M. Sahoo and K. Parida, *Inorg. Chem. Front.*, 2022, **9**, 559–576.

194 J. Zhang, J. Liu, L. Xi, Y. Yu, N. Chen, S. Sun, W. Wang, K. M. Lange and B. Zhang, *J. Am. Chem. Soc.*, 2018, **140**, 3876–3879.

195 Y. Hu, G. Luo, L. Wang, X. Liu, Y. Qu, Y. Zhou, F. Zhou, Z. Li, Y. Li, T. Yao, C. Xiong, B. Yang, Z. Yu and Y. Wu, *Adv. Energy Mater.*, 2021, **11**, 2002816.

196 P. Li, M. Wang, X. Duan, L. Zheng, X. Cheng, Y. Zhan, Y. Kuang, Y. Li, Q. Ma, Z. Feng, W. Liu and X. Sun, *Nat. Commun.*, 2019, **10**, 1711.

197 B. Zhang, C. Zhu, Z. Wu, E. Stavitski, Y. H. Lui, T.-H. Kim, H. Liu, L. Huang, X. Luan, L. Zhou, K. Jiang, W. Huang, S. Hu, H. Wang and J. S. Francisco, *Nano Lett.*, 2020, **20**, 136–144.

198 X. Meng, J. Han, L. Lu, G. Qiu, Z. L. Wang and C. Sun, *Small*, 2019, **15**, 1902551.

199 Z. Cai, D. Zhou, M. Wang, S.-M. Bak, Y. Wu, Z. Wu, Y. Tian, X. Xiong, Y. Li, W. Liu, S. Siahrostami, Y. Kuang, X.-Q. Yang, H. Duan, Z. Feng, H. Wang and X. Sun, *Angew. Chem., Int. Ed.*, 2018, **130**, 9536–9540.

200 Q. Li, G. Liu, Z. Wu, X. Sun, W. Chen and Y. F. Song, *Chem. Eng. J.*, 2024, **2024**, 154029.

201 L. Wang, Z. Xiang, H. Zhang, Y. Deng, J. Wang, H. Xiao, W. Wang and X. Song, *New J. Chem.*, 2024, **48**, 5681–5695.

202 P. Li, X. Duan, Y. Kuang, Y. Li, G. Zhang, W. Liu and X. Sun, *Adv. Energy Mater.*, 2018, **8**, 1703341.

203 Y. Guo, Z. Zhu, Y. Qiu and J. Zhao, *J. Hazard. Mater.*, 2012, **15**, 239–240.

204 H. Jun, Z. Zhiliang, L. Hongtao and Q. Yanling, *RSC Adv.*, 2014, **4**, 5156–5164.

205 E. M. Seftel, J. Spooren, M. Kun, P. Cool and B. Michielsen, *J. Environ. Chem. Eng.*, 2024, **12**, 112196.

206 B. R. Gevers, E. Roduner, A. Leuteritz and F. J. W. J. Labuschagné, *Nanoscale*, 2024, **16**, 6449–6454.

207 R. P. Wijitwongwan, S. G. Intasa-ard and M. Ogawa, *Dalton Trans.*, 2024, **53**, 6144–6156.

208 M. Nogami, Y. Abe, K. Hirao and D. H. Cho, *Appl. Phys. Lett.*, 1995, **66**, 2952–2954.

209 M. Nogami, X. H. Le and X. Q. Vu, *J. Non-Cryst. Solids*, 2019, **503–504**, 260–267.

210 A. Tuel, *Microporous Mesoporous Mater.*, 1999, **27**, 151–169.

211 G. Lagaly, *Adv. Colloid Interface Sci.*, 1979, **11**, 105–148.

212 T. Selvam, A. Inayat and W. Schwieger, *Dalton Trans.*, 2014, **43**, 10365–10387.

213 B. Marler, I. Grosskreuz and H. Gies, *J. Solid State Chem.*, 2021, **300**, 122215.

214 Y. Krysiak, M. Maslyk, B. N. Silva, S. Plana-Ruiz, H. M. Moura, E. O. Munsignatti, V. S. Vaiss, U. Kolb, W. Tremel, L. Palatinus, A. A. Leitão, B. Marler and H. O. Pastore, *Chem. Mater.*, 2021, **33**, 3207–3219.

215 S. Vortmann, J. Rius, S. Siegmann and H. Gies, *J. Phys. Chem. B*, 1997, **101**, 1292–1297.

216 S. Vortmann, J. Rius, B. Marler and H. Gies, *Eur. J. Mineral.*, 1999, **11**, 125–134.

217 T. Ikeda, Y. Oumi, K. Honda, T. Sano, K. Momma and F. Izumi, *Inorg. Chem.*, 2011, **50**, 2294–2301.

218 H. P. Eugster, *Science*, 1967, **157**, 1177–1180.

219 K. Kosuge, A. Yamazaki, A. Tsunashima and R. Otsuka, *J. Ceram. Soc. Jpn.*, 1992, **100**, 326–331.

220 K. Beneke and G. Lagaly, *Am. Mineral.*, 1983, **68**, 818–826.

221 K. Endo, Y. Sugahara and K. Kuroda, *Bull. Chem. Soc. Jpn.*, 1994, **67**, 3352–3355.

222 T. G. Dos Santos, G. C. De Assis, A. O. S. Da Silva and S. M. P. Meneghetti, *ACS Appl. Mater. Interfaces*, 2023, **15**, 43234–43250.

223 G. Pal-Borberly and A. Auroux, *Stud. Surf. Sci. Catal.*, 1995, **94**, 55–62.

224 G. B. Superti, E. C. Oliveira, H. O. Pastore, A. Bordo, C. Bisio and L. Marchese, *Chem. Mater.*, 2007, **19**, 4300–4315.

225 W. Supronowicz, F. Roessner, W. Schwieger, M. Meilikhov and D. Eskenm, *Clays Clay Miner.*, 2012, **60**, 254–264.

226 Y. Bi, J. Blanchard, J. F. Lambert, Y. Millot, S. Casale, S. Zeng, H. Nie and D. Li, *Appl. Clay Sci.*, 2012, **57**, 71–78.

227 M. E. R. Oliveira, E. C. da Silva Filho, J. M. Filho, S. S. Ferreira, A. C. Oliveira and A. F. Campos, *Chem. Eng. J.*, 2015, **263**, 257–267.

228 G. L. Paz, E. C. O. Munsignatti and H. O. Pastore, *J. Mol. Catal. A: Chem.*, 2016, **422**, 43–50.

229 R. K. S. Almeida, G. L. Paz, G. B. Báfero and H. O. Pastore, *Microporous Mesoporous Mater.*, 2019, **284**, 1–9.

230 T. G. Santos, A. O. S. Silva and S. M. P. Meneghetti, *Appl. Clay Sci.*, 2019, **183**, 105293.

231 G. B. Báfero, B. N. N. Silva, A. A. Leitão and H. O. Pastore, *Mol. Catal.*, 2023, **535**, 112870.

232 S. Inagaki, Y. Yamada and Y. Fukushima, *Stud. Surf. Sci. Catal.*, 1997, **105**, 109–116.

233 Q. Kan, V. Fornés, F. Rey and A. Corma, *J. Mater. Chem.*, 2000, **10**, 993–1000.

234 T. Shigeno, K. Inoue, T. Kimura, N. Katada, M. Niwa and K. Kuroda, *J. Mater. Chem.*, 2003, **13**, 883–887.

235 T. Kimura, M. Suzuki, T. Ikeda, K. Kato, M. Maeda and S. Tomura, *Microporous Mesoporous Mater.*, 2006, **95**, 146–153.

236 G. Pal-Borberly, H. Beyer, Y. Kiyozumi and F. Mizukami, *Microporous Mesoporous Mater.*, 1998, **22**, 57–68.

237 E. M. Barea, V. Fornés, A. Corma, P. Bourges, E. Guillon and V. F. Puntes, *Chem. Commun.*, 2004, 1974–1975.

238 S. Neatu, M. Puche, V. Fornes and H. Garcia, *Chem. Commun.*, 2014, **50**, 14643–14646.

239 F. S. O. Ramos and H. O. Pastore, *Dalton Trans.*, 2017, **46**, 11728–11737.

240 M. D. Alba, P. Chain and E. Pavon, *Microporous Mesoporous Mater.*, 2006, **94**, 66–73.

241 W. Schwieger and E. Brunner, *Colloid Polym. Sci.*, 1992, **270**, 935–938.

242 W. Schwieger, K. Pohl, U. Brenn, C. A. Fyfe, H. Grondey, G. Fu and G. T. Kokotailo, *Stud. Surf. Sci. Catal.*, 1995, **94**, 47–54.
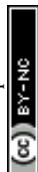
This journal is © The Royal Society of Chemistry 2024

Chem. Soc. Rev., 2024, **53**, 10523–10574 | **10567**

243 C. A. Fyfe, J. Skibsted and W. Schwieger, *Inorg. Chem.*, 2001, **40**, 5906–5912.

244 H. M. Moura, F. A. Bonk, R. C. G. Vinhas, R. Landers and H. O. Pastore, *CrystEngComm*, 2011, **13**, 5428–5438.

245 M. Morita, Y. Horiuchi, M. Matsuoka and M. Ogawa, *Cryst. Growth Des.*, 2022, **22**, 1638–1644.

246 W. Supronowicz and F. Roessner, *Clays Clay Miner.*, 2011, **59**, 95–105.

247 Q. Sun, X. Guo, B. Guo, Q. Tang, W. Yu, Q. Wan and Y. An, *Appl. Clay Sci.*, 2023, **231**, 106745.

248 C. T. G. V. M. T. Pires, J. R. Costa and C. Airoldi, *Microporous Mesoporous Mater.*, 2012, **163**, 1–10.

249 N. Takahashi and K. Kuroda, *J. Mater. Chem.*, 2011, **21**, 14336–14353.

250 W. J. Roth, P. Nachtigall, R. E. Morris and J. Čejka, *Chem. Rev.*, 2014, **114**, 4807–4837.

251 M. Koike, I. Grosskreuz, Y. Asakura, R. Miyawaki, H. Gies, H. Wada, A. Shimojima, B. Marler and K. Kuroda, *Chem. – Eur. J.*, 2023, e202301942.

252 S. Zanardi, A. Alberti, G. Cruciani, A. Corma, V. Fornés and M. Brunelli, *Angew. Chem., Int. Ed.*, 2004, **43**, 4933–4937.

253 T. Ikeda, Y. Akiyama, Y. Oumi, A. Kawai and F. Mizukami, *Angew. Chem., Int. Ed.*, 2004, **43**, 4892–4896.

254 B. Marler, N. Ströter and H. Gies, *Microporous Mesoporous Mater.*, 2005, **83**, 201–211.

255 Y. X. Wang, H. Gies, B. Marler and U. Müller, *Chem. Mater.*, 2005, **17**, 43–49.

256 Y. Ide, S. Tominaka, H. Kono, R. Ram, A. Machida and N. Tsunoji, *Chem. Sci.*, 2018, **9**, 8637–8643.

257 G. Lagaly, K. Beneke and A. Weiss, *Am. Mineral.*, 1975, **60**, 642–649.

258 G. Lagaly, K. Beneke and A. Weiss, *Am. Mineral.*, 1975, **60**, 650–658.

259 G. Lagaly, *Solid State Ionics*, 1986, **22**, 43–51.

260 M. Ogawa, K. Saito and M. Sohmiya, *Dalton Trans.*, 2014, **43**, 10340–10354.

261 C. Tirayaphanitchkul, K. Imwiset and M. Ogawa, *Bull. Chem. Soc. Jpn.*, 2021, **94**, 678–693.

262 E. Doustkhah and Y. Ide, *New J. Chem.*, 2020, **44**, 9957–9968.

263 N. Tsunoji, T. Ikeda, Y. Ide, M. Sadakane and T. Sano, *J. Mater. Chem.*, 2012, **22**, 13682–13690.

264 N. Tsunoji, M. Fukuda, K. Yoshida, Y. Sasaki, T. Ikeda, Y. Ide, M. Sadakane and T. Sano, *J. Mater. Chem. A*, 2013, **1**, 9680–9688.

265 G. J. Ray, B. L. Meyers and C. L. Marshall, *Zeolites*, 1987, **7**, 307–310.

266 C. A. Fyfe, G. C. Gobbi, W. J. Murphy, R. S. Ozubko and D. A. Slack, *Chem. Lett.*, 1983, 1547–1550.

267 B. Notari, *Adv. Catal.*, 1996, **41**, 253–334.

268 C. Perego, A. Carati, P. Ingallina, M. A. Mantegazza and G. Bellussi, *Appl. Catal., A*, 2001, **221**, 63–72.

269 P. T. Tanev, M. Chibwe and T. J. Pinnavaia, *Nature*, 1994, **368**, 321–323.

270 A. Corma, M. T. Navarro and J. P. Pariente, *J. Chem. Soc., Chem. Commun.*, 1994, 147–148.

271 K. Koyano and T. Tatsumi, *Chem. Commun.*, 1996, 145–146.

272 W. Zhang, M. Fröba, J. Wang, P. T. Tanev, J. Wong and T. J. Pinnavaia, *J. Am. Chem. Soc.*, 1996, **118**, 9164–9171.

273 M. Ogawa, K. Ikeue and M. Anpo, *Chem. Mater.*, 2001, **13**, 2900–2904.

274 K. J. Imwiset and M. Ogawa, *Inorg. Chem.*, 2021, **60**, 9563–9570.

275 T. Yamaguchi, K. J. Imwiset, M. G. Choi, J. M. Oh, S. Y. Lee and M. Ogawa, *Appl. Clay Sci.*, 2023, **236**, 106882.

276 E. Ruiz-Hitzky and J. M. Rojo, *Nature*, 1980, **287**, 28–30.

277 E. Ruiz-Hitzky, J. M. Rojo and G. Lagaly, *Colloid Polym. Sci.*, 1985, **263**, 1025–1030.

278 M. Ogawa, S. Okutomo and K. Kuroda, *J. Am. Chem. Soc.*, 1998, **120**, 7361–7362.

279 Y. Ide and M. Ogawa, *Bull. Chem. Soc. Jpn.*, 2007, **80**, 1624–1629.

280 E. Ruiz-Hitzky, P. Aranda, M. Darder and M. Ogawa, *Chem. Soc. Rev.*, 2011, **40**, 801–828.

281 M. Yatomi, M. Koike, N. Rey, Y. Murakami, S. Saito, H. Wada, A. Shimojima, D. Portehault, S. Carenco, C. Sanchez, C. Carcel, M. Wong Chi Man and K. Kuroda, *Eur. J. Inorg. Chem.*, 2021, 1836–1845.

282 M. Nomi, M. Morita, A. Kondo and K. Maeda, *Inorg. Chem.*, 2022, **61**, 5255–5261.

283 D. Sruamsiri, A. Shimojima and M. Ogawa, *ACS Appl. Mater. Interfaces*, 2023, **15**, 41130–41140.

284 E. Doustkhah, N. Tsunoji, M. H. N. Assadi and Y. Ide, *Adv. Mater. Interfaces*, 2023, **10**, 2202368.

285 Y. Ide, N. Ochi and M. Ogawa, *Angew. Chem., Int. Ed.*, 2011, **50**, 654–656.

286 N. Homhuan, S. Bureekaew and M. Ogawa, *Langmuir*, 2017, **33**, 9558–9564.

287 D. Sruamsiri, T. Sirinakorn and M. Ogawa, *Clays Clay Miner.*, 2021, **69**, 416–424.

288 K. Yamamoto, S. E. Borjas Garcia, F. Saito and A. Muramatsu, *Chem. Lett.*, 2006, **35**, 570–571.

289 K. Yamamoto, S. E. Borjas García and A. Muramatsu, *Microporous Mesoporous Mater.*, 2007, **101**, 90–96.

290 S. E. Borjas Garcia, K. Yamamoto and A. Muramatsu, *J. Mater. Sci.*, 2008, **43**, 2367–2371.

291 M. Yabushita, H. Kobayashi, R. Osuga, M. Nakaya, M. Matsubara, S. Maki, K. Kanie and A. Muramatsu, *Ind. Eng. Chem. Res.*, 2021, **60**, 2079–2088.

292 I. A. Crone, K. R. Franklin and P. Graham, *J. Mater. Chem.*, 1995, **5**, 2007–2011.

293 M. Yatomi, T. Hikino, S. Yamazoe, K. Kuroda and A. Shimojima, *Dalton Trans.*, 2023, **52**, 18158–18167.

294 H. Inada, M. Morita and K. Maeda, *Dalton Trans.*, 2024, **53**, 13756–13763.

295 R. E. Grim, *Applied Clay Mineralogy*, McGraw-Hill Inc, US, 1962.

296 F. Bergaya, B. K. G. Theng and G. Lagaly, *Handbook of Clay Science*, Elsevier Science, Amsterdam, 2006.

297 B. K. G. Theng, *The Chemistry of Clay-Organic Reactions*, 2nd edn, CRC Press, Boca Raton, 2024.

10568 | *Chem. Soc. Rev.*, 2024, **53**, 10523–10574

This journal is © The Royal Society of Chemistry 2024

298 H. van Olphen, *An Introduction to Clay Colloid Chemistry*, Wiley-Interscience, New York, 1977.

299 H. Iwase, M. Kubota, T. Itoh, T. Ogura, T. Ebina, H. Ohtani, K. Kurosawa and Y. Fukushima, *Langmuir*, 2021, **37**, 6435–6441.

300 N. Miyamoto and T. Nakato, *Isr. J. Chem.*, 2012, **52**, 881–894.

301 N. Yamaguchi, S. Anraku, E. Paineau, C. R. Safinya, P. Davidson, L. J. Michot and N. Miyamoto, *Sci. Rep.*, 2018, **8**, 4367.

302 N. Miyamoto and S. Yamamoto, *ACS Omega*, 2022, **7**, 6070–6074.

303 T. Inadomi, K. Urayama and N. Miyamoto, *ACS Appl. Polym. Sci.*, 2022, **4**, 4664–4672.

304 M. Ogawa, M. Takahashi, C. Kato and K. Kuroda, *J. Mater. Chem.*, 1994, **4**, 519–523.

305 R. A. Schoonheydt, *Appl. Clay Sci.*, 2014, **96**, 9–21.

306 P. Das, J.-M. Malho, K. Rahimi, F. H. Schacher, B. Wang, D. E. Demco and A. Walther, *Nat. Commun.*, 2015, **6**, 5967.

307 A. P. Teepakakorn and M. Ogawa, *Langmuir*, 2021, **37**, 12887–12896.

308 K. Inukai, Y. Hotta, M. Taniguchi, S. Tomura and A. Yamagishi, *J. Chem. Soc., Chem. Commun.*, 1994, 959.

309 E. R. Kleinfeld and G. S. Ferguson, *Science*, 1994, **265**, 370–373.

310 J. R. Kovacs, C. Liu and P. T. Hammond, *ACS Appl. Mater. Interfaces*, 2015, **7**, 13375–13383.

311 B. V. Lotsch and G. A. Ozin, *Adv. Mater.*, 2008, **20**, 4079–4084.

312 Y. Fukushima and S. Inagaki, *J. Inclusion Phenom.*, 1987, **5**, 473–482.

313 K. Haraguchi and H. J. Li, *Macromolecules*, 2006, **39**, 1898–1905.

314 K. Haraguchi, T. Takada and R. Haraguchi, *ACS Appl. Nano Mater.*, 2018, **1**, 418–425.

315 T. Ebina, *Chem. Rec.*, 2018, **18**, 1020–1032.

316 C. Zhao, P. Zhang, J. Zhou, S. Qi, Y. Yamauchi, R. Shi, R. Fang, Y. Ishida, S. Wang, A. P. Tomsia, M. Liu and L. Jiang, *Nature*, 2020, **58**, 210–215.

317 T. Aizawa, M. Kubota and T. Ebina, *Appl. Clay Sci.*, 2022, **226**, 106571.

318 T. R. Jones, *Clay Miner.*, 1983, **18**, 399–410.

319 M. Minase, T. Hayakawa, M. Oya, K. Fujita and M. Ogawa, *Bull. Chem. Soc. Jpn.*, 2019, **92**, 1329–1334.

320 T. Okada, M. Sohmiya and M. Ogawa, *Struct. Bonding*, 2015, **166**, 177–211.

321 T. Yamaguchi, J.-M. Oh and M. Ogawa, *Struct. Bonding*, 2020, **183**, 251–320.

322 T. Yamaguchi and M. Ogawa, *Sci. Technol. Adv. Mater.*, 2022, **23**, 796–844.

323 S. Takagi, T. Shimada, Y. Ishida, T. Fujimura, D. Masui, H. Tachibana, M. Eguchi and H. Inoue, *Langmuir*, 2013, **29**, 2108–2119.

324 Y. Suzuki, Y. Tenma, Y. Nishioka and J. Kawamata, *Chem. – Asian J.*, 2012, **7**, 1170–1179.

325 W. Soontornchaiyakul, K. Takada, T. Kaneko and M. Ogawa, *Inorg. Chem.*, 2024, **63**, 2787–2792.

326 T. Okada, Y. Ide and M. Ogawa, *Chem. – Asian J.*, 2012, **7**, 1980–1992.

327 A. Phuekphong, K. Imwiset and M. Ogawa, *J. Hazard. Mater.*, 2020, **399**, 122888.

328 A. Yamagishi, K. Tamura, M. Kamon, J. Yoshida and H. Sato, *Appl. Clay Sci.*, 2024, **251**, 107290.

329 A. Yamagishi and H. Sato, *Clays Clay Miner.*, 2012, **60**, 411–419.

330 T. J. Pinnavaia, *Science*, 1983, **220**, 365–371.

331 C. Breen, F. D. Zahoor, J. Madejová and P. Komadel, *J. Phys. Chem. B*, 1997, **101**, 5324–5331.

332 R. Miyawaki, T. Sano, F. Ohashi, M. Suzuki, T. Kogure, T. Okumura, J. Kameda, T. Umezome, T. Sato, D. Chino, K. Hiroyama, H. Yamada, K. Tamura, K. Morimoto, S. Uehara and T. Hatta, *Nendo Kagaku*, 2010, **48**, 158–198.

333 The Clay Minerals Society, **https://www.clays.org/source-and-special-clays/**, (accessed March 2024).

334 The Clay Science Society of Japan, **https://www.cssj2.org/english/reference_clay_e/**, (accessed March 2024).

335 E. A. Warren and B. Ransom, *Clay Miner.*, 1992, **27**, 193–209.

336 W. Loewenstein, *Am. Mineral.*, 1954, **39**, 92–96.

337 C. S. Ross and S. B. Hendricks, in *Minerals of the montmorillonite group, their origin and relation to soils and clays*, ed. C. S. Ross and S. B. Hendricks, U.S. Geol. Survey Prof. Paper, 1945, ch. 205-B, pp. 23–79.

338 D. R. Lewis, in *Analytical data on reference clay materials*, ed. P. F. Kerr, Columbia University, New York, Preliminary Rept. no. 7, Reference Clay Minerals, A.P.I. Project 49, 1950, pp. 91–124.

339 A. Mehlich, *Soil Sci.*, 1948, **66**, 429–446.

340 C. L. Bascomb, *J. Sci. Food Agric.*, 1964, **15**, 821–823.

341 R. Dohrmann, *Appl. Clay Sci.*, 2006, **34**, 31–37.

342 M. Ogawa, Y. Nagafusa, K. Kuroda and C. Kato, *Appl. Clay Sci.*, 1992, **7**, 291–302.

343 P. T. Hang and G. W. Brindley, *Clays Clay Miner.*, 1970, **10**, 203–212.

344 ASTM International, ASTM C837-09(2019), **https://www.astm.org/c0837-09r19.html**, (accessed March 2024).

345 R. Dohrmann, *Appl. Clay Sci.*, 2006, **34**, 38–46.

346 F. Bergaya and M. Vayer, *Appl. Clay Sci.*, 1997, **12**, 275–280.

347 R. E. Grim, W. H. Allaway and F. L. Cuthbert, *J. Am. Ceram. Soc.*, 1947, **30**, 137–142.

348 M. F. Traynor, M. M. Mortland and T. J. Pinnavaia, *Clays Clay Miner.*, 1978, **26**, 318–326.

349 M. Koizumi and R. Roy, *Am. Mineral.*, 1959, **44**, 788–805.

350 J. Méring and G. Perdo, *Bull. Groupe Fr. Argiles*, 1969, **21**, 1–30.

351 J.-F. Joly, L. Huve, P. Martin, R. Le Dred, D. Saehr and J. Baron, *Eur. Pat.*, 92/400522.6, 1992.

352 J. Breu, W. Seidl, A. J. Stoll, K. G. Lange and T. U. Probst, *Chem. Mater.*, 2001, **13**, 4213–4220.

353 T. Egawa, H. Watanabe, T. Fujimura, Y. Ishida, M. Yamato, D. Masui, T. Shimada, H. Tachibana, H. Yoshida, H. Inoue and S. Takagi, *Langmuir*, 2011, **27**, 10722–10729.

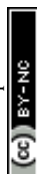354 A. Decarreau, O. Grauby and S. Petit, *Appl. Clay Sci.*, 1992, **7**, 147–167.

This journal is © The Royal Society of Chemistry 2024

Chem. Soc. Rev., 2024, **53**, 10523–10574 | **10569**

355 J. T. Iiyama and R. Roy, *Clay Miner. Bull.*, 1963, **5**, 161–171.

356 H. Suquet, J. T. Iiyama, H. Kodama and H. Pezerat, *Clays Clay Miner.*, 1977, **25**, 231–242.

357 R. J. M. J. Vogels, T. J. Kloprogge, J. W. Geus and A. W. F. Beers, *Am. Mineral.*, 2005, **90**, 945–953.

358 R. J. M. J. Vogels, T. J. Kloprogge and J. W. Geus, *Am. Mineral.*, 2005, **90**, 931–944.

359 R. J. M. J. Vogels, T. J. Kloprogge and J. W. Geus, *J. Catal.*, 2005, **231**, 443–452.

360 M. Reinholdt, J. Miehe-Brendle, L. Delmotte, M. H. Tuilier, R. le Dred, R. Cortes and A. M. Flank, *Eur. J. Inorg. Chem.*, 2001, 2831–2841.

361 K. Torii and T. Iwasaki, *Chem. Lett.*, 1988, 2045–2048.

362 V. C. Farmer, *Clays Clay Miner.*, 1997, **45**, 591–597.

363 BYK Additives & Instruments, **https://www.byk.com/en/products/additives-by-name/laponite-rd**, (accessed March 2024).

364 N. Finck, K. Dardenne and H. Geckeis, *Chem. Geol.*, 2015, **409**, 12–19.

365 H. Brandt, D. Bosbach, P. J. Panak and T. Fanghänel, *Geochim. Cosmochim. Acta*, 2007, **71**, 145–154.

366 P. H. Michels-Brito, V. Dudko, D. Wagner, P. Markus, G. Papastavrou, L. Michels, J. Breu and J. O. Fossum, *Sci. Adv.*, 2022, **8**, eabl8147.

367 P. Komadel, J. Madejova and J. W. StuckIi, *Clays Clay Miner.*, 1999, **47**, 458–465.

368 H. Yamada, K. Yoshioka and H. Nakazawa, *Mineral. J.*, 1991, **15**, 300–308.

369 H. Yamada, H. Nakazawa, K. Yoshioka and T. Fujita, *Clay Miner.*, 1991, **26**, 359–369.

370 J. T. Kloprogge, S. Komarneni and J. E. Amonetie, *Clays Clay Miner.*, 1999, **47**, 529–554.

371 K. Urabe, H. Sakurai and Y. Izumi, *J. Chem. Soc., Chem. Commun.*, 1988, 1520–1521.

372 M. Ogawa, R. Kawai and K. Kuroda, *J. Phys. Chem. B*, 1996, **100**, 16218–16221.

373 P. Saengdet and M. Ogawa, *Chem. Commun.*, 2022, **58**, 3278–3281.

374 Y. Ishida, T. Shimada, H. Tachibana, H. Inoue and S. Takagi, *J. Phys. Chem. A*, 2012, **116**, 12065–12072.

375 C. H. Zhou, Q. Zhou, Q. Q. Wu, S. Petit, X. C. Jiang, S. T. Xia, C. S. Li and W. H. Yu, *Appl. Clay Sci.*, 2018, **168**, 136–154.

376 R. S. Varma, *Tetrahedron*, 2002, **58**, 1235–1255.

377 H. Heinz, H. Koerner, K. L. Anderson, R. A. Vaia and B. L. Farmer, *Chem. Mater.*, 2005, **17**, 5658–5669.

378 W. Shen, L. Li, H. Zhou, Q. Zhou, M. Chen and J. Zhu, *Appl. Clay Sci.*, 2016, **159**, 10–15.

379 K. Ohtsuka, *Chem. Mater.*, 1997, **9**, 2039–2050.

380 P. Laszlo, *Science*, 1987, **235**, 1473–1477.

381 M. Arai, S. L. Guo, M. Shirai, Y. Nishiyama and K. Torii, *J. Catal.*, 1996, **161**, 704–712.

382 B. Zhoufeng and K. Sibudjing, *J. CO₂ Util.*, 2017, **18**, 345–352.

383 S. Higashi, K. Miki and S. Komarneni, *Clays Clay Miner.*, 2002, **50**, 299–305.

384 C. Q. Zhang, H. P. He, Q. Tao, S. C. Ji, S. Y. Li, L. Y. Ma, X. L. Su and J. X. Zhu, *Appl. Clay Sci.*, 2017, **135**, 282–288.

385 V. Luca, D. J. MacLachlan, R. F. Howe and R. Bramley, *J. Mater. Chem.*, 1995, **5**, 557–564.

386 A. Phuekphong, T. Hayakawa and M. Ogawa, *Chem. Commun.*, 2022, **58**, 12661–12664.

387 M. Ogawa, T. Matsutomo and T. Okada, *Bull. Chem. Soc. Jpn.*, 2009, **82**, 408–412.

388 T. B. Hofstetter, R. P. Schwarzenbach and S. B. Haderlein, *Environ. Sci. Technol.*, 2003, **37**, 519–528.

389 J. R. White and A. J. Bard, *J. Electroanal. Chem.*, 1986, **197**, 233–244.

390 B. K. G. Theng, *Clays Clay Miner.*, 1971, **19**, 383–390.

391 D. T. B. Tennakoon, J. M. Thomas, M. J. Tricker and J. O. Williams, *J. Chem. Soc., Dalton Trans.*, 1974, **20**, 2207–2211.

392 Y. Qian, A. C. Scheinost, S. Grangeon, A. Hoving, S. V. Churakov and M. M. Fernandes, *Geochim. Cosmochim. Acta*, 2024, **377**, 19–33.

393 F. Bergaya and H. V. Damme, *J. Chem. Soc., Faraday Trans.*, 1983, **79**, 505–518.

394 A. Habti, D. Keravis, P. Levitz and H. van Damme, *J. Chem. Soc., Faraday Trans. 2*, 1984, **80**, 67–83.

395 R. A. Schoonheydt, P. De Pauw, D. Vliers and F. C. De Schrijver, *J. Phys. Chem.*, 1984, **88**, 5113–5118.

396 P. A. Teepakakorn, S. Bureekaew and M. Ogawa, *Langmuir*, 2018, **34**, 14069–14075.

397 A. P. Teepakakorn, T. Yamaguchi and M. Ogawa, *Chem. Lett.*, 2019, **48**, 398–409.

398 A. Nag, T. Hayakawa, M. Minase and M. Ogawa, *Langmuir*, 2022, **38**, 2979–2985.

399 P. M. Saengdet and M. Ogawa, *Langmuir*, 2024, **40**, 1016–1023.

400 J. W. Stucki, D. C. Golden and C. B. Roth, *Clays Clay Miner.*, 1984, **32**, 350–356.

401 J. W. Stucki, P. F. Low, C. B. Roth and D. C. Golden, *Clays Clay Miner.*, 1984, **32**, 357–362.

402 J. W. Stucki, J. Wu, H. Gan, P. Komadel and A. Banin, *Clays Clay Miner.*, 2000, **48**, 290–298.

403 S. Petit, F. Baron and A. Decarreau, *Clay Miner.*, 2017, **52**, 469–483.

404 S. Caillere, S. Henin and J. Esquevin, *J. Bull. Soc. Francaise Miner. Cristallogr.*, 1955, **78**, 227–241.

405 H. Harder, *Clays Clay Miner.*, 1978, **26**, 65–72.

406 A. Decarreau, D. Bonnin, D. Badaut-Trauth, R. Couty and P. Kaiser, *Clays Clay Miner.*, 1987, **22**, 207–223.

407 K. Tomita, H. Yamane and M. Kawano, *Clays Clay Miner.*, 1993, **41**, 655–661.

408 V. C. Farmer, W. J. McHardy, F. Elsass and M. Robert, *Clays Clay Miner.*, 1994, **42**, 180–186.

409 A. Manceau, V. A. Drits, B. Lanson, D. Chateigner, J. Wu, D. Huo, W. P. Gates and J. W. Stucki, *Am. Mineral.*, 2000, **85**, 153–172.

410 O. Grauby, S. Petit, A. Decarreau and A. Baronnet, *Eur. J. Mineral.*, 1994, **6**, 99–112.

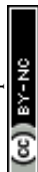411 S. Higashi, K. Miki and S. Komarneni, *Appl. Clay Sci.*, 2007, **38**, 104–112.

10570 | *Chem. Soc. Rev.*, 2024, **53**, 10523–10574

This journal is © The Royal Society of Chemistry 2024

412 N. J. Tosca and A. L. Masterson, *Clay Miner.*, 2014, **49**, 165–194.

413 M. Reinholdt, J. Miehe-Brendle, L. Delmotte, M. H. Tuilier and R. le Dred, *Clay Miner.*, 2001, **40**, 177–190.

414 U. Hofmann and R. Klemen, *Z. Anorg. Chem.*, 1950, **262**, 95–99.

415 P. Komadel, J. Madejova and K. Bujdak, *Clays Clay Miner.*, 2005, **53**, 313–334.

416 K. Takahashi, R. Ishii, T. Nakamura, A. Suzuki, T. Ebina, M. Yoshida, M. Kubota, T. T. Nge and T. Yamada, *Adv. Mater.*, 2017, **29**, 1606512.

417 J. Bujdak and N. Iyi, *Clays Clay Miner.*, 2002, **50**, 446–454.

418 J. Bujdak, *J. Phys. Chem. C*, 2015, **119**, 12016–12022.

419 W. F. Jaynes and S. A. Boyd, *Clays Clay Miner.*, 1991, **39**, 428–436.

420 R. Zhu, L. Zhu and L. Xu, *Colloids Surf., A*, 2007, **294**, 221–227.

421 R. Zhu, J. Zhao, F. Ge, L. Zhu, J. Zhu, Q. Tao and H. He, *Appl. Clay Sci.*, 2014, **88–89**, 73–77.

422 A. L. Barrientos-Velázquez, A. M. Cardona, L. Liu, T. Phillips and Y. Deng, *Appl. Clay Sci.*, 2016, **132–133**, 281–289.

423 S. Jatav and Y. M. Joshi, *Appl. Clay Sci.*, 2014, **97–98**, 72–77.

424 J. Zhang, C.-H. Zhou, S. Petit and H. Zhang, *Appl. Clay Sci.*, 2019, **177**, 114–138.

425 W. T. Granquist and S. S. Pollack, *Clays Clay Miner.*, 1960, **8**, 150–169.

426 K. A. Carrado, P. Thiyagarajan and K. Song, *Clay Miner.*, 1997, **32**, 29–40.

427 K. A. Carrado, L. Xu, D. M. Gregory, K. Song, S. Seifert and R. E. Botto, *Chem. Mater.*, 2000, **12**, 3052–3059.

428 N. Finck, T. Stumpf, C. Walther and D. Bosbach, *J. Contam. Hydrol.*, 2008, **102**, 253–262.

429 T. Iwasaki, M. Reinikainen, Y. Onodera, H. Hayashi, T. Ebina, T. Nagase, K. Torii, K. Kataja and A. Chatterjee, *Appl. Surf. Sci.*, 1998, **130–132**, 845–850.

430 M. Ogawa, T. Matsutomo and T. Okada, *J. Ceram. Soc. Jpn.*, 2008, **116**, 1309–1313.

431 T. Okada, T. Matsutomo and M. Ogawa, *J. Phys. Chem. C*, 2010, **114**, 539–545.

432 T. Okada, A. Suzuki, S. Yoshido and H. M. Minamisawa, *Microporous Mesoporous Mater.*, 2015, **215**, 168–174.

433 T. Sánchez, P. Salagre and Y. Cesteros, *Microporous Mesoporous Mater.*, 2013, **171**, 24–34.

434 G. Wang, J. Wei, G. Liang, Y. Chen, S. Ma, J. Zhu and H. Liu, *Colloids Surf., A*, 2024, **687**, 133475.

435 S. Petit, D. Righi and A. Decarreau, *Clays Clay Miner.*, 2008, **56**, 645–654.

436 H. Harder, *Clay Miner.*, 1977, **12**, 281–288.

437 K. Tomita, H. Yamane and M. Kawano, *Clays Clay Miner.*, 1993, **41**, 655–661.

438 H. Harder, *Chem. Geol.*, 1976, **18**, 169–180.

439 M. Jaber and J. Miehé-Brendlé, *Microporous Mesoporous Mater.*, 2008, **107**, 121–127.

440 J. Brendlé, *Dalton Trans.*, 2018, **47**, 2925–2932.

441 A. J. Patil, E. Muthusamy and S. Mann, *Angew. Chem., Int. Ed.*, 2004, **43**, 4928–4933.

442 K. K. R. Datta, A. Achari and M. Eswaramoorthy, *J. Mater. Chem. A*, 2013, **1**, 6707–6718.

443 M. Claverie, A. Dumas, C. Carême, M. Poirier, C. Le Roux, P. Micoud, F. Martin and C. Aymonier, *Chem. – Eur. J.*, 2018, **24**, 519–542.

444 Y. Fukushima and M. Tani, *J. Chem. Soc., Chem. Commun.*, 1995, 241–242.

445 Y. Fukushima and M. Tani, *Bull. Chem. Soc. Jpn.*, 1996, **69**, 3667–3671.

446 M. Jaber and J. Miehé-Brendlé, *J. Mater. Sci.*, 2004, **39**, 1489–1490.

447 T. Okada, N. Taguchi and S. Shimomura, *Colloids Surf., A*, 2023, **676**, 132135.

448 M. Jaber, J. Miehé-Brendlé, L. Delmotte and R. Le Dred, *Microporous Mesoporous Mater.*, 2003, **65**, 155–163.

449 M. Jaber, J. Miehé-Brendlé, M. Roux, J. Dentzer, R. Le Dred and J. Guth, *New J. Chem.*, 2002, **26**, 1597–1600.

450 M. Yamauchi and T. Okada, *Clays Clay Miner.*, 2018, **66**, 104–113.

451 K. A. Carrado, L. Xu, R. Csencsits and J. V. Muntean, *Chem. Mater.*, 2001, **13**, 3766–3773.

452 H. Yamada, *Nendo Kagaku*, 2001, **41**, 87–96.

453 K. A. Carrado, *Appl. Clay Sci.*, 2000, **17**, 1–23.

454 H. Yamada, H. Nakazawa and H. Hashizume, *Clays Clay Miner.*, 1994, **42**, 674–678.

455 M. M. Herling, H. Kalo, S. Seibt, R. Schobert and J. Breu, *Langmuir*, 2012, **28**, 14713–14719.

456 M. Stöter, D. A. Kunz, M. Schmidt, D. Hirsemann, H. Kalo, B. Putz, J. Senker and J. Breu, *Langmuir*, 2013, **29**, 1280–1285.

457 M. Röhrl, R. L. Timmins, S. Rosenfeldt, D. D. Schuchardt, F. Uhlig, S. Nürmberger and J. Breu, *ACS Appl. Mater. Interfaces*, 2023, **15**, 22524–22531.

458 D. D. Schuchardt, S. Rosenfeldt, H. Kalo and J. Breu, *Nanoscale*, 2023, **15**, 7044–7050.

459 C. Habel, E. S. Tsurko, R. L. Timmins, J. Hutschreuther, R. Kunz, D. D. Schuchardt, S. Rosenfeldt, V. Altstädt and J. Breu, *ACS Nano*, 2020, **14**, 7018–7024.

460 M. Stöcker, W. Seidl, L. Seyfarth, J. Senker and J. Breu, *Chem. Commun.*, 2008, 629–631.

461 M. Stöcker, L. Seyfarth, D. Hirsemann, J. Senker and J. Breu, *Appl. Clay Sci.*, 2010, **48**, 146–153.

462 R. Mariychuk, A. Baumgartner, F. E. Wagner, A. Lerf, A. Dubbe, R. Moos and J. Breu, *Chem. Mater.*, 2007, **19**, 5377–5387.

463 A. Baumgartner, K. Sattler, J. Thun and J. Breu, *Angew. Chem., Int. Ed.*, 2008, **47**, 1640–1644.

464 R. Greene-Kelly, *J. Soil Sci.*, 1953, **4**, 233–237.

465 E. N. Skoubris, G. D. Chryssikos, G. E. Christidis and V. Gionis, *Clays Clay Miner.*, 2013, **61**, 83–97.

466 G. E. Christidis and D. D. Eberl, *Clays Clay Miner.*, 2013, **61**, 644–655.

467 A. R. Mermut, *Layer Charge Characteristics of 2:1 Silicate Clay Minerals*, CMS workshop lectures, Clay Miner. Society, Aurora, USA, 1994, vol. 6.

468 J. W. Jordan, *J. Phys. Colloid Chem.*, 1950, **54**, 294–306.

This journal is © The Royal Society of Chemistry 2024

Chem. Soc. Rev., 2024, **53**, 10523–10574 | **10571**

469 G. Lagaly, *Clay Miner.*, 1981, **16**, 1–16.

470 K. Imwiset, A. Teepakakorn, P. Saengdet, C. Tiraya-phanitchkul and M. Ogawa, in *Concepts and Design of Materials Nanoarchitectonics*, ed. O. Azzaroni and K. Ariga, The Royal Society of Chemistry, Croydon, 2022, ch. 12, pp. 247–278.

471 BYK Additives & Instruments, Cloisite, **https://www.byk.com/en/product/additive-guide/cloisite**, (accessed March 2024).

472 HOJUN Co., Ltd, Organophilic bentonites, **https://www.hojun.co.jp/eng/e29_f_chemicals_no.html**, (accessed March 2024).

473 T. Hayakawa, M. Minase, K. Fujita and M. Ogawa, *Clays Clay Miner.*, 2016, **64**, 275–282.

474 P. R. Bodart, L. Delmotte, S. Rigolet, J. Brendlé and R. D. Gougeon, *Appl. Clay Sci.*, 2018, **157**, 204–211.

475 M. Lipsicas, R. H. Raythatha, T. J. Pinnavaia, I. D. Johnson, R. F. Giese, P. M. Costanzo and J. L. Robert, *Nature*, 1984, **309**, 604–607.

476 D. Plee, F. Borg, L. Gatineau and J. J. Fripiat, *J. Am. Chem. Soc.*, 1985, **107**, 2362–2369.

477 G. W. Brindley, in *X-Ray Identification and Crystal Structures of Clay Minerals*, ed. G. W. Brindley, Taylor and Francis, London, 1951, pp. 159–164.

478 L. Heller and I. Rozenson, *Phys. Chem. Miner.*, 1981, **7**, 223–238.

479 I. Rozenson and L. Herrer-Kallai, *Clays Clay Miner.*, 1976, **24**, 283–288.

480 J. D. Russel, B. A. Goodman and A. R. Fraser, *Clays Clay Miner.*, 1979, **27**, 63–71.

481 J. W. Stucki, G. W. Bailey and H. Gan, *Appl. Clay Sci.*, 1996, **10**, 417–430.

482 T. B. Hofstetter, A. Neumann and R. P. Schwarzenbach, *Environ. Sci. Technol.*, 2006, **40**, 235–242.

483 J. W. Stucki and C. B. Roth, *Clays Clay Miner.*, 1977, **41**, 808–814.

484 H. Gan, J. W. Stucki and G. W. Bailey, *Clays Clay Miner.*, 1992, **40**, 659–665.

485 C. P. Ponce and J. T. Kloprogge, *Life*, 2020, **10**, 168.

486 T. Okada, M. Sueyoshi and H. M. Minamisawa, *Langmuir*, 2015, **31**, 13842–13849.

487 E. Pavón, F. J. Osuna, M. D. Alba and L. Delevoye, *Solid State Nucl. Magn. Reson.*, 2019, **100**, 45–51.

488 A. Dumas, M. Mizrahi, F. Martin and F. G. Requejo, *Cryst. Growth Des.*, 2015, **15**, 5451–5463.

489 T. Okada, A. Kumasaki, K. Shimizu, A. Yamagishi and H. Sato, *J. Chromatogr. Sci.*, 2016, **54**, 1238–1243.

490 T. Okada, S. Hosoyamada, C. Takada and C. Ohta, *ChemPhotoChem*, 2021, **5**, 32–35.

491 Y. Nakauchi, H. Minamisawa and T. Okada, *Dalton Trans.*, 2024, **53**, 2558–2564.

492 V. Shklover, T. Haibach, F. Ried, R. Nesper and P. Novák, *J. Solid State Chem.*, 1996, **123**, 317–323.

493 J. E. Post and D. R. Veblen, *Am. Mineral.*, 1990, **75**, 477–489.

494 M. Catti, I. Pinus and A. Scherillo, *J. Solid State Chem.*, 2013, **205**, 64–70.

495 J. Kwiatkowska, I. E. Grey, I. C. Madsen and L. A. Bursill, *Acta Crystallogr.*, 1987, **B43**, 258–265.

496 S. Anderson and A. D. Wadsley, *Acta Crystallogr.*, 1961, **14**, 1245–1249.

497 A. D. Wadsley, *Acta Crystallogr.*, 1964, **17**, 623–628.

498 M. Gasperin and M. T. le Bihan, *J. Solid State Chem.*, 1982, **43**, 346–353.

499 D. B. Rogers, R. D. Shannon, A. W. Sleight and J. L. Gillson, *Inorg. Chem.*, 1969, **8**, 841–849.

500 W. D. Ryden, A. W. Lawson and C. C. Sartain, *Phys. Rev. B: Condens. Matter Mater. Phys.*, 1970, **1**, 1494–1500.

501 J. Livage, M. Henry and C. Sanchez, *Prog. Solid State Chem.*, 1988, **18**, 259–341.

502 S. L. Brock, N. Duan, Z. R. Tian, O. Giraldo, H. Zhou and S. L. Suib, *Chem. Mater.*, 1998, **10**, 2619–2628.

503 T. Taniguchi, L. Nurdiwijayanto, R. Ma and T. Sasaki, *Appl. Phys. Rev.*, 2022, **9**, 021313.

504 F. Geng, R. Ma, A. Nakamura, K. Akatsuka, Y. Ebina, Y. Yamauchi, N. Miyamoto, Y. Tateyama and T. Sasaki, *Nat. Commun.*, 2013, **4**, 1632.

505 R. Uppuluri, A. S. Gupta, A. S. Rosas and T. E. Mallouk, *Chem. Soc. Rev.*, 2018, **47**, 2401–2430.

506 P. Wattanapaphawong, P. Reubroycharoen, C. Samart, L. Kou, J. Song, J. Su and K. Kajiyoshi, *Appl. Ceram. Technol.*, 2024, **21**, 750–758.

507 X. Wang, X. Li, S. Aya, F. Araoka, Y. Ishida, A. Kikkawa, M. Kriener, Y. Taguchi, Y. Ebina, T. Sasaki, S. Koshiya, K. Kimoto and T. Aida, *J. Am. Chem. Soc.*, 2018, **140**, 16396–16401.

508 Y. Shi, M. Osada, Y. Ebina and T. Sasaki, *ACS Nano*, 2020, **14**, 15216–15226.

509 K. Awaya, A. Takashida, T. Taniguchi, M. Koinuma, T. Ishihara and S. Ida, *Chem. Commun.*, 2019, **55**, 4586–4588.

510 Y. Shi, E. Yamamoto, M. Kobayashi and M. Osada, *ACS Appl. Mater. Interfaces*, 2023, **15**, 22737–22743.

511 T. Sasaki, Y. Ebina, T. Tanaka, M. Harada, M. Watanabe and G. Decher, *Chem. Mater.*, 2001, **13**, 4661–4667.

512 K. Matsuba, C. Wang, K. Saruwatari, Y. Uesusuki, K. Akatsuka, M. Osada, Y. Ebina, R. Ma and T. Sasaki, *Sci. Adv.*, 2017, **3**, e1700414.

513 K. Awaya and S. Ida, *Chem. Commun.*, 2020, **56**, 9811–9814.

514 N. Sakai and T. Sasaki, *Acc. Mater. Res.*, 2024, **5**, 752–760.

515 S. J. Hwang, T. Zhang and I. Chung, *Coord. Chem. Rev.*, 2021, **430**, 213762.

516 N. H. Kwon, K.-G. Lee, H. K. Kim and S. J. Hwang, *Mater. Chem. Front.*, 2021, **5**, 3549–3575.

517 K. Ament, D. R. Wagner, T. Götsch, T. Kikuchi, J. Kröhnert, A. Trunschke, T. Lunkenbein, T. Sasaki and J. Breu, *ACS Catal.*, 2021, **11**, 2754–2762.

518 B. Ohtani, S. Ikeda, H. Nakayama and S. Nishimoto, *Phys. Chem. Chem. Phys.*, 2000, **2**, 5308–5313.

519 Y. Ide, Y. Nakasato and M. Ogawa, *J. Am. Chem. Soc.*, 2010, **132**, 3601–3604.

520 Y. Ide, M. Matsuoka and M. Ogawa, *J. Am. Chem. Soc.*, 2010, **132**, 16762–16764.

10572 | *Chem. Soc. Rev.*, 2024, **53**, 10523–10574

This journal is © The Royal Society of Chemistry 2024

521 A. Kudo and T. Sakata, *J. Phys. Chem.*, 1995, **99**, 15963–15967.

522 A. Kudo, *Chem. Mater.*, 1997, **9**, 664–669.

523 J. Du, K. Li, R. Van Deun, D. Poelman and H. Lin, *Adv. Opt. Mater.*, 2022, **10**, 2101714.

524 Q. Du, J. Ueda and S. Tanabe, *J. Mater. Chem. C*, 2023, **11**, 16225–16233.

525 H. Yim, S. Y. Yoo, Y. H. Kim, K. H. Chae, Y.-H. Kim, S. K. Kim, S.-H. Baek, C.-H. Lee and J.-W. Choi, *Chem. Mater.*, 2021, **33**, 8685–8692.

526 H. Yim, S. Y. Yoo, H. Choi, H. J. Chang, S.-J. Hwang, S. Nahm, M. Osada and J.-W. Choi, *J. Alloys Compd.*, 2022, **925**, 166606.

527 N. N. Rabin, S. Ida, M. R. Karim, Md. S. Islam, R. Ohatni, M. Nakamura, M. Koinuma, L. Lindoy and S. Hayami, *ACS Omega*, 2018, **3**, 2074–2083.

528 T. Sasaki, F. Kooli, M. Iida, Y. Michiue, S. Takenouchi, Y. Yajima, F. Izumi, B. C. Chakoumakos and M. Watanabe, *Chem. Mater.*, 1998, **10**, 4123–4128.

529 A. J. Jacobson, J. W. Johnson and J. T. Lewandowski, *Mater. Res. Bull.*, 1987, **22**, 45–51.

530 A. F. Reid, W. G. Mumme and A. D. Wadsley, *Acta Crystallogr.*, 1968, **B24**, 1228–1232.

531 D. Groult, C. Mercey and B. Raveau, *J. Solid State Chem.*, 1980, **32**, 289–296.

532 M. Hervieu and B. Raveau, *Rev. Chim. Miner.*, 1981, **18**, 642–649.

533 I. E. Grey, C. Li, I. C. Madsen and J. A. Watts, *J. Solid State Chem.*, 1987, **66**, 7–19.

534 T. Sasaki, Y. Komatsu and Y. Fujiki, *J. Chem. Soc., Chem. Commun.*, 1991, 817–818.

535 M. Osada, Y. Ebina, K. Takada and T. Sasaki, *Adv. Mater.*, 2006, **18**, 295–299.

536 M. Osada, Y. Ebina, K. Fukuda, K. Ono, K. Takada, K. Yamaura, E. Takayama-Muromachi and T. Sasaki, *Phys. Rev. B: Condens. Matter Mater. Phys.*, 2006, **73**, 153301.

537 X. Dong, M. Osada, H. Ueda, Y. Ebina, Y. Kotani, K. Ono, S. Ueda, K. Kobayashi, K. Takada and T. Sasaki, *Chem. Mater.*, 2009, **21**, 4366–4373.

538 M. Osada, S. Yoguchi, M. Itose, B.-W. Li, Y. Ebina, K. Fukuda, Y. Kotani, K. Ono, S. Ueda and T. Sasaki, *Nanoscale*, 2014, **6**, 14227–14236.

539 F. Kishimoto, Y. Takamura, S. Nakagawa and Y. Wada, *Adv. Mater. Interfaces*, 2016, **3**, 1600509.

540 Y. Ide, M. Sadakane, T. Sano and M. Ogawa, *J. Nanosci. Nanotechnol.*, 2014, **14**, 2135–2147.

541 A. J. Jacobson, J. W. Johnson and J. T. Lewandowski, *Inorg. Chem.*, 1985, **24**, 3727–3729.

542 T. Tokumitsu, K. Toda, T. Aoyagi, D. Sakuraba, K. Uematsu and M. Sato, *J. Ceram. Soc. Jpn.*, 2006, **114**, 795–797.

543 H. Suzuki, O. Tomita, M. Higashi and R. Abe, *Catal. Sci. Technol.*, 2015, **5**, 2640–2648.

544 T. Oshima, T. Yokoi, M. Eguchi and K. Maeda, *Dalton Trans.*, 2017, **46**, 10594–10601.

545 S. Atri, M. Pokhriyal and S. Uma, *Inorg. Chem.*, 2020, **59**, 8044–8053.

546 S. Pal and S. Uma, *Ceram. Int.*, 2024, **50**, 31540–31547.

547 H. J. Kim, S. Morita, K.-N. Byun, Y. Shi, T. Taniguchi, E. Yamamoto, M. Kobayashi, Y. Ebina, T. Sasaki and M. Osada, *Nano Lett.*, 2023, **23**, 3788–3795.

548 B.-W. Li, M. Osada, Y. Ebina, T. C. Ozawa, R. Ma and T. Sasaki, *Appl. Phys. Lett.*, 2010, **96**, 182903.

549 T. B. N. Le, C.-W. Chang and Y.-H. Su, *Surf. Interfaces*, 2023, **36**, 102623.

550 R. Liu, B. Feng, Y. Ma, H. Liu, J. Cui, D. Yang and H. Yuan, *Mater. Lett.*, 2020, **281**, 128635.

551 Y. Zhou, T. Wen, X. Zhang, B. Chang, W. Kong, Y. Guo, B. Yang and Y. Wang, *Chem. – Asian J.*, 2017, **12**, 2727–2733.

552 M. R. Aziza, C.-W. Chang, A. Mohapatra, C.-W. Chu, C.-C. Kaun and Y.-H. Su, *ACS Appl. Nano Mater.*, 2020, **3**, 6367–6375.

553 W. Zhang and M. Yashima, *Chem. Commun.*, 2023, **59**, 134–152.

554 D. Hamada, M. Machida, Y. Sugahara and K. Kuroda, *J. Mater. Chem.*, 1996, **6**, 69–72.

555 S. Uma and J. Gopalakrishnan, *J. Solid State Chem.*, 1993, **102**, 332–339.

556 S. Uma, A. R. Raju and J. Gopalakrishnan, *J. Mater. Chem.*, 1993, **3**, 709–713.

557 J. Gopalakrishnan, S. Uma and V. Bhat, *Chem. Mater.*, 1993, **5**, 132–136.

558 D. Hamada, M. Machida, Y. Sugahara and K. Kuroda, *J. Ceram. Soc. Jpn.*, 1997, **105**, 284–287.

559 Y. Huang, J. Li, Y. Wei, Y. Li, J. Lin and J. Wu, *J. Hazard. Mater.*, 2009, **166**, 103–108.

560 M. Osada and T. Sasaki, *Int. J. Ceram. Technol.*, 2012, **9**, 29–36.

561 T.-H. Wang, C.-L. Chiang, P.-C. Li, Y.-K. Hsieh and C.-F. Wang, *Chem. Eng. J.*, 2014, **244**, 243–251.

562 Y. Matsumoto, S. Ida and T. Inoue, *J. Phys. Chem. C*, 2008, **112**, 11614–11616.

563 M. Khodabakhsh, B. Yilmaz, S. Firoozi, D. F. Haghshenas and U. Unal, *ACS Omega*, 2023, **8**, 10607–10617.

564 S. Dong, J. Feng, M. Fan, Y. Pi, L. Hu, X. Han, M. Liu, J. Sun and J. Sun, *RSC Adv.*, 2015, **5**, 14610–14630.

565 Y. Huang, Y. Li, Y. Wei, M. Huang and J. Wu, *Sol. Energy Mater. Sol. Cells*, 2011, **95**, 1019–1027.

566 M. Harada, T. Sasaki, Y. Ebina and M. Watanabe, *J. Photochem. Photobiol., A*, 2002, **148**, 273–276.

567 T. Sasaki and M. Watanabe, *J. Phys. Chem. B*, 1997, **101**, 10159–10161.

568 R. Hiroi, S. S. Ray, M. Okamoto and T. Shiroi, *Macromol. Rapid Commun.*, 2004, **25**, 1359–1364.

569 Y. Fuse, Y. Ide and M. Ogawa, *Bull. Chem. Soc. Jpn.*, 2008, **81**, 767–772.

570 K. Maeda, M. Eguchi and T. Oshima, *Angew. Chem., Int. Ed.*, 2014, **53**, 13164–13168.

571 D. E. Scaife, *Sol. Energy*, 1980, **25**, 41–54.

572 Y. Matsumoto, *J. Solid State Chem.*, 1996, **126**, 227–234.

573 P. Xu, T. J. Milstein and T. E. Mallouk, *ACS Appl. Mater. Interfaces*, 2016, **8**, 11539–11547.

This journal is © The Royal Society of Chemistry 2024

Chem. Soc. Rev., 2024, **53**, 10523–10574 | **10573**

574 M. Lv, X. Sun, S. Wei, C. Shen, Y. Mi and X. Xu, *ACS Nano*, 2017, **11**, 11441–11448.

575 Y. Tang, K. Kato, T. Oshima, H. Mogi, A. Miyoshi, K. Fujii, K. Yanagisawa, K. Kimoto, A. Yamakata, M. Yashima and K. Maeda, *Inorg. Chem.*, 2020, **59**, 11122–11128.

576 Y. Zhou, T. Wen, Y. Guo, B. Yang and Y. Wang, *RSC Adv.*, 2016, **69**, 64930–64936.

577 K. Maeda, Y. Tokunaga, K. Hibino, K. Fujii, H. Nakaki, T. Uchiyama, M. Eguchi, D. Lu, S. Ida, Y. Uchimoto and M. Yashima, *ACS Appl. Energy Mater.*, 2018, **1**, 1734–1741.

578 H. Wakayama, K. Hibino, K. Fujii, T. Oshima, K. Yanagisawa, Y. Kobayashi, K. Kimoto, M. Yashima and K. Maeda, *Inorg. Chem.*, 2019, **58**, 6161–6166.

579 T. Oshima, T. Ichibha, K. Oqmhula, K. Hibino, H. Mogi, S. Yamashita, K. Fujii, Y. Miseki, K. Hongo, D. Lu, R. Maezono, K. Sayama, M. Yashima, K. Kimoto, H. Kato, M. Kakihana, H. Kageyama and K. Maeda, *Angew. Chem., Int. Ed.*, 2020, **59**, 9736–9743.

580 Y. Shiroma, H. Mogi, T. Mashiko, S. Yasuda, S. Nishioka, T. Yokoi, S. Ida, K. Kimoto and K. Maeda, *J. Mater. Chem. A*, 2023, **11**, 9485–9492.

581 S. Ida, N. Kim, E. Ertekin, S. Takenaka and T. Ishihara, *J. Am. Chem. Soc.*, 2015, **137**, 239–244.

582 Y. Okamoto, S. Ida, J. Hyodo, H. Hagiwara and T. Ishihara, *J. Am. Chem. Soc.*, 2011, **133**, 18034–18037.

583 T. Gao, H. Fjellvåg and P. Norby, *J. Mater. Chem.*, 2009, **19**, 787–794.

584 K. Saito, S. Orikasa, Y. Asakura, Y. Ide, Y. Sugahara, M. Ogasawara, S. Yin and S. Kato, *Int. J. Photoenergy*, 2021, **2021**, 8847956.

585 K. Saito, S. Tominaka, S. Yoshihara, K. Ohara, Y. Sugahara and Y. Ide, *ACS Appl. Mater. Interfaces*, 2017, **9**, 24538–24544.

586 T. Maluangnont, B. Wuttitham, P. Hongklai, P. Khunmee, S. Tippayasukho, N. Chanlek and T. Sooknoi, *Inorg. Chem.*, 2019, **58**, 6885–6892.

587 T. Maluangnont, N. Chanlek, O. Khamman, W. Vittayakorn and T. Sooknoi, *Inorg. Chem.*, 2021, **60**, 16326–16336.

588 G. Zhang, J. Gong, H. Gan and F. Lü, *J. Alloys Compd.*, 2011, **509**, 9791–9797.

589 M. Ogawa, M. Morita, S. Igarashi and S. Sato, *J. Solid State Chem.*, 2013, **206**, 9–13.

590 S. Igarashi, S. Sato, T. Takashima and M. Ogawa, *Ind. Eng. Chem. Res.*, 2013, **52**, 3329–3333.

591 M. Ohashi, *Mol. Cryst. Liq. Cryst.*, 1998, **311**, 51–56.

592 B. W. Li, M. Osada, Y. H. Kim, Y. Ebina, K. Akatsuka and T. Sasaki, *J. Am. Chem. Soc.*, 2017, **139**, 10868–10874.

593 X. Li, W. Ke, B. Traoré, P. Guo, I. Hadar, M. Kepenekian, J. Even, C. Katan, C. C. Stoumpos, R. D. Schaller and M. G. Kanatzidis, *J. Am. Chem. Soc.*, 2019, **141**, 12880–12890.

594 M. Ogawa, H. Suzuki, K. Ogawa, O. Tomita and R. Abe, *Solid State Sci.*, 2023, **141**, 107221.

595 J. Liu, C. Deng, X. Liu, S. Shao, P. Zheng, L. Chen, P. Wu, H. Li, H. Ji and W. Zhu, *Inorg. Chem.*, 2023, **62**, 11044–11055.

596 K. Sano, Y. S. Kim, Y. Ishida, Y. Ebina, T. Sasaki, T. Hikima and T. Aida, *Nat. Commun.*, 2016, **7**, 12559.

597 W. Yang, S. Yamamoto, K. Sueyoshi, T. Inadomi, R. Kato and N. Miyamoto, *Angew. Chem., Int. Ed.*, 2021, **60**, 8466–8471.

598 M. Ohwada, K. Kimoto, T. Mizoguchi, Y. Ebina and T. Sasaki, *Sci. Rep.*, 2013, **3**, 2801.

599 P. Xiong, F. Zhang, X. Zhang, Y. Liu, Y. Wu, S. Wang, J. Safaei, B. Sun, R. Ma, Z. Liu, Y. Bando, T. Sasaki, X. Wang, J. Zhu and G. Wang, *Nat. Commun.*, 2021, **12**, 4184.

600 C. Liu, C. Ye, Y. Wu, Y. Liu, Z. Liu, Z. Chen, R. Ma, N. Sakai, L. Xue, J. Sun, W. Zhang, W. Zhang, X. Wang, T. Sasaki, P. Xiong and J. Zhu, *Nano Energy*, 2023, **110**, 108348.

601 H. Dai, X. Cai, X. Li, C. Wang and Y. Hou, *Solid State Sci.*, 2022, **129**, 106907.

602 E. Doustkhah, M. H. N. Assadi, K. Komaguchi, N. Tsunoji, M. Esmat, N. Fukata, O. Tomita, R. Abe, B. Ohtani and Y. Ide, *Appl. Catal., B*, 2021, **297**, 120380.

603 T. C. Ozawa and T. Sasaki, *Inorg. Chem.*, 2010, **49**, 3044–3050.

604 T. C. Ozawa and T. Sasaki, *Dalton Trans.*, 2014, **43**, 14902–14908.

605 M. Ohwada, K. Kimoto, K. Suenaga, Y. Sato, Y. Ebina and T. Sasaki, *J. Phys. Chem. Lett.*, 2011, **2**, 1820–1823.

606 K. Saito, K. Inaguma, M. Ogawa, P. T. Ha, H. Akiyama, S. Yamaguchi, H. Minokoshi, M. Ogasawara and S. Kato, *ACS Appl. Nano Mater.*, 2022, **5**, 9053–9062.

607 T. Maluangnont, P. Pulphol, K. Klangvijit, K. Bowornthommatadsana, N. Chanlek, M. Ogawa and W. Wongwiriyapan, *Dalton Trans.*, 2023, **52**, 11815–11825.

608 K. Nakase, S. Ichihara, J. Matsumoto, S. Koh, M. Mizuno and T. Okada, *Langmuir*, 2022, **38**, 6076–6085.

609 J. Di, J. Xiong, H. Li and Z. Liu, *Adv. Mater.*, 2018, **30**, 1704548.

610 T. Saothayanun and M. Ogawa, *Chem. Commun.*, 2021, **57**, 10003–10006.

611 T. K. Saothayanun, R. P. Wijitwongwan and M. Ogawa, *Inorg. Chem.*, 2022, **61**, 20268–20274.

612 Q. Zhong, Y. Li and G. Zhang, *Chem. Eng. J.*, 2021, **409**, 128099.

10574 | *Chem. Soc. Rev.*, 2024, **53**, 10523–10574

This journal is © The Royal Society of Chemistry 2024